

INTERFACIAL REACTIONS IN NICKEL/TITANIUM OHMIC CONTACTS  
TO N-TYPE SILICON CARBIDE

By

JAE HYUN PARK

A DISSERTATION PRESENTED TO THE GRADUATE SCHOOL  
OF THE UNIVERSITY OF FLORIDA IN PARTIAL FULFILLMENT  
OF THE REQUIREMENTS FOR THE DEGREE OF  
DOCTOR OF PHILOSOPHY

UNIVERSITY OF FLORIDA

2003

Copyright 2003

by

Jae Hyun Park

## ACKNOWLEDGMENTS

I would like to thank my advisor, Dr. Paul H. Holloway, for the opportunity to study ohmic contacts to SiC. I am also grateful for his philosophy on the relation between research and knowledge, for his desire to understand and help students, and his devotion to improving my research. I treasure the memory of his guidance and help with research and personal affairs.

I thank my committee members, Drs. Kevin S. Jones, Cammy Abernathy, Sheng S. Li, and David Norton, for their valuable contributions. The assistance from the staffs of MAIC, Eric Lambers for AES, Dr. Valentin Craciun for XRD, and Kerry Siebein for TEM analysis, is highly appreciated. I thank Kwanghyun Baik and Kyupil Lee for RTA work, and Dr. Kaufman and Junghan Kim for TEM help.

I thank all of the members in Dr. Holloway's group including Ludie. I appreciate their friendship and patience over the past few years. I have enjoyed working with each of them. I also thank all my friends in Gainesville.

I especially thank my wife, son and God for their patience, support and encouragement through my academic years.

## TABLE OF CONTENTS

	<u>Page</u>
ACKNOWLEDGMENTS .....	iii
LIST OF TABLES .....	vii
LIST OF FIGURES .....	viii
ABSTRACT .....	xiii
CHAPTER	
1 INTRODUCTION .....	1
2 LITERATURE REVIEW .....	5
2.1 Mechanisms of Ohmic Contact .....	5
2.1.1 Introduction .....	5
2.1.2 Metal Semiconductor Junctions .....	5
2.1.3 Electron Transport Mechanisms .....	7
2.1.4 Ohmic Contacts .....	10
2.1.5 Contact Resistance Measurements .....	12
2.2 Advantages of SiC in Electronic Devices .....	15
2.2.1 High Thermal Stability .....	16
2.2.2 Wide Energy Gap .....	16
2.2.3 High Breakdown Field Strength .....	17
2.2.4 High Electron Saturation Velocity .....	17
2.2.5 High Thermal Conductivity .....	18
2.2.6 Existence of Stable Oxide .....	18
2.2.7 Commercially Available SiC Bulk Wafers .....	19
2.2.8 Polytypism of SiC .....	19
2.3 Applications of SiC .....	21
2.3.1 Power Devices (Rectifying & Power Switching Devices) .....	21
2.3.2 High Temperature Devices .....	21
2.3.3 High Frequency Power Devices .....	21
2.3.4 Substrate Material for GaN .....	21
2.4 Requirements for Ohmic Contact to SiC .....	21
2.5 Recent Trends in Ohmic Contacts to n-type 4H SiC .....	22
2.5.1 Nickel-based Ohmic Contacts .....	22
2.5.2 Other Approaches for Ohmic Contacts to n-SiC .....	24
2.5.3 Interfacial Reactions in Ni-based Ohmic Contacts .....	29

2.5.4 Advantages and Issues of Ni-based Ohmic Contact.....	42
<b>3 EXPERIMENTAL PROCEDURES.....</b>	<b>45</b>
3.1 Introduction.....	45
3.2 Substrate Preparation.....	45
3.3 Photoresist Patterning.....	46
3.4 Metal Deposition .....	48
3.5 Contact Annealing .....	50
3.6 Characterization.....	50
3.6.1 Electrical Characterization .....	50
3.6.2 Physical Characterization.....	52
<b>4 INTERFACIAL REACTIONS IN NICKEL/TITANIUM OHMIC CONTACTS TO N-TYPE SIC .....</b>	<b>55</b>
4.1 Introduction.....	55
4.2 Published Results on Multi-Layer Metal Contacts.....	55
4.3 Principles of Tri Layer Metal Contacts in This Study.....	56
4.4 Results of the Tri Metal Contact Scheme.....	58
4.4.1 Current-Voltage (I-V) Data .....	58
4.4.2 Optical Microscopy Data.....	60
4.4.3 Auger Electron Spectroscopy (AES).....	61
4.5 Effects of Ni and Ti Layers on Ohmic Contact Formation .....	63
4.5.1 Current-Voltage (I-V) Data .....	63
4.5.2 Optical Microscopy .....	66
4.5.3 XRD Data .....	67
4.5.4 Auger Electron Spectroscopy (AES).....	69
4.5.5 Auger Electron Spectroscopy (AES) : Chemical State Information .....	75
4.5.6 Transmission Electron Microscopy (TEM).....	88
4.6 Discussion.....	91
4.7 Summary.....	97
<b>5 THE EFFECTS OF NICKEL AND TITANIUM THICKNESS ON NICKEL/TITANIUM OHMIC CONTACTS TO SIC .....</b>	<b>99</b>
5.1 Introduction.....	99
5.2 Effects of Ti Thickness.....	99
5.2.1 Current and Voltage (I-V) Data.....	99
5.2.2 Optical Microscopy .....	101
5.2.3 XRD Data .....	103
5.2.4 Auger Electron Spectroscopy (AES).....	104
5.3 Effects of Ni Thickness .....	109
5.3.1 Current and Voltage (I-V) Data.....	109
5.3.2 XRD data .....	110
5.3.3 Auger Electron Spectroscopy (AES).....	112
5.3.4 Transmission Electron Microscopy (TEM).....	116

5.4 Discussion.....	119
5.5 Summary.....	126
6 CONCLUSIONS.....	128
7 FUTURE WORK.....	130
LIST OF REFERENCES.....	132
BIOGRAPHICAL SKETCH .....	138

## LIST OF TABLES

<u>Table</u>	<u>page</u>
2-1 Important physical properties of major semiconductors .....	20
2-2 Phases and atomic ratios of reaction products of Pd and Ni on SiC and Si substrates after annealing .....	31
4-1 Thermodynamic and diffusion properties of metals for ohmic contacts to SiC.....	95
4-2 Thermodynamic properties of elements for the bottom metal (Ti) of the Ti/Ni/Ti/SiC contacts to SiC .....	96

## LIST OF FIGURES

<u>Figure</u>	<u>page</u>
1-1 The F-22 aircraft subsystems potentially improved by SiC electronic components ..2	
2-1 Energy-band diagram for an n-type semiconductor before and after contact .....	6
2-2 Energy band diagram for an n-type semiconductor with a large density of interface states causing Fermi-level pinning .....	7
2-3 Four basic transport mechanisms under a forward bias: a) thermionic emission over the barrier, b) tunneling through the barrier, c) recombination in the space charge region, and d) hole injection from the metal to the semiconductor in the neutral region.....	8
2-4 Mechanisms of ohmic contact formation at different doping levels. (a) thermionic emission, (b) thermionic field emission, and (c) field emission .....	10
2-5 Energy band diagram for a highly surface doped n-type semiconductor after metal contact formation.....	12
2-6 Square transfer length method pattern. Metal remains in the gray areas after the photo resist is removed.....	13
2-7 Plot of measured resistance vs. contact gap spacing .....	14
2-8 Circular transfer length method (C-TLM) pattern with photo resist remaining in the white rings .....	15
2-9 Breakdown voltage changes in SiC and Si according to doping level .....	17
2-10 Electron drift velocity change in SiC and Si according to electric field .....	18
2-11 Properties of various polytypes of silicon carbide.....	20
2-12 Rutherford backscattering spectrometry (RBS) spectrum for annealed Ni/SiC sample.....	23
2-13 X-ray photoemission profiles of an Al/Ni/Al/SiC structure annealed at 1000°C ....	25
2-14 X-ray photoemission profiles of Ni-Si/SiC structure annealed at 950°C .....	26

2-15 X-ray diffraction pattern of Ti/Ni/Al/SiC contacts (a) as deposited, (b) annealed at 900°C for 5 min and (c) 1000°C for 5 min .....	27
2-16 I-V characteristics of the Ni/WSi/Ti/Pt ohmic contacts to n-SiC as deposited, annealed at 900°C, 950°C and 1000°C for 30 sec .....	28
2-17 AES depth profile for (a) the as deposited and (b) the 1000°C annealed Ni/WSi/Ti/Pt/SiC contacts on n-SiC .....	28
2-18 Backscattering spectra of Ni/SiC samples before and after annealing at 500 and 700°C.....	30
2-19 Ion backscattering spectra (a) Ni/SiC before annealing, (b) Ni/SiC annealed at 600°C for 10 min in forming gas .....	32
2-20 AES depth profile of specimen annealed at 600°C for 10 min .....	33
2-21 X-ray diffraction spectra for Ni/SiC samples before and after vacuum annealing for 30 min at 400, 500, 600 or 700°C .....	35
2-22 Backscattering spectra of the SiC/Ni annealed at different temperatures .....	36
2-23 Si L <sub>2,3</sub> emission band spectra for Ni/SiC samples annealed at (a) 600°C, (b) 800°C and (c) 950°C with the standard spectra of (d) 4H-SiC and (e) Ni <sub>2</sub> Si .....	38
2-24 C K emission band spectra for Ni/SiC samples annealed at: (a) 600°C, (b) 800°C and (c) 950°C with the standard spectra of (d) 4H-SiC and (e) graphite .....	39
2-25 The C K emission spectra for Ni/SiC samples annealed at 950°C was decomposed into standard C K spectra for 4H-SiC (cross) and graphite (open circle) with the spectral ratio 0.52:0.48 .....	40
2-26 XRD spectra of the Ni/SiC samples annealed in vacuum at 600°C for 25 min and in N <sub>2</sub> at 700°C for 60 s. In both cases the Ni <sub>2</sub> Si phases forms.....	41
2-27 Carbon distribution profile obtained by EDX in a Ni/SiC sample after annealing in vacuum at 600°C for 25 min. The dashed line indicates the position of the Ni/SiC interface .....	42
2-28 Interface roughness and voids formation in Ni/n-SiC contact after annealing.....	43
3-1 Schematic diagram of the photoresist patterning process .....	47
3-2 Schematic of the CTLM ring pattern.....	47
3-3 Schematic of the electron beam evaporation system.....	48

3-4	Lift-off procedure after the photoresist is deposited on the SiC substrate (a) before metal deposition, (b) after metal deposition, and (c) after the photoresist is removed, leaving the metal structure. ....	49
3-6	Schematic of the current-voltage measurement setup .....	51
4-1	I-V data of the as deposited contacts and the contacts annealed at 1000°C, 2min, (a) Al/Ni/Al/4H-SiC, (b) Ti/Ni/Ti/4H-SiC, and (c) Au/Pt/Ni/4H-SiC.....	59
4-2	Comparison of the I-V data for Al/Ni/Al/SiC and Ti/Ni/Ti/SiC contacts on either 4H or 6H SiC after annealing at 1000°C, 2min in pure N <sub>2</sub> .....	60
4-3	Optical microscope (OM) pictures of (a) Au/Pt/Ni, (b) Al/Ni/Al, and (c) Ti/Ni/Ti contacts annealed at 1000°C, 2min. ....	61
4-4	AES depth profiles of (a) Au/Pt/Ni, (b) Al/Ni/Al, and (c) Ti/Ni/Ti contacts after annealing at 1000°C, 2min. ....	62
4-5	I-V data of (a) as deposited and (b) contacts annealed at 1000°C, 2min. ....	64
4-6	I-V data from the TLM patterns of (a) the Ni/Ti/SiC contacts, and (b) the Ti/Ni/Ti/SiC contacts, both of them annealed at 1000°C, 2min. ....	65
4-7	Optical Microscope pictures of (a) as deposited Ni/SiC contacts, (b) annealed Ni/SiC contacts, (c) as deposited Ni/Ti/SiC contacts, (d) annealed Ni/Ti/SiC contacts, (e) annealed Ti/Ni/Ti/SiC contacts, and (f) annealed Au/Ni/Ti/SiC contacts, (all anneals at 1000°C, 2min).....	67
4-8	XRD data of the (a) as deposited Ti/Ni/Ti/SiC contacts and (b) annealed Ti/Ni/Ti/SiC contacts, and (c) annealed Ni/SiC contacts. Contacts annealed at 1000°C for 2min. ....	68
4-9	XRD peak matching data (a) Ni for as deposited contacts and (b) Ni <sub>2</sub> Si for annealed contacts.....	69
4-10	AES depth profiles of the Au/Ni/Ti/SiC contacts (a) as deposited, and (b) after annealing at 1000°C, 2min .....	70
4-11	AES depth profiles of the Ni/SiC contacts (a) as deposited, and (b) after annealing at 1000°C, 2min.....	71
4-12	AES depth profiles of the Ni/Ti/SiC contacts (a) as deposited, and (b) after annealing at 1000°C, 2min.....	72
4-13	AES depth profiles of the Ti/Ni/Ti/SiC contacts (a) as deposited, and (b) after annealing at 1000°C, 2min. ....	74

4-14	AES depth profile and spectra of the as deposited Ti/Ni/Ti/SiC contacts (a) depth profile, (b) surface, (c) Top Ti (d) Ni, and (e) Bottom Ti .....	76
4-15	AES spectrum of titanium in metallic and carbide state, and carbon in graphite (organics) and carbide state <sup>69</sup> .....	78
4-16	AES depth profile and spectra of the as deposited Ni/Ti/SiC contacts (a) depth profile, (b) surface, (c) Ni layer, and (d) Bottom Ti layer.....	79
4-17	AES spectra of carbon in (a) graphite or surface contamination-organics and hydrocarbons, and (b) carbide state <sup>69</sup> .....	80
4-18	AES depth profile and spectra of the annealed Ti/Ni/Ti/SiC contacts (a) depth profile, (b) surface, (c) top Ti, (d) bottom Ti, (e) Ni <sub>x</sub> Si, (f) carbon peak at the Ni <sub>x</sub> Si/SiC interface, and (g) SiC substrate.....	83
4-19	AES depth profile and spectra of the annealed Ni/Ti/SiC contacts (a) depth profile, (b) surface, (c) bottom Ti (d) Ni <sub>x</sub> Si, and (e) carbon peak layer at the Ni <sub>x</sub> Si/SiC interface .....	87
4-20	Cross-sectional TEM data of the (a) Ni/SiC contacts and (b) Ti/Ni/Ti/SiC contacts. Both annealed at 1000°C for 2min. ....	89
4-21	TEM EDX data of the Ti/Ni/Ti/SiC contacts annealed at 1000°C for 2min. (a) on Ni <sub>2</sub> Si layers, (b) on TiC layers, and (c) C layers.....	90
4-22.	A schematic model of the Ti/Ni/Ti/SiC contacts. (a) as deposited and (b) after annealing .....	92
5-1	I-V data of the contacts with different bottom Ti thickness (a) as deposited contacts and (b) annealed contacts .....	100
5-2	OM pictures of the contacts with different Ti thickness. (a)&(b) as deposited contacts, balance from annealed contacts with Ti thickness of (c)&(d) 30 nm, (e)&(f) 20 nm, (g)&(h) 10 nm, and (i)&(j) 0 nm. ....	101
5-3	XRD data of the contacts with different Ti thickness (a) as deposited, and after annealing with a Ti thickness of (b) 30 nm, (c) 20 nm, (d) 10 nm, and (e) 0 Ti (Ni only) contacts. Contacts are annealed at 1000°C for 2min.....	103
5-4	XRD peak matching data using JCPDS (a) Ni (JCPDS: 04-0850) for as deposited contacts and (b) Ni <sub>2</sub> Si (JCPDS: 73-2092) for annealed contacts ((d) and (e) in figure 5-3).....	104
5-5	AES depth profiles of the contacts with Ti thickness 30 nm (a) as deposited, and (b) annealed at 1000°C for 2min. ....	105

5-6	AES depth profiles of the contacts with Ti thickness 20 nm (a) as deposited, and (b) annealed at 1000°C for 2min.....	106
5-7	AES depth profiles of the contacts with 10 nm Ti thickness (a) as deposited, and (b) annealed at 1000°C for 2min.....	107
5-8	AES depth profiles of the contacts with 0 bottom Ti (Ni only) (a) as deposited, and (b) annealed at 1000°C for 2min.....	108
5-9	I-V curves of the contacts with different Ni thickness. (a) as deposited contacts and (b) contacts annealed at 1000°C for 2min.....	110
5-10	XRD data of the contacts with different Ni thickness. (a) 30 nm, (b) 50 nm, (c) 70 nm, and (d) 90 nm. The contacts are annealed at 1000°C for 2min.....	111
5-11	AES depth profiles of the Ti/Ni/Ti contacts with 90 nm of Ni (a) as deposited, and (b) annealed at 1000°C for 2min.....	112
5-12	AES depth profiles of the contacts with 70 nm of Ni (a) as deposited, and (b) annealed at 1000°C for 2min.....	113
5-13	AES depth profiles of the contacts with 50 nm of Ni (a) as deposited, and (b) annealed at 1000°C for 2min.....	114
5-14	AES depth profiles of Ti/Ni/Ti contacts with 30 nm of Ni (a) as deposited, and (b) annealed at 1000°C for 2min.....	115
5-15	Cross-sectional TEM images of the Ti/Ni/Ti contacts with different Ni thickness. (a) as deposited contacts with Ni 30 nm, (b) annealed contacts with Ni 30 nm, (c) annealed contacts with Ni 70 nm, and (d) annealed contacts with Ni 90 nm. Contacts are annealed at 1000°C for 2min. Bottom Ti 20 nm.....	117
5-16	TEM EDX line scanning data of the Ti/Ni/Ti contacts with different Ni thickness. (a) as deposited contacts with Ni 30 nm, and (b) annealed contacts with Ni 30 nm, and (c) annealed contacts with Ni 90 nm. Contacts are annealed at 1000°C for 2min. Bottom Ti 20 nm.....	118
5-17	Schematic model of the layers in the thick (30nm) bottom Ti contacts (a) as deposited, and (b) annealed contacts.....	120
5-18	Schematic model of the layers in 90nm Ni contacts (a) as deposited, and (b) annealed contacts, bottom Ti 20 nm.....	124
5-19	Schematic model of the layers in 50 and 70 nm Ni contacts (a) as deposited, and (b) annealed contacts, bottom Ti 20 nm.....	124
5-20	Schematic model of the layers in 30 nm Ni contacts (a) as deposited, and (b) annealed contacts, bottom Ti 20 nm.....	125

Abstract of Dissertation Presented to the Graduate School  
of the University of Florida in Partial Fulfillment of the  
Requirements for the Degree of Doctor of Philosophy

INTERFACIAL REACTIONS IN NICKEL/TITANIUM OHMIC CONTACTS  
TO N-TYPE SILICON CARBIDE

By

Jae Hyun Park

December 2003

Chair: Paul H. Holloway

Major Department: Materials Science and Engineering

Titanium/nickel/titanium ohmic contacts to n-SiC have been studied. The Ti/Ni/Ti/SiC structures were rectifying as the as-deposited state but became ohmic upon annealing at 1000°C for 2 minutes in a N<sub>2</sub> ambient. A nickel silicide phase (Ni<sub>2</sub>Si) was formed, resulting in a specific contact resistance ( $\rho_C$ ) as low as  $1 \times 10^{-4} \Omega \text{ cm}^2$ . Smooth interface profiles were obtained due to the Ti layer between the Ni and SiC. Auger depth profile data and transmission electron microscopy analysis showed that Ni moved through the Ti layer to decompose the SiC and form Ni<sub>2</sub>Si, leaving excess carbon as a reaction product. Some of the carbon reacted with the two Ti layers to form titanium carbide (TiC). These phases are observed because titanium carbide has lower free energy of formation than titanium silicide, and nickel silicide has a lower free energy of formation than titanium silicide. The carbon that was not bonded as TiC was distributed in the silicide layer and at the silicide/SiC interface as a graphite phase. A schematic model of the layers in the Ti/Ni/Ti/SiC contacts was deduced. The dependence of ohmic

contact resistance on Ni and Ti layer thickness was also studied. Contacts with a 20 nm bottom Ti and Ni/Ti ratio of 3.5 showed a contact resistance of  $1 \times 10^{-4} \Omega \text{ cm}^2$ , while maintaining an interfacial roughness of 7.5 nm. Thicker bottom Ti ( $>20$  nm) contacts were rectifying with a non-linear I-V behavior, and there was still a Ti layer between the Ni and SiC after annealing. The lack of an ohmic contact was attributed to the Ti layer acting as a diffusion barrier preventing the formation of  $\text{Ni}_2\text{Si}$ . The Ni thickness was varied from 90 to 30 nm over 20 nm Ti bottom layers, but the specific contact resistances ( $\rho_C$ ) ( $3.3 \times 10^{-4} \pm 2.5 \times 10^{-4} \Omega \text{ cm}^2$ ) did not vary systematically with Ni thickness. Thicker Ni ( $>30$  nm) contacts showed a non-uniform carbon distribution with carbon peaks at the silicide/SiC interface as graphite. Thin Ni contacts (30 nm) showed more uniform carbon distribution than in the contacts with thicker Ni. No significant carbon peak layer was found at the silicide/SiC interface.

## CHAPTER 1 INTRODUCTION

Silicon carbide (SiC) is a wide band-gap semiconductor, which has prospects for a variety of applications. The applications include high power, high frequency, and high temperature devices. Silicon carbide is currently used as a substrate for gallium nitrides LED's. Military aircraft designers are investigating the potential of using SiC in various electronic devices. The interest is generated by the prospect of designing aircraft with improved flight control systems, mass reduction, and reduced reliability on environmental control subsystems.<sup>1,2</sup> SiC can operate at both higher temperatures and higher frequency compared to Si. The trend to incorporate SiC electronics into aircraft is referred to as the more electric aircraft (MEA) initiative.<sup>1,2</sup> The MEA also includes military and commercial systems such as electric vehicles, ships, and commercial power. Figure 1-1 shows components of the Air Force's aircraft, the F-22, that would benefit from SiC electronic devices.

SiC devices can operate at high frequency (8~10 GHz) for temperatures up to 500 °C.<sup>1,2</sup> High frequency applications include radar and communication systems for unpiloted aircraft and satellite arrays. The automotive and petroleum industries also have an interest in SiC-based technology. The automotive industry is exploring engine control sensors using SiC.<sup>1,2</sup> These SiC-based electronic sensors would also be used to probe the environment around drilling equipment where temperatures reach about 300 °C.<sup>1,2</sup>

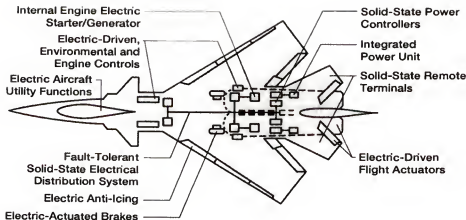


Figure 1-1 The F-22 aircraft subsystems potentially improved by SiC electronic components<sup>1</sup>

Some applications would benefit from SiC technology because of its higher operating temperatures and long-term reliability.<sup>3</sup>

Junction field effect transistors (JFET) using SiC are being studied by a variety of companies including Siemens AG in Germany, US Army research, and NASA.<sup>3</sup> The CEA-LETI in France and Cree Research are making metal oxide semiconductor field effect transistors (MOSFET).<sup>3</sup> Cree Research is also producing p-n diodes and thyristors. General Electric is making operational amplifier IC's with SiC.<sup>3,4</sup> Kyoto University in Japan makes Schottky diodes.<sup>3,4</sup>

The nickel-based contacts have been studied as a major material for ohmic contact to n-type 4H SiC. The n-type ohmic contacts based on nickel are currently reported to have the lowest specific contact resistance ( $\sim 5 \times 10^{-6} \Omega \text{cm}^2$ ) due to the formation of stable and reproducible metal silicides at the interface during annealing.<sup>5</sup>

However, the difficulty of controlling the metal contact properties, as well as the need of optimal annealing conditions to reduce the risk of nickel oxidation, remains limiting factors for many industrial applications. There are four major issues related to nickel based ohmic contacts to n-SiC in terms of the difficulty of controlling the metal contact properties:<sup>5-7</sup> broadening of the metal SiC interface; rough interface morphology with voids; excess carbon segregation released from silicide reaction at the metal SiC interface; and substantial roughening of the contact surface.

The Ni diffusion into the SiC substrate causes excessive interfacial reactions deep into the substrate. This limits the device performances in achieving a shallow junction depth of transistors. Interface roughness and interface broadening are issues for long-term reliability of SiC devices. Interface oxidation degrades the device performance and creates difficulties in achieving proper ohmic contact properties.

There have been many approaches to improve these issues, such as employing new multi-layer metal structures. This includes Ni-Cr, Ni-Al and Ni-Si, etc.<sup>8-10</sup> Some improvements have been reported but not for all issues simultaneously. In addition, the mechanisms leading to the improvements were not adequately explained. It is important to continue efforts to develop a stable ohmic contact to n-type SiC.

The goals for this study can be summarized as follows.

First, it is desirable to obtain a reproducible and low specific contact resistance so that a minimum voltage drop across the metal semiconductor junction can be achieved.

Second, the interface and junction should be uniform, shallow and abrupt with lateral homogeneity of the interfacial phases. Control of interface roughening and interfacial reactions is important. To obtain a uniform, shallow and abrupt metal

semiconductor interface with homogeneous interfacial phases, metal diffusion into the substrate and interfacial reactions should be controlled.

Third, reduction of excess carbon at the interface after annealing is required to improve the high temperature stability. Finally, preventing surface oxidation of contacts is a factor that determines their high temperature stability.

## CHAPTER 2 LITERATURE REVIEW

### 2.1 Mechanisms of Ohmic Contact

#### 2.1.1 Introduction

An ohmic or Schottky barrier (rectifying) contact is formed when a metal is brought into contact with a semiconductor.<sup>11-13</sup> A contact may be ohmic if the electron affinity of an n-type semiconductor ( $\chi_s$ ) is greater than the work function of the metal ( $\phi_M$ ). An ohmic contact has a linear and symmetric current-voltage relationship for both positive and negative bias and a small resistance compared to the bulk resistivity of the semiconductor. Fermi-level pinning and interfacial contamination may prevent formation of an ohmic contact, even when  $\chi_s > \phi_M$ .<sup>14</sup>

#### 2.1.2 Metal Semiconductor Junctions

An ideal Schottky or rectifying contact occurs when a metal is brought into contact with an n-type semiconductor that has an electron affinity ( $\chi_s$ ) less than that of the metal work function ( $\phi_M$ ), or has interface conditions such as Fermi-level pinning.<sup>12,15</sup> Figure 2-1 shows the energy level diagrams before (a) and after contact (b). The work function of the semiconductor,  $\phi_s$ , is the difference between the vacuum level ( $E_{vac}$ ) and the Fermi energy level ( $E_F$ ). The semiconductor work function is given by:<sup>12,15</sup>

$$\phi_s = \chi_s + V_n \quad [v] \quad (2-1)$$

where  $V_n$  is the energy difference between the bottom of the conduction band ( $E_C$ ) and the Fermi level. Once contact occurs, the Fermi levels in both the metal and the semiconductor

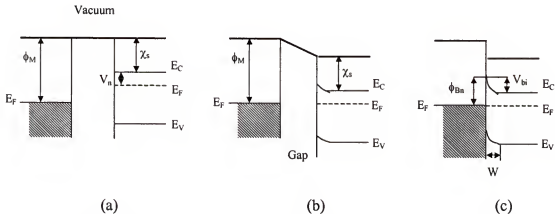


Figure 2-1 Energy-band diagram for an n-type semiconductor before and after contact<sup>15</sup> line up at thermal equilibrium. The conduction and valence band levels in the semiconductor are raised or lowered relative to the metal by the difference in the work functions. This energy shift is called the “built-in” or “contact” potential,  $V_{bi}$ ;<sup>12</sup>

$$V_{bi} = \phi_M - \phi_S \quad [v] \quad (2-2)$$

For  $\phi_M > \chi_s$ , a negative charge is built up on the metal and an equal and positive charge forms on the semiconductor as a result. This produces a barrier height equal to

$$\phi_{Bn} = \phi_M - \chi_s \quad [v] \quad (2-3)$$

Unfortunately, it has been shown experimentally that most semiconductor/metal contacts do not obey the predictions of this ideal Schottky limit.<sup>11,15</sup> Schottky contacts may also be influenced by a large number of surface states at the interface. In a simple model, the Schottky barrier height,  $\phi_B$ , can be expressed as follows.<sup>12</sup>

$$\phi_B = S \cdot \chi_m + \phi_0 \quad [v] \quad (2-2)$$

where  $\chi_m$  is the metal electronegativity, and  $\phi_0$  represents the contribution of surface states from the semiconductors. The interface index

$$S = \frac{d\phi_B}{d\chi_m} \quad [v] \quad (2-2)$$

is a function of the electronegativity difference,  $\Delta\chi$ , between the cationic and anionic components of a compound semiconductor. This S factor should be equal to unity for an ideal semiconductor/metal junction. When  $S=0$ , the system is in the regime of strong "Fermi level pinning." The surface states are occupied to the Fermi level,  $E_F$ . If the surface has a large quantity of surface states, the Fermi level will remain unchanged once equilibrium is achieved. In this case, the barrier is not affected by the metal work function but is solely controlled by the semiconductor surface. This phenomenon is also known as Fermi-level pinning<sup>11,15</sup> and is shown in figure 2-2.

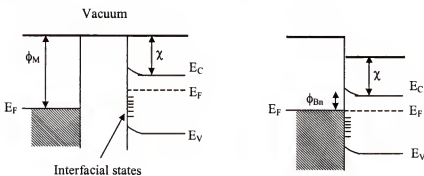


Figure 2-2 Energy band diagram for an n-type semiconductor with a large density of interface states causing Fermi-level pinning<sup>11,15</sup>

### 2.1.3 Electron Transport Mechanisms

There are four common transport mechanisms for electrons across metal-semiconductor contacts: (1) thermionic emission over the barrier, (2) tunneling through the barrier, (3) recombination in the space charge region, and (4) hole injection from the

metal to the semiconductor in the neutral region.<sup>12</sup> These mechanisms are illustrated schematically in Figure 2-3.

Thermionic emission theory assumes that the barrier height is much larger than  $kT$  (0.0259 eV at 300°K). When thermal equilibrium is reached, the net current flow does not affect thermal equilibrium. Based on these assumptions, the barrier height is the only factor affecting current flow. The current density can be expressed as a function of voltage by<sup>12,15</sup>

$$I = I_s \left[ \exp\left(\frac{qV}{kT}\right) - 1 \right] \quad [A] \quad (2-4)$$

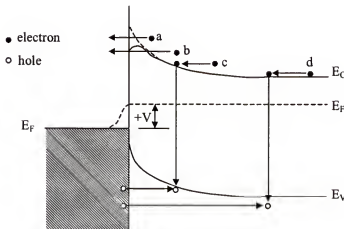


Figure 2-3 Four basic transport mechanisms under a forward bias: a) thermionic emission over the barrier, b) tunneling through the barrier, c) recombination in the space charge region, and d) hole injection from the metal to the semiconductor in the neutral region<sup>12</sup>

where  $q$  is the electron charge,  $V$  is the applied voltage,  $k$  is Boltzmann's constant,  $T$  is temperature, and  $I_s$  the saturation current is

$$I_s = A ** ST^2 \exp\left[-\frac{\phi_{Bn}}{kT}\right] \quad [A] \quad (2-5)$$

where  $S$  is the contact area,  $A^{**}$  is the effective Richardson constant, ( $J = I/S$  and  $J_S = I_S/S$ ).

The total current density is given by the sum of the current from the metal into the semiconductor ( $J_{m \rightarrow s}$ ) and the current from the semiconductor into the metal ( $J_{s \rightarrow m}$ ). Then the total current density is expressed as<sup>12,15</sup>

$$J = J_S \left[ \exp\left(\frac{qV}{nkT}\right) - 1 \right] \quad [A/cm^2] \quad (2-6)$$

where  $n$  is the ideality factor, defined as

$$n \equiv \frac{q}{kT} \frac{\partial V}{\partial(\ln J)} \quad (2-7)$$

where  $\partial V/\partial(\ln J)$  and the saturation current density ( $J_S$ ) are found experimentally. Low doped materials at high temperatures have an ideality factor that is close to one and  $J_S$  is relatively constant.<sup>12</sup>

For higher doping and low temperatures, the tunneling current ( $J_t$ ) dominates. The current density can be expressed as

$$J_t \sim \exp\left(-\frac{q\phi_{Bn}}{E_{00}}\right) \quad [A/cm^2] \quad (2-8)$$

where the energy term is given by

$$E_{00} \equiv \frac{q\hbar}{2} \sqrt{\frac{N_d}{\epsilon_s m^*}} \quad [eV] \quad (2-9)$$

where  $\hbar$  is  $h/2\pi$ .  $N_d$  will increase the current by an exponential factor of  $N_d^{1/2}$ .

Electrons will also recombine with holes in the space-charge region. Holes from the metal move to the top of the valence band ( $E_v$ ) of the semiconductor while an electron from the semiconductor moves to the bottom of the conduction band ( $E_C$ ) as shown in

Figure 2-3 (c). The electron falls to the valence level and combines with the hole. This same process also occurs in the neutral region as illustrated in Figure 2-3 (d).<sup>12</sup>

### 2.1.4 Ohmic Contacts

Fermi-level pinning and interfacial contamination may prevent formation of an ohmic contact, even when  $\chi_S > \phi_M$ .<sup>11,15</sup> Ohmic contacts require a very low voltage to drive a current across the contact interface.

For an Ohmic contact, current is transported across the interface by mechanisms shown in Figure 2.4. Current transport can be principally ascribed to the following three mechanisms:<sup>11,12,15</sup>

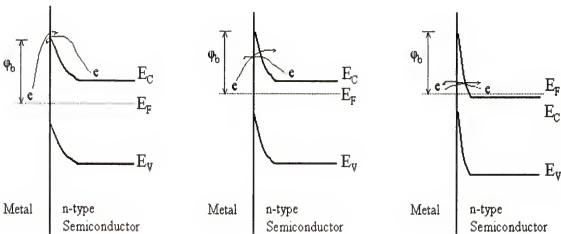


Figure 2-4 Mechanisms of ohmic contact formation at different doping levels. (a) thermionic emission, (b) thermionic field emission, and (c) field emission

First, thermionic emission (TE) is a dominant in low and moderately doped semiconductors with  $N_{e(h)} < 10^{17} \text{ cm}^{-3}$ . At low to moderate carrier densities, the wide depletion region prevents tunneling through the barrier. When the barrier height is small, the electrons can be thermally excited over the top of the barrier (thermionic emission,

Figure 2-4a). On the other hand, for a high barrier, the majority of electrons are unable to overcome this barrier, resulting in non-ohmic (rectifying) contacts.

Second, thermionic-field emission (TFE) is applicable for intermediate doping densities,  $\sim 10^{17} \text{ cm}^{-3} < N_{e(h)} < 10^{18} \text{ cm}^{-3}$ . Both thermionic and tunneling emissions are important (Figure 2-4b).

Third, field emission (FE) is only effective in heavily doped semiconductors,  $N_{e(h)} > \sim 10^{18} \text{ cm}^{-3}$ . In this case the depletion region is narrow, and electron or hole can tunnel easily from metal to semiconductor or vice versa (Figure 2-4c).

Ohmic contacts are described by the specific contact resistance,  $\rho_c$ , defined as the derivative of the current density (J) at a zero voltage (V = 0):<sup>12,15</sup>

$$\rho_c \equiv \left( \frac{\partial J}{\partial V} \right)_{V=0}^{-1} \quad [\Omega \text{ cm}^2] \quad (2-10)$$

Metal-semiconductor contacts with low doping, with thermionic emission as the dominant mechanism, have specific contact resistivity that is given by the following equation:<sup>12,15</sup>

$$\rho_c = \frac{k}{qA^{**}T} \exp\left(\frac{q\phi_{Bn}}{kT}\right) \quad [\Omega \text{ cm}^2] \quad (2-11)$$

where k is Boltzmann's constant, q is the electron charge, and A<sup>\*\*</sup> is the effective Richardson constant for thermionic emission. The specific contact resistance is clearly dependent on temperature. At high temperatures, the thermionic emission current increases and results in a smaller resistance.

The specific contact resistance for higher doping level ( $> 10^{18} \text{ cm}^{-3}$ ) where tunneling is the primary method of electron transport is given by

$$\rho_c \sim \exp\left(\frac{q\phi_{Bn}}{E_{00}}\right) = \exp\left[\frac{2\sqrt{\epsilon_s m^*}}{\hbar}\left(\frac{\phi_{Bn}}{\sqrt{N_d}}\right)\right] \quad [\Omega \text{ cm}^2] \quad (2-12)$$

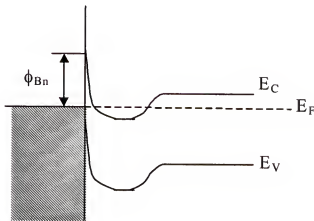


Figure 2-5 Energy band diagram for a highly surface doped n-type semiconductor after metal contact formation<sup>12,15</sup>

where  $\epsilon_s$  is the semiconductor permittivity,  $\hbar$  is  $h/2\pi$ , and  $N_d$  is the donor concentration.

The energy diagram for an ohmic contact on a highly [degenerately doped] surface doped n-type semiconductor is given in figure 2-5.

### 2.1.5 Contact Resistance Measurements

The contact resistance can be defined completely if physical and operating parameters are known.<sup>11,15</sup> The physical parameters are mainly of contact area and thickness, while operating parameters are predominantly temperature and bias. In practice, the contact resistance can be affected by a number of other factors, such as interfacial layers (oxide formation or contamination), surface damage, minority carrier injection, and deep impurity levels.

The most widely used method for determining the specific contact resistance is the transfer length method or transmission line model (TLM).<sup>14,16</sup> An array of contacts is fabricated with various spacing between them as shown in figure 2-6.

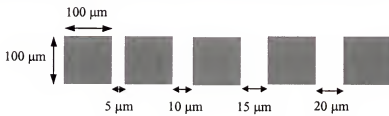


Figure 2-6 Square transfer length method pattern. Metal remains in the gray areas after the photo resist is removed<sup>16</sup>

The resistance is measured as a function of the gap spacing. Extrapolation of the resistance to zero gap spacing gives a value equal to twice the contact resistance  $R_c$ . The distance axis intercept is equal to twice the transfer length  $L_t$ , which is given as the following equation,<sup>14,16</sup>

$$L_t = \left[ \frac{\rho_c}{R_s} \right]^{1/2} \quad (2-13)$$

where  $R_s$  is the sheet resistance of the semiconductor and  $\rho_c$  is the specific contact resistance. Figure 2-7 shows a plot of measured resistance vs. contact gap spacing. The transfer length is defined as the distance from the edge to where the current in the contact falls to  $1/e$  of its original value. The specific contact resistance ( $\rho_c$ ) can be calculated using the equation,<sup>14,16</sup>

$$\rho_c = \frac{R_c^2 \cdot W^2}{R_s} = R_s \cdot L_t^2 \quad (2-14)$$

where  $R_c$  is the contact resistance,  $w$  is the width of contact pattern,  $R_s$  is the semiconductor sheet resistance and  $L_t$  is the transfer length as defined as (2-13). The units

for  $\rho_C$  are expressed in  $\Omega \text{ cm}^2$ . Since the test pattern should be isolated so that current flows only in the space between dots (no leakage path), a mesa structure may be required.<sup>14,16</sup>

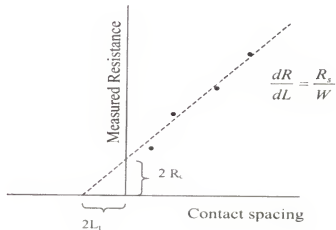


Figure 2-7 Plot of measured resistance vs. contact gap spacing<sup>16</sup>

For the ring pattern of the circular transfer length method (C-TLM) in figure 2-8, the device isolation step can be omitted because there is no leakage path for current flow. The resistance calculation is complex, but when  $r_t/L_t \gg 1$ , it can be simplified and calculated using the following equation.<sup>17</sup>

$$R = \frac{1}{2\pi} \left[ R_{sc} L_t \left( \frac{1}{r_2} + \frac{1}{r_1} \right) + R_s \ln \left( \frac{r_2}{r_1} \right) \right] \quad [\Omega] \quad (2-15)$$

where  $r_1$  is the inner radius,  $r_2$  is the outer one, and  $R_s$  is the sheet resistance of the semiconductor. The total resistance of the contact is measured for different spacing as a function of  $\ln(r_2/r_1)$ . The least square curve-fitting method can be used to obtain a straight linear plot of

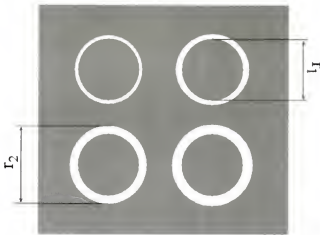


Figure 2-8 Circular transfer length method (C-TLM) pattern with photo resist remaining in the white rings

$R$  vs.  $\ln(r_2/r_1)$ . The slope gives  $R_s$ , and the intercept at  $\ln(r_2/r_1) = 0$  is  $R_s L_v / r\pi$ , leading to  $L_v$ . So the specific contact resistance can be expressed as  $L_v = [\rho_v / R_s]^{1/2}$ . In practice the outside radius is usually 200~300  $\mu\text{m}$  and the gap spacing are 10, 20, 30, 40, 50, 60, 70, 80 and 90  $\mu\text{m}$ .

A good ohmic contact should have a low specific resistance, high stability, smooth surface morphology and good edge definition. Because contact resistance usually constitutes a small portion of the total measured resistance, caution must be taken to avoid errors.

## 2.2 Advantages of SiC in Electronic Devices

Silicon carbide (SiC) is currently under intensive investigation as an enabling material for a variety of new semiconductor devices in areas where silicon devices cannot effectively compete. These include high power, high voltage switching applications, high temperature electronics and high power microwave applications in the 1~10 GHz regime.<sup>1,2</sup> Silicon carbide is attractive for these applications because of its extreme

thermal stability, wide energy gap, high breakdown field strength, high electron saturation velocity, high thermal conductivity, existence of stable oxide and commercially available SiC bulk wafers.<sup>18-21</sup> In the following sections, some of the key advantages of using SiC as electronic devices are listed.

### 2.2.1 High Thermal Stability

Due to the strong covalent bond of Si and C in SiC, it has very high melting temperature at 2839°C.<sup>3</sup> This thermal stability of SiC promises long-term reliable operation at high temperatures where silicon devices cannot effectively operate.

### 2.2.2 Wide Energy Gap

Because of the wide energy (band) gap (4H-SiC: 3.25eV), the intrinsic carrier concentration ( $6.2 \times 10^9 \text{ cm}^{-3}$  at 300°K) of SiC is much lower than that of silicon ( $1.1 \times 10^{10} \text{ cm}^{-3}$  at 300°K). The intrinsic carrier concentration ( $n_i$ ) is related to the energy gap of the semiconductors by the following equation<sup>13,18</sup>

$$n_i = (N_c \cdot N_v)^{\frac{1}{2}} \cdot \exp\left[\frac{(E_v - E_c)}{2kT}\right] = (N_c \cdot N_v)^{\frac{1}{2}} \cdot \exp\left[-\frac{E_g}{2kT}\right] \quad [\text{cm}^{-3}] \quad (2-16)$$

where  $N_c$  is the effective density of states in the conduction band,  $N_v$  is the effective density of states in valence band,  $E_g$  is energy gap, and  $k$  is Boltzmann's constant. Low intrinsic carrier concentration allows the leakage current in SiC to be many orders of magnitude lower than in silicon and an intrinsic temperature well over 800°C is observed. This electronic property makes SiC attractive for high temperature devices and high radiation environment applications.

### 2.2.3 High Breakdown Field Strength

Fig. 2-9 shows that breakdown voltages of Si and SiC according to doping level. The breakdown field strength ( $3.8 \times 10^6$  V/cm) in SiC is 8 times higher than Si due to the wide energy gap of SiC.<sup>22</sup> High breakdown field strength is critical for power switching devices, because the specific on-resistance scales inversely as the cube of the breakdown

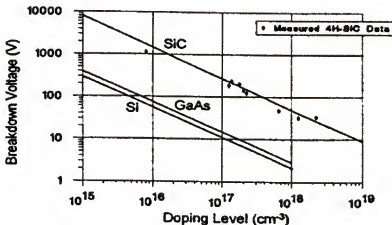


Figure 2-9 Breakdown voltage changes in SiC and Si according to doping level<sup>22</sup> field. Thus, SiC power devices are expected to have a specific on-resistance 100~200 times lower than Si devices.<sup>22</sup>

### 2.2.4 High Electron Saturation Velocity

The electron mobility in SiC is lower than in Si, which gives slower electron response in SiC than in Si. However, the electron saturation velocity ( $2.2 \times 10^7$  cm/sec) at high electric field is two times higher than Si, as shown in Fig. 2-10.<sup>23</sup> This is an important parameter for high power radio and microwave applications. The field dependence of electron drift velocity can be represented by the two following equations at low and high electric field, respectively.<sup>13,23</sup>

$$v_{\text{drift}} = \mu_n \cdot E \quad [\text{cm/sec}] \quad : \text{ at low } E\text{-field}$$

$$v_{\text{drift}} = v_{\text{sat}} \quad [\text{cm/sec}] \quad : \text{ at high } E\text{-field}$$

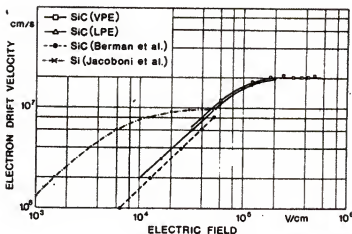


Figure 2-10 Electron drift velocity change in SiC and Si according to electric field<sup>23</sup>

### 2.2.5 High Thermal Conductivity

The high thermal conductivity (4.9W/cm°K) of SiC results in a fast cooling rate during device operation at high power and high frequency. Therefore, this will reduce the cooling requirements of the system. This property is critical for aircraft applications in terms of minimizing the total mass of the system.<sup>18,24</sup>

### 2.2.6 Existence of Stable Oxide

SiC is the only compound semiconductor that can be thermally oxidized to form a high quality native oxide (SiO<sub>2</sub>). The stable oxide makes it possible to fabricate metal oxide semiconductor field effect transistors (MOSFET), insulated gated bipolar transistors (IGBT), and MOS-controlled thyristors (MCT) using SiC.<sup>18</sup>

### 2.2.7 Commercially Available SiC Bulk Wafers

Single crystal bulk wafers of SiC have been commercially available since 1990 (current standard: 2" diameter). This makes SiC a strong candidate for high temperature and high power electronic devices.

### 2.2.8 Polytypism of SiC

There are a wide variety of polytypes of silicon carbide with differing electrical and physical properties. The energy gap is 2.390 eV for 3C-SiC and 3.330 for 2H-SiC.<sup>25</sup> A polytype is a material that consists of the same chemical composition but the atomic stacking sequence changes in a regular way over distance. Over 170 different polytypes exist for SiC.<sup>25</sup> The  $\alpha$ -SiC consists of rhombohedral (R) and hexagonal (H) types or wurtzite structure. The  $\beta$ -SiC describes the cubic (C) or zinc blende structure. There are a few common types of  $\alpha$ -SiC: namely 2H, 4H, 6H, and 15R. The 2H and 15R types are rare.<sup>25</sup> The two polytypes of interest are typically 4H and 6H for their electrical properties.

The structures of the five key polytypes are shown in Figure 2-11. The 6H structure consists of about 33% hexagonal structure, meaning that the stacking sequence consists of two (identical neighboring) hexagonal bilayers and four (different neighboring) cubic bilayers. The 3C-SiC is difficult to grow in large volumes and consequently is not commercially available. Anti-phase boundaries, stacking faults, and threading dislocations are defects that occur during growth and influence the properties of

3C	15R	6H	4H	2H	
$\begin{array}{c} A \\ B \\ C \end{array} \} C_3$	$\begin{array}{c} A \\ B \\ C \\ A \\ C \\ B \\ C \\ A \\ B \\ A \\ C \\ A \\ B \\ C \\ B \end{array} \} C_{15}$	$\begin{array}{c} A \\ B \\ C \\ A \\ C \\ B \end{array} \} C_6$	$\begin{array}{c} A \\ B \\ A \\ C \end{array} \} C_4$	$\begin{array}{c} A \\ B \end{array} \} C_2$	
$a_0 = 4.349 \text{ \AA}$	37.700	15.079	10.050	5.048	$\text{C}_0 \text{ IN \AA}$
(2)	(10)	(12)	(8)	(4)	ATOMS PER UNIT CELL
F43m $T_d^2$	R3m $C_{3v}^5$	P6 <sub>3</sub> mc $C_{6v}^4$	P6 <sub>3</sub> mc $C_{6v}^4$	P6 <sub>3</sub> mc $C_{6v}^4$	SPACE GROUPS
(1)	(5)	(3)	(2)	(1)	INEQUIVALENT SITES
2.390	2.986	3.023	3.265	3.330	$E_{\text{GX}} (2 \text{ K}) \text{ (eV)}$

Figure 2-11 Properties of various polytypes of silicon carbide<sup>25</sup>

both  $\alpha$ - and  $\beta$ -SiC. These defects led to “leaky”  $pn$  junctions.<sup>25</sup> Important physical properties of a few major semiconductors are listed in Table 2-1.

Table 2-1 Important physical properties of major semiconductors<sup>18,21,24</sup>

Materials	$E_g$ (eV)	$\mu_n$ (cm <sup>2</sup> /V•s)	$E_c$ (10 <sup>6</sup> V/cm)	$V_{\text{sat}}$ (10 <sup>7</sup> cm/s)	$\lambda$ (W/cm)	$n_i$ (cm <sup>-3</sup> ) at 300°K
Si	1.12	1350	0.3	1.0	1.5	$1.5 \times 10^{10}$
Ge	0.66	3900	0.1	0.5	0.6	$2.4 \times 10^{13}$
GaAs	1.43	8500	0.4	2.0	0.5	$1.8 \times 10^6$
6H-SiC	3.0	370 <sup>a</sup> , 50 <sup>c</sup>	3.0	2.2	4.9	$2.4 \times 10^{-5}$
4H-SiC	3.26	720 <sup>a</sup> , 650 <sup>c</sup>	3.8	2.2	4.9	$6.2 \times 10^{-9}$
Diamond	5.45	1900	5.6	2.7	20	$2.4 \times 10^{-27}$

a : a-axis, c : c-axis

### 2.3 Applications of SiC

#### 2.3.1 Power Devices (Rectifying & Power Switching Devices)

For high power applications, SiC devices can be used as transistors and thyristors.

In transistor application, power MOSFET structures can be utilized. Schottky diodes, junction diodes, Thyristor and GTO (Gate turn-off Thyristor) are devices for power rectifying applications.<sup>2,18,26,27</sup>

#### 2.3.2 High Temperature Devices

Aerospace (“more electric aircraft”), automobile (engine) and geothermal sensor applications are areas that require the high temperature (200 ~ 500°C) capability of electronic devices. Due to its wide energy gap, SiC can be used for devices operating under high radiative environments, such as satellites and space exploration.<sup>2,18,26,27</sup>

#### 2.3.3 High Frequency Power Devices

Metal Semiconductor Field Effect Transistor (MESFET) and Static Induction Transistor (SIT) are two major vehicles being developed for the high frequency, high power (RF and microwave frequency) devices using SiC.<sup>2,18,26,27</sup>

#### 2.3.4 Substrate Material for GaN

As a substrate material for the Optoelectronic device applications (GaN light emitting diodes-LEDs and diode lasers), SiC has advantages over the conventional substrate material (Al<sub>2</sub>O<sub>3</sub>: Sapphire) due to its better lattice matching to GaN. Higher thermal conductivity of SiC also allows the GaN devices to have a faster cooling rate.<sup>24</sup>

### 2.4 Requirements for Ohmic Contact to SiC

There are four essential requirements for ohmic contacts to SiC.<sup>6</sup> They can be summarized as follows. First, a reproducible and low specific contact resistance ( $\rho_c$ ) is

required. This is essential for high frequency operation to reduce power loss across the metal semiconductor junction. Second, high temperature and high power means that the contacts must be reliable under extreme operating conditions. Thermal stability with SiC at high temperatures and mechanical stability of ohmic contacts are critical. Third, a uniform, shallow and abrupt metal semiconductor interface is important for both long time stability and device performance. Since long time and high temperature annealing could degrade the interface quality, stability of interfacial phases and the device performance (junction depth, transistor parameters and materials compatibility), the ohmic contact process needs to be optimized to have a uniform, abrupt and stable interface. Finally, surface and interface oxidation issues need to be controlled to obtain stable ohmic contacts.

## 2.5 Recent Trends in Ohmic Contacts to n-type 4H SiC

### 2.5.1 Nickel-based Ohmic Contacts

Ohmic contacts to n-type SiC have been formed from a variety of silicides, carbides and single metal elements. Nickel (Ni)-based metal contacts has been proposed as the most suitable and promising candidate for the fabrication of ohmic and rectifying metal contact to n-type 4H silicon carbide,<sup>5,7,8,28,29</sup> and are already used for high voltage SiC Schottky rectifier. For fabricating ohmic contacts on SiC using nickel, annealing processes of Ni/SiC are generally performed under different atmospheres at 950~1000°C, all resulting in low

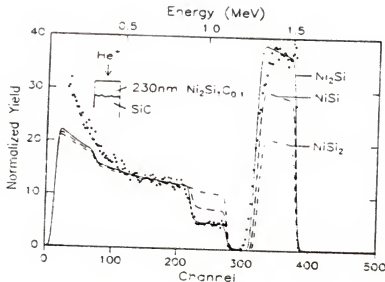


Figure 2-12 Rutherford backscattering spectrometry (RBS) spectrum for annealed Ni/SiC sample<sup>5</sup>

values of specific contact resistance. One of the studies on the n-type ohmic contact based on Ni has reported specific contact resistance as low as  $\sim 5 \times 10^{-6} \Omega \text{cm}^2$ .<sup>5</sup> The low contact resistance and ohmic contact formation is attributed to the formation of nickel silicide (Ni<sub>2</sub>Si) at the interface.<sup>5,7,28</sup> The RBS spectrum with simulations (Figure 2-12) and AES data suggested the formation of Ni<sub>2</sub>Si phase at the interface. The annealing process that forms the ohmic contact results in the formation of a nickel silicide layer with incorporated C and O throughout the layer.<sup>5</sup>

It is reported that there are issues from metal semiconductor interface broadening and roughening after annealing.<sup>5,8</sup> This could degrade the device performances. Ni diffusion into the substrate and inter-diffusion between Ni and other metal layers needs to be optimized. There is a concern due to the generation of excess carbon at the metal-SiC

interface after silicide reaction. This excess carbon layer could be a problem for high temperature reliability.<sup>5,8</sup>

### 2.5.2 Other Approaches for Ohmic Contacts to n-SiC

Recently there have been many new efforts and approaches in the Ni based ohmic contact area to improve the properties. A Ni-Cr system was tried to reduce interdiffusion between the Ni and a Au cap layers for wire bonding. Metal interdiffusion between the Ni and Au cap layer was reduced due to the relatively large Cr concentration at the surface of the Ni-Cr contact layer that acted as a barrier. Enhanced Ni adhesion to the Au cap layer was also reported. The electrical characteristics of the Ni-Cr contacts were similar to those for pure Ni contacts.<sup>9</sup>

Experiments with Al/Ni/Al/SiC structures were also reported to result in improved interfaces due to Al-O and Al-C reactions. In this study Al was selected based on reports of the formation of carbide and oxide that could reduce unreacted carbon and interfacial oxides.<sup>30</sup> The top Al layer was mainly consumed by formation of Al<sub>2</sub>O<sub>3</sub> to avoid Ni surface oxidation. The bottom Al layer was believed to prevent voids at the interface and also to reduce the oxide on the semiconductor surface (Figure 2-13). The bottom Al layer did not participate in creating the actual ohmic contact. Some of the excess carbon was reduced due to the Al-C reaction that resulted in the formation of Al<sub>4</sub>C<sub>3</sub>.<sup>30</sup>

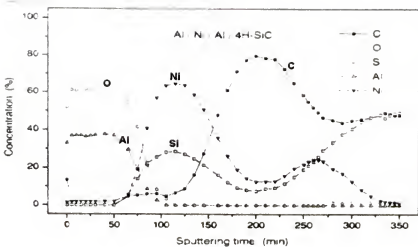


Figure 2-13 X-ray photoemission profiles of an Al/Ni/Al/SiC structure annealed at 1000°C<sup>30</sup>

Metal structures of Ni/Si/SiC and Si/Ni/SiC were utilized to prevent SiC dissociation during contact formation. The structural and chemical properties of the interface were improved by using Ni/Si layers instead of pure nickel for ohmic contacts on n-SiC. These structures resulted in reduced excess carbon at the interface by providing a Si source for getting any free C.<sup>8,31</sup> A Ni<sub>2</sub>Si layer was formed after annealing. Figure 2-14 shows that lower carbon concentrations were observed at the interface and within the contact layer in Ni/Si/SiC and Si/Ni/SiC contacts as compared to Ni/SiC contacts. The number of interface voids

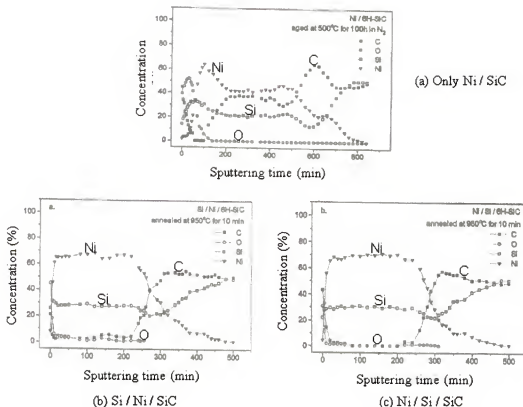


Figure 2-14 X-ray photoemission profiles of Ni-Si/SiC structure annealed at 950°C for 10min<sup>8</sup>

decreased significantly leading to an enhancement of the contact reliability. The Si/Ni ratio and the influence of the thickness of the interfacial Si layer were important factors optimized for this contact structure.

Ohmic contacts using Al/Ni/Ti/SiC and Al/Ni/Al/SiC structures were investigated.<sup>32</sup> Nickel silicide (Ni<sub>2</sub>Si) layers formed after annealing. Ni<sub>2</sub>Si with a (203) texture is the dominant phase after 900°C annealing. Continued annealing to 1000°C caused a decrease of the TiC and Ni<sub>2</sub>Si (203) X-ray diffraction (XRD) peaks. As shown in Figure 2-15 (c), many peaks at positions corresponding to different orientations of Ni<sub>2</sub>Si were observed. Al at the interface improved interface oxidation in Al/Ni/Al

structure. The Ti-C reaction reduced excess carbon formation at the interface in Al/Ni/Ti contact.<sup>32</sup> The Al and Ti layers did not participate in forming the actual ohmic contact, but they improved the contact stability by reducing the interface oxide and reacting with carbon. Titanium seems to give a better metal/n-SiC interface than aluminum, resulting in better contact resistance on n-type SiC than Al/SiC contact

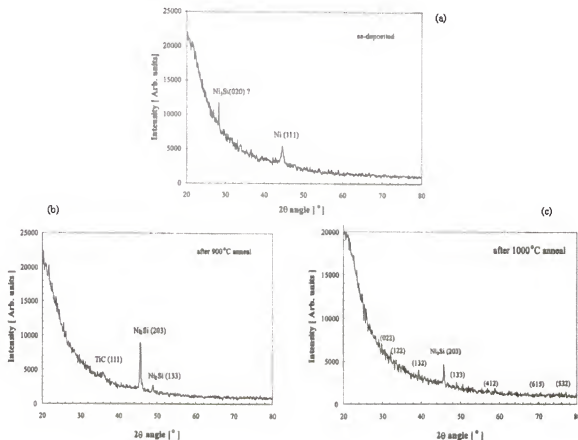


Figure 2-15 X-ray diffraction pattern of Ti/Ni/Al/SiC contacts (a) as deposited, (b) annealed at 900°C for 5 min and (c) 1000°C for 5 min<sup>32</sup>

A multi-layer metal structure, Pt/Ti/WSi/Ni/SiC, was studied in an attempt to reduce the unreacted carbon and to provide silicon from the source. The annealing temperature was varied from 900 to 1000°C.<sup>6</sup> Annealing at 900°C caused the I-V characteristics to become more ohmic (Figure 2-16). The contacts became fully ohmic

after a 950°C anneal. A further reduction in resistance and the best ohmic behavior was achieved after annealing at 1000°C. Thus, annealing at temperatures between 900 and 1000°C significantly enhanced the current conduction through the contacts. The AES depth

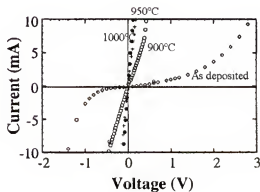


Figure 2-16 I-V characteristics of the Ni/WSi/Ti/Pt ohmic contacts to n-SiC as deposited, annealed at 900°C, 950°C and 1000°C for 30 sec<sup>6</sup>

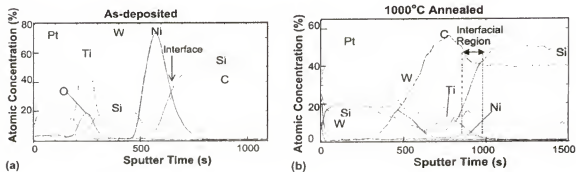


Figure 2-17 AES depth profile for (a) the as deposited and (b) the 1000°C annealed Ni/WSi/Ti/Pt/SiC contacts on n-SiC<sup>6</sup>

profiles for the as deposited and 1000°C annealed samples are shown in Figure 2-17. In the as deposited contact, the layer sequence is distinct. Extensive intermixing has occurred in response to the 1000°C heat treatment. XRD analysis showed that WC and

TiC layers formed at the interface after annealing, reducing the excess carbon from the metal carbon reactions. SEM images showed that the WC and TiC layers reduced interface roughening and voids.<sup>6</sup>

Other ohmic contacts using TiC to n-type SiC have also shown promise, but with higher contact resistances of  $\sim 10^{-4} \sim 10^{-5} \Omega \text{cm}^2$ .<sup>33,34</sup> Numerous other metals have been tried, including W, WN, Ta and TiN.<sup>35,36</sup> W and WN ohmic contacts have excellent thermal stability but require too high an annealing temperature.<sup>35</sup> Many other metallizations, namely Ta, TaC, Ti/Au, Co and TiN, have been investigated for ohmic contacts with some interesting results.<sup>7,37</sup>

Based on these studies, Ni-based contacts have been suggested to be superior candidates for ohmic contact to n-SiC due to their reproducible low specific contact resistance.<sup>5</sup>

### 2.5.3 Interfacial Reactions in Ni-based Ohmic Contacts

There have been many studies of the onset of the silicide reactions in Ni-based ohmic contacts to n-SiC. However, there is poor agreement since the temperatures reported range from 300–600°C.<sup>38-40</sup> Ni reacts with SiC and forms nickel silicide (Ni<sub>2</sub>Si) and graphite, the latter being either uniformly distributed inside the silicide layer or as a surface layer.

Pai, Hansen, and Lau<sup>38</sup> studied the metallurgical interaction of Ni on SiC using X-ray diffraction and Rutherford backscattering spectrometry. Nickel on SiC shows no detectable reaction after annealing at 400°C. The ion backscattering spectra of a Ni/SiC

sample before and after annealing at 500 and 700°C are shown in Fig. 2-18. Ni has completely

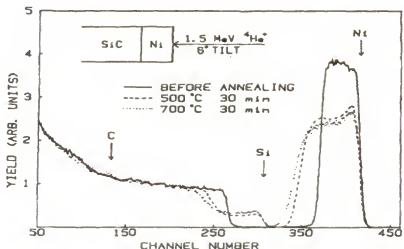


Figure 2-18 Backscattering spectra of Ni/SiC samples before and after annealing at 500 and 700°C<sup>38</sup>

reacted with the SiC substrate after annealing at 500°C. The atomic ratios of Ni to Si in the reaction products were measured to be 2.3 and 1.8 after annealing at 500 and 700°C, respectively. X-ray diffraction analysis showed that both  $\text{Ni}_{31}\text{Si}_{12}$  and  $\text{Ni}_2\text{Si}$  coexist after annealing at 500°C.  $\text{Ni}_2\text{Si}$  is the only silicide phase observed after annealing between 700 and 900°C.

In the case of Ni/Si contacts,  $\text{Ni}_2\text{Si}$  forms at 250°C, transforming to  $\text{NiSi}$  at 400°C and  $\text{NiSi}_2$  at 800°C.<sup>38</sup> Ni/SiC contacts show that higher temperatures are required to cause the initial reactions and that a metal-rich silicide is formed first in both cases. For comparison the results obtained for Ni/Si vs. Ni/SiC reactions are listed in Table 2-2.

Table 2-2 Phases and atomic ratios of reaction products of Pd and Ni on SiC and Si substrates after annealing<sup>38</sup>

T (°C)	Pd/SiC		Pd/Si		Ni/SiC		Ni/Si
	Phases identified by x-ray diffraction	Pd to Si atomic ratios by RBS	Phases formed <sup>1</sup>	Phases identified by x-ray diffraction	Ni to Si atomic ratios by RBS	Phases formed <sup>1</sup>	Phases formed <sup>1</sup>
300	No reaction	No reaction	Pd <sub>3</sub> Si	No reaction	No reaction	Ni <sub>3</sub> Si	Ni <sub>3</sub> Si
400	No reaction	No reaction	Pd <sub>3</sub> Si	No reaction	No reaction	Ni <sub>3</sub> Si	Ni <sub>3</sub> Si
500	Pd <sub>3</sub> Si	2.9	Pd <sub>3</sub> Si	Ni <sub>3</sub> Si <sub>12</sub> , Ni <sub>2</sub> Si	2.3	Ni <sub>3</sub> Si	Ni <sub>3</sub> Si
600	Pd <sub>3</sub> Si	2.9	Pd <sub>3</sub> Si	Ni <sub>3</sub> Si <sub>12</sub> , Ni <sub>2</sub> Si	2.2	Ni <sub>3</sub> Si	Ni <sub>3</sub> Si
700	Pd <sub>3</sub> Si, Pd <sub>2</sub> Si	2.2	Pd <sub>3</sub> Si	Ni <sub>2</sub> Si	1.8	Ni <sub>3</sub> Si	Ni <sub>3</sub> Si
800	Pd <sub>3</sub> Si	1.9	Pd <sub>3</sub> Si	Ni <sub>2</sub> Si	1.8	Ni <sub>3</sub> Si <sub>2</sub>	Ni <sub>3</sub> Si <sub>2</sub>
900	Pd <sub>3</sub> Si	...	PdSi	Ni <sub>2</sub> Si	...	Ni <sub>3</sub> Si <sub>2</sub>	Ni <sub>3</sub> Si <sub>2</sub>

The reason for the differences in the reaction temperature is that the bonding between Si and C play an important role in the formation of a silicide on SiC. The difference in electro negativities,  $\Delta\chi$ , between Si and C is about 0.7, thus leading to a partial ionic bonding characteristic of SiC.<sup>38</sup> The partial ionic bonding nature of SiC may limit not only the supply of Si during reaction, but also raise the reaction temperatures as well, due to the need to break Si-C bonds. The activity of Si in SiC is obviously less than that in Si itself. In forming silicides for SiC, the free energy driving force is reduced by the free energy formation of SiC. Thus, in the case of reactions with SiC, compounds requiring less SiC dissociation will be increasingly favored relative to reactions with elemental Si for any given silicide.

Because of the low sensitivity of the backscattering technique for light elements, the measurement of the amount of the carbon in the reacted film could not be performed. Thus, the behavior of the carbon atoms during the metal/SiC interface reaction has not been clarified.

Ohdomari et al<sup>39</sup> used a high-energy ion backscattering technique with resonance scattering of helium and carbon to obtain a highly sensitive analysis of carbon contained

in SiC substrate and in reaction products. The atomic ratio of Ni to Si gradually changes in the reacted film, and the ratio near the surface and interface were measured to be 2.5 and 2.0, respectively. As shown in Figure 2-19, the carbon signal was high enough to separate

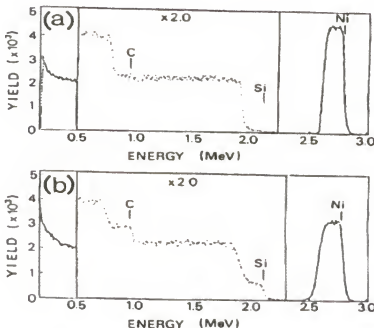


Figure 2-19 Ion backscattering spectra (a) Ni/SiC before annealing. (b) Ni/SiC annealed at 600°C for 10 min in forming gas<sup>39</sup>

from that of Si. Carbon is distributed uniformly with a concentration of about 25 at. % throughout the reacted film. The XRD spectra also demonstrated that polycrystalline Ni<sub>2</sub>Si was formed in the reacted film.

The Auger spectra were taken at different sputtering times. The C KLL spectra at sputtering times of 10-180 min are shown in Fig 2-20. Some line shapes of C KLL Auger spectra are shown from (a) to (c). The remarkable difference of the line shape between (a), (b) and (c) is indicated by the arrows. The line shape of C KLL spectra at sputtering times of 10-120 min ((a) and (c)) was that of elemental carbon, which is called “graphite carbon”, not to carbide.<sup>39</sup> The line shape after sputtering for 180 min is identical to that

of SiC. There was no indication of nickel carbide formation. Ni, Si and C are distributed uniformly in the reacted film.

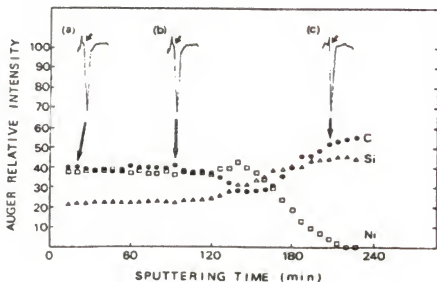


Figure 2-20 AES depth profile of specimen annealed at 600°C for 10 min<sup>39</sup>

In this study Ni carbide was not detected. Single-phase polycrystalline Ni<sub>2</sub>Si was formed as the only reaction products.<sup>39</sup>

Porter et al. reviewed the formation of ohmic contacts on SiC.<sup>28</sup> The sequence of phase formation in bulk diffusion couple was Ni / Ni<sub>3</sub>Si / Ni<sub>3</sub>Si<sub>12</sub> / Ni<sub>2</sub>Si / SiC. Carbon in the form of graphite is found not only at the interface with SiC, but also throughout the Ni<sub>3</sub>Si<sub>12</sub> and Ni<sub>2</sub>Si layers. The situation is expected to differ for thin Ni films deposited on a SiC substrate. There, the limited amount of Ni, the large surface to volume ratio of the film, and the huge stresses typically observed in thin films impose different boundary conditions that could lead to reaction pathways different from those of bulk reactions.<sup>28</sup>

In terms of carbon distribution after annealing, Pai et al.<sup>38</sup> reported the formation of the Ni<sub>3</sub>Si<sub>12</sub> phase after annealing at 500°C, 30 min and the Ni<sub>2</sub>Si phase after 700°C, 30min annealing in vacuum. However, carbides were not found. In the study by

Ohdomari et al.<sup>39</sup> where annealing was performed in forming gas, no reaction between the Ni film and 6H-SiC was observed at 500°C. At 600°C, Ni<sub>2</sub>Si forms, carbon bonds are found to be graphitic and the carbon concentration is described as being constant throughout the reacted film, except near the Ni<sub>2</sub>Si/SiC interface where the carbon is slightly depleted. No such depletion is reported by Marinova et al.,<sup>8</sup> but NiSi rather than Ni<sub>2</sub>Si is inferred to exist (probably erroneously) from X-ray photoemission spectroscopy on a sample annealed in forming gas at 1000°C for 1h. Rastegaeva et al.<sup>41</sup> on the other hand, see an enhancement of carbon at the Ni<sub>2</sub>Si/SiC interface in their Auger electron spectrum of a sample annealed in vacuum at 1000°C for an unspecified duration. They propose that this enrichment is a key factor in the formation of an ohmic contact.

Marinova et al.<sup>8</sup> also observe a carbon peak at the Ni<sub>2</sub>Si/SiC interface in an X-ray photoemission profile of a sample annealed in an N<sub>2</sub> atmosphere for 10 min at 950°C. According to Crofton et al.<sup>5</sup>, the role of carbon incorporation is not well understood yet.

Bachli et al.<sup>40</sup> reported X-ray diffraction data from the samples with different annealing temperatures. As shown in Fig 2-21, after annealing at 500°C, the Ni peaks disappeared completely and new peaks emerge that can be attributed to the Ni<sub>31</sub>Si<sub>12</sub> phase. At 600°C, these Ni<sub>31</sub>Si<sub>12</sub> peaks weakened and some of the main peaks of the orthorhombic

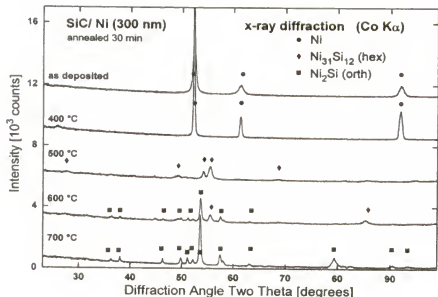


Figure 2-21 X-ray diffraction spectra for Ni/SiC samples before and after vacuum annealing for 30 min at 400, 500, 600 or 700°C<sup>40</sup>

Ni<sub>2</sub>Si phase appeared. This phase is the only one detected by X-ray diffraction after annealing at 700°C. The films were strongly textured. Backscattering spectra of the samples annealed at different temperatures are given in Fig. 2-22, supporting the XRD data. The peak of the backscattering signal indicates a high carbon concentration at the surface. This carbon layer is too thin to be resolved by backscattering spectrometry. The Ni<sub>2</sub>Si phase began to form at 600°C. The Ni<sub>2</sub>Si phase nucleates at or close to the surface and grows toward the SiC/ Ni<sub>31</sub>Si<sub>12</sub> interface. The final state was a layer of Ni<sub>2</sub>Si with

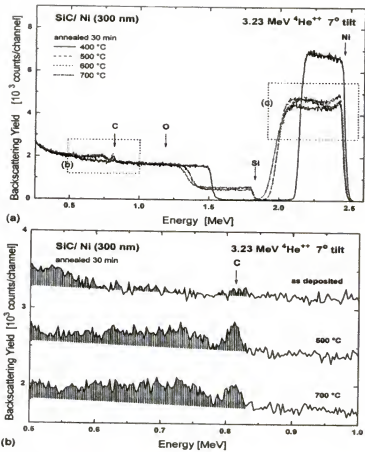


Figure 2-22 Backscattering spectra of the SiC/Ni samples annealed at different temperatures<sup>40</sup>

incorporated carbon. Neither the crystallographic structure nor the morphology of this carbon was specified except that it was uniformly distributed in aerial average.

Crofton et al.<sup>5,7</sup> have concluded that after a 2 min annealing at 950°C in a vacuum, a Ni film on 6H-SiC also turns into Ni<sub>2</sub>Si. All existing evidence thus points towards the conclusion that this Ni<sub>2</sub>Si phase is independent of the poly type, the polarity of the SiC and the details of the annealing cycle, as long as the system has had the opportunity to reach its thermodynamically stable state. The time-temperature cycle and the vacuum conditions may affect the kinetics and the pathway of the reaction. This in turn could change the morphology of the carbon and silicide in the final state. The ability to reduce

the carbon content of the reacted layer has practical relevance because graphitic inclusions tend to increase the resistivity of the reacted layer.<sup>40,42</sup>

Additional insight can be gained from cross-sectional transmission electron micrographs of annealed Ni/SiC samples. In bulk diffusion couples, a laterally and perpendicularly discontinuous distribution of carbon in the reacted nickel silicide layer has often been reported.<sup>40</sup> Cross-sectional micrographs for Ni/SiC contacts have been recently published.<sup>8</sup> After 2 min of annealing at 950°C in a N<sub>2</sub> ambient of a 150 nm Ni film on 6H-SiC, Marinova et al.<sup>8</sup> see a fully reacted layer of Ni<sub>2</sub>Si that contains many light globular and banded features they interpret as Kirkendall voids. Gasser et al. annealed their sample of a 300 nm-thick Ni film on 3H-SiC for 30 min at 700°C in vacuum and see a fully reacted layer of Ni<sub>2</sub>Si that contains elongated light features perpendicular to the plane of the layer.<sup>40</sup> High-resolution images identified them as nano grains of graphitic carbon. If nickel is the dominant moving species throughout all reactions that lead to the layer of Ni<sub>2</sub>Si and carbon, Kirkendall voids would not be expected to exist at the Ni<sub>2</sub>Si interface and within the bulk of the Ni<sub>2</sub>Si, so the light banded features along the Ni<sub>2</sub>Si/SiC interface would represent a region of enriched carbon. The Auger and X-ray photoemission profiles are consistent with such an interpretation.

Ohi et al.<sup>43</sup> used soft X-ray emission spectroscopy (SXES) with synchrotron radiation to characterize annealed Ni/4H-SiC samples. Si L<sub>2,3</sub> SXE showed the formation of Ni<sub>2</sub>Si for annealing temperatures at 600, 800 and 950°C as shown in Fig 2-23.

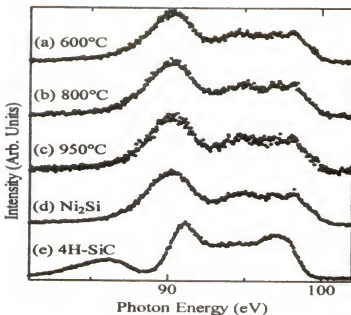


Figure 2-23 Si L<sub>2,3</sub> emission band spectra for Ni/SiC samples annealed at (a) 600°C, (b) 800°C and (c) 950°C with the standard spectra of (d) 4H-SiC and (e) Ni<sub>2</sub>Si<sup>43</sup>

The C K SXE indicated the formation of graphite and graphitic carbons at annealing temperatures of 950°C and below 800°C, respectively. To investigate further the chemical states of the carbon species, C K SXES studies were carried out. Fig. 2-24 shows C K spectra. Fig. 2-24 (a), (b) and (c) show the spectra for Ni/SiC samples annealed at 600, 800 and 950°C. Fig. 2-24 (d) and (e) shows the standard spectra for 4H-SiC and graphite. Each spectrum was measured with incident photon energy of 350eV, and is normalized by the highest peaks. The C K SXE for 4H-SiC (Fig 2-24 (d)) and graphite (e) have prominent peaks at energies of ~278 and ~276 eV, respectively. The C K emission

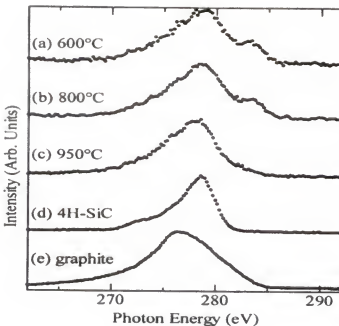


Figure 2-24 C K emission band spectra for Ni/SiC samples annealed at: (a) 600°C, (b) 800°C and (c) 950°C with the standard spectra of (d) 4H-SiC and (e) graphite<sup>43</sup>

spectrum for the Ni/SiC sample annealed at 950°C (c) shows a broader peak at ~278 eV with a shoulder around 276 eV. Samples annealed at 600 and 800°C exhibit small peaks around 283 eV, in addition to the main peaks at ~278 eV. Thus, the SXE spectrum for each of the annealed Ni/SiC samples differs from the standard spectra, and the chemical states of carbon atoms in the samples could not be identified by simple comparison with the standard materials.

In order to explain the C K emission from Ni/SiC samples, decomposition of these spectra was carried out. Fig. 2-25 shows the result for the sample annealed at 950°C. The measured spectrum could be separated into the C K spectrum for 4H-SiC (cross) and for

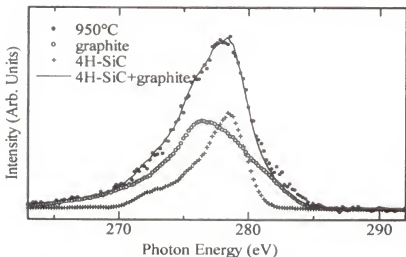


Figure 2-25 The C K emission spectra for Ni/SiC samples annealed at 950°C was decomposed into standard C K spectra for 4H-SiC (cross) and graphite (open circle) with the spectral ratio 0.52:0.48<sup>43</sup>

graphite (open circle) with intensity ratio of 0.52:0.48. Thus, the SXE spectrum from the sample annealed at 950°C is the superposition of SXE from 4H-SiC and graphite. This indicates that carbon atoms existed in the reacted region as graphite. The graphite should be composed of fine grains, because crystalline graphite is not detected by the X-ray diffraction

Roccaforte et al.<sup>44,45</sup> also confirmed the formation of Ni<sub>2</sub>Si phase after annealing of the Ni/SiC samples using X-ray diffraction spectra. Fig 2-26 shows the XRD spectra of two samples annealed in vacuum at 600°C for 25 min or undertaken to RTA at 700°C in N<sub>2</sub> for 60 sec. The thermal treatment of the Ni/SiC samples result in both cases in the formation

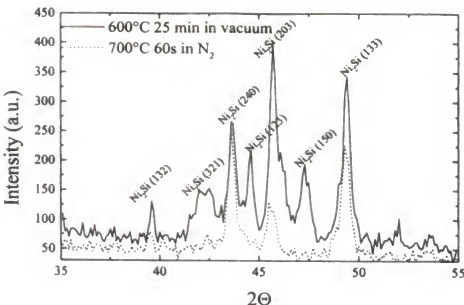


Figure 2-26 XRD spectra of the Ni/SiC samples annealed in vacuum at 600°C for 25 min and in N<sub>2</sub> at 700°C for 60 s. In both cases the Ni<sub>2</sub>Si phases forms.<sup>44</sup>

of polycrystalline nickel silicide (Ni<sub>2</sub>Si). The main peaks observed are associated with diffraction from the planes (240), (203) and (133) of the phase Ni<sub>2</sub>Si. The coexistence with other nickel rich phases like Ni<sub>2</sub>Si<sub>12</sub>, which has the largest negative enthalpy of formation, was not detected under these annealing conditions. In both cases diffraction peaks from pure nickel were not observed, indicating that the deposited film completely reacted after these thermal treatments. Annealing at higher temperature up to 1000°C did not induce the formation of phases other than Ni<sub>2</sub>Si, and no evidence of carbide could be found.

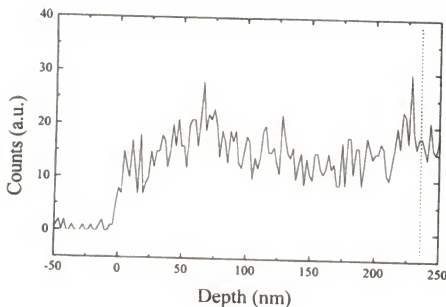


Figure 2-27 Carbon distribution profile obtained by EDX in a Ni/SiC sample after annealing in vacuum at 600°C for 25 min. The dashed line indicates the position of the Ni/SiC interface<sup>44</sup>

The redistribution of carbon after silicide formation, which is one of the most controversial arguments in the studies on Ni/SiC solid state reaction, was monitored by means of EDX and the obtained carbon profile is reported in Fig 2-27. Carbon is almost uniformly distributed inside the films, thus confirming the RBS analysis.<sup>44,45</sup>

#### 2.5.4 Advantages and Issues of Ni-based Ohmic Contact

The nickel-based contacts have been studied as a major material for ohmic contact to n-type 4H SiC. The n-type ohmic contacts based on nickel are currently reported to have the lowest specific contact resistance ( $\sim 5 \times 10^{-6} \Omega \text{cm}^2$ )<sup>5</sup> due to the formation of stable and reproducible metal silicides at the interface during annealing.

However, the difficulty of controlling the metal contact properties, as well as the need of optimal annealing conditions to reduce the risk of nickel oxidation, remain limiting factors for many industrial applications. There are four major issues related to

nickel based ohmic contacts to n-SiC in terms of the difficulty of controlling the metal contact properties<sup>5-7</sup>: broadening of the metal SiC interface; rough interface morphology with voids; excess carbon segregation released from silicide reaction at the metal SiC interface; and substantial roughening of the contact surface. The interface roughness and voids formation is shown in figure 2-28.

The Ni diffusion into the SiC substrate causes excessive interfacial reactions deep into the substrate. This limits the device performances in achieving a shallow junction depth of transistors.

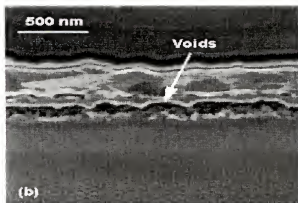


Figure 2-28 Interface roughness and voids formation in Ni/n-SiC contact after annealing<sup>6</sup>

Interface roughness and interface broadening are issues for long-term reliability of SiC devices. Interface oxidation degrades the device performance and creates difficulties in achieving proper ohmic contact properties.

There have been many approaches to improve these issues, such as employing new multi-layer metal structures. This includes Ni-Cr, Ni-Al and Ni-Si etc.<sup>8,9,30</sup> Some improvements have been reported,<sup>8,9,30</sup> but not for all issues simultaneously. In

addition, the mechanisms leading to the improvements were not adequately explained. It is important to continue efforts to develop a stable ohmic contact to n-type SiC.

## CHAPTER 3 EXPERIMENTAL PROCEDURES

### 3.1 Introduction

This chapter describes the experimental procedures that were followed for sample cleaning and preparation of electrical contact to n-type SiC. The procedures consist of an initial cleaning of the samples and photolithographic patterning, followed by metal deposition. After finishing a patterning step and a metal deposition step, the contacts were heat treated in an annealing chamber. Then the samples were characterized for their electrical properties, elemental composition and interfacial reaction products.

### 3.2 Substrate Preparation

In this study, n-type 4H (Hexagonal) silicon carbide (SiC) wafers were used. They were purchased from Cree Research Inc., and Sterling Semiconductor, Inc. The 4H SiC wafers were grown using the modified Lely method.<sup>46-48</sup> The n-type 4H SiC substrates were nitrogen (N<sub>2</sub>) doped to  $3.55 \times 10^{18}$  and  $1.22 \times 10^{19} \text{ cm}^{-3}$ , which corresponds to 0.03 and 0.014  $\Omega \text{cm}$  of resistivity. The SiC wafers orientation was  $7.5 \sim 8^\circ$  off the (0001) axis.

For the electrical characterization of the samples, photoresist patterns for circular transfer length method (CTLM) were employed. The size of the samples used in this study was 7×7 mm. Before photoresist patterning or metal deposition, a cleaning process was used consisting of two steps including a DI rinse. First, the samples were immersed in a hydrogen peroxide (H<sub>2</sub>O<sub>2</sub>) / ammonium hydroxide (NH<sub>4</sub>OH) / water (H<sub>2</sub>O) solution

with a ratio of 1:1:5 and heated at 85°C for 5 minutes. The samples were then rinsed in DI water and blown dry with N<sub>2</sub> gas.

The non-patterned samples were used for physical characterization techniques, such as X-ray diffraction (XRD) and transmission electron microscopy (TEM). For non-patterned samples, first they were immersed in a hydrogen peroxide (H<sub>2</sub>O<sub>2</sub>) / ammonium hydroxide (NH<sub>4</sub>OH) / water (H<sub>2</sub>O) solutions with a ratio of 1:1:5 and heated at 85°C for 5 minutes, the same as patterned samples. After a DI rinse step, the samples were cleaned in a 10% hydrofluoric acid (HF) solution for 20 seconds to remove native oxides from the surface. The samples were rinsed with DI water to clean any excess HF solution and blown dry using nitrogen.

### 3.3 Photoresist Patterning

In order to accurately measure the contact resistance, a circular transfer length method (CTLM) patterns were utilized as described in chapter 2. After the first cleaning step in H<sub>2</sub>O<sub>2</sub> / NH<sub>4</sub>OH / H<sub>2</sub>O solutions, a pre-bake step in a hot oven at 90°C for 10 minutes was used to remove water. Then the photoresist (NR7-1500PY: negative photoresist) was applied by spinning at 4000 r.p.m. for 40 seconds. The photoresist coating was followed by a soft bake in a hot oven at 150°C for 10 minutes to dry the photoresist. The samples with photoresist were then exposed to ultraviolet (UV) light (wavelength = 365 nm) through a contact mask for 10 seconds in a contact mask aligner. The post exposure-bake for cross-linking the photoresist was done in a hot oven at 100°C for 10 minutes. Immersing the samples in a photoresist developer (RD6) for 20 seconds completed the CTLM pattern, removing the unexposed photoresist. Any residue was cleaned from the substrates by a de-ionized water (DI) rinse following the developing

step. The samples were blown dry by  $N_2$ . A flow diagram of the photoresist patterning process is shown in Fig. 3-1.

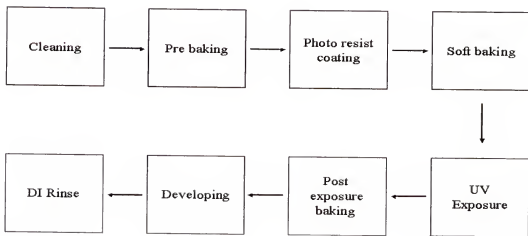


Figure 3-1 Schematic diagram of the photoresist patterning process

A CTLM pattern consists of a square with nine rings of photo resist pattern remaining. The inner diameter of all the rings was  $300\text{ }\mu\text{m}$ . The gap distances between the inner circles and the outer circles varied from 10 to 20, 30, 40, 50, 60, 70, 80, or 90

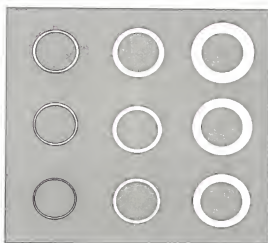


Figure 3-2 Schematic of the CTLM ring pattern

$\mu\text{m}$ . A schematic of the CTLM ring pattern is shown in Fig. 3-2.

### 3.4 Metal Deposition

After the CTLM patterning using photo resist or the first cleaning in a  $\text{H}_2\text{O}_2$  /  $\text{NH}_4\text{OH}$  /  $\text{H}_2\text{O}$  solutions (non-patterned samples case), the samples were cleaned in a 10% hydrofluoric acid (HF) solution for 10 seconds to remove native oxides on the surface. The samples were rinsed with DI water to clean any excess HF solution and blown dry using nitrogen. The samples were then immediately introduced into the vacuum chamber for contact metal deposition. All metal contacts were deposited in an electron beam evaporation system with a glass bell jar. Electron beam evaporation

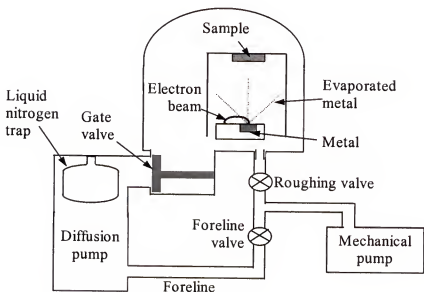


Figure 3-3 Schematic of the electron beam evaporation system

provides fast and easy deposition as compared to sputter deposition.<sup>49</sup> Deposition of high melting point elements can be performed more easily with electron beam evaporation than from thermal evaporation sources. The electron beam evaporation

system was pumped with a Varian oil diffusion pump backed by a two-stage mechanical rotary vane pump, providing a base pressure of  $1 \times 10^{-6} \sim 2 \times 10^{-6}$  torr. A schematic of the electron beam evaporation system is shown in Fig. 3-3.

The source metals in the electron beam well consisted of metal pellets with the following purities: Nickel (Ni : Target Materials Inc., 99.95%), Titanium (Ti : Cerac, 99.95%), Gold (Au : Materials Research Corporation, 99.95%), Aluminum (Al : Cerac, 99.95%), and Silicon (Si : semiconductor grade).

Metal was deposited on the substrate at room temperature. The thickness of the deposited metal layers was monitored using a quartz crystal oscillator that was installed next to the sample stage. The contact metal thickness varied with different experiments and will be noted in the results sections.

After the metal deposition, agitating the samples in acetone for a few minutes lifted off the metal film from the ring pattern areas where there was photoresist remaining after exposure and developing. This "lift-off" process leaves the desired contact patterns for CTLM. The overall flow of the lift off process is shown in Fig. 3-4.

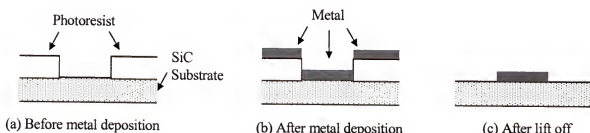


Figure 3-4 Lift-off procedure after the photoresist is deposited on the SiC substrate (a) before metal deposition, (b) after metal deposition, and (c) after the photoresist is removed, leaving the metal structure.

### 3.5 Contact Annealing

Since as deposited contacts were rectifying, the contacts were annealed using a commercial rapid thermal annealing (RTA) system (AG Associates, Model: Heat pulse 610). The samples were annealed in a nitrogen ( $N_2$ ) ambient (99.99%). To reduce contaminants, a 60-second nitrogen purge was performed before heating. The samples were placed on a silicon wafer susceptor with a thermocouple wire attached for monitoring and controlling the temperature. The typical heating rate used for the experiment was 60°C/second, which means the samples got to 1000°C within 20 seconds. After annealing, the samples were cooled inside the RTA chamber in flowing nitrogen until they reach a temperature below 100°C.

### 3.6 Characterization

Contacts on SiC were characterized in the as deposited and annealed states. Their electrical properties, surface composition, surface and interfacial morphology and interfacial reaction products were characterized by current-voltage (I-V) measurement, Auger electron spectroscopy (AES)<sup>50</sup>, scanning electron microscopy (SEM)<sup>50</sup>, X-ray diffraction (XRD) analysis, and transmission electron microscopy (TEM).<sup>50</sup>

#### 3.6.1 Electrical Characterization

The electrical properties of all contacts on SiC were investigated using room temperature current-voltage measurements between two isolated surface contacts. The current-voltage data were obtained by measuring the current flow between two adjacent top contacts under an applied voltage bias. The ohmic or rectifying nature of the contacts could be determined by the linearity of the I-V curves and total resistance values. A Keithley model 238 source measure unit was used for the I-V measurements. The set up

of the current-voltage measurement is shown in Fig. 3-6. The typical voltage bias range used was from  $-3$  V to  $+3$  V, with a step increment of  $0.02$  V. Electrical contacts to the samples was made using a Wentworth Labs probe station with Alessi Industry tungsten probes (tip diameter  $10\ \mu\text{m}$ ).

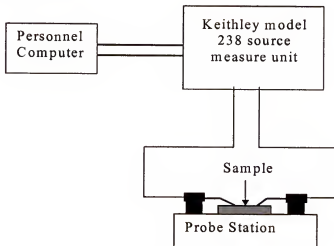


Figure 3-6 Schematic of the current-voltage measurement setup

Specific contact resistance data were determined using the CTLM pattern<sup>16</sup> described in Chapter 2 and shown in Fig. 3-2. The I-V data were obtained from each of the nine circular structures. This set of resistance ( $\Omega$ ) values (9 points) was plotted versus the contact separation,  $L$  (cm), as shown in Fig. 2-6. Linear regression of the I-V curves is used to find the slope, which is equal to

$$\frac{dR}{dL} = \frac{R_s}{W} \quad (3-1)$$

where  $W$  is the contact perimeter. The resistance intercept is  $2 \cdot R_c$  and the contact separation intercept equals twice the transfer length,  $2 \cdot L_T$ . The specific contact resistance ( $\rho_c$ ) is obtained from the following equation.<sup>16</sup>

$$\rho_c = \frac{R_c^2 \cdot W^2}{R_s} = R_s \cdot L_T^2 \quad (3-2)$$

The units for  $\rho_c$  are  $\Omega \text{ cm}^2$ .

### 3.6.2 Physical Characterization

Surface and layer composition, surface and interfacial morphology and interfacial reaction products were characterized using the following physical characterization techniques.

Scanning electron microscopy (SEM)<sup>50</sup> JEOL Model JEM 600, was used in the secondary or back scattered electron modes to characterize the surface morphology of the deposited film as a measure of the microstructural evolution and flaws that could affect contact resistance. Optical microscopy (OM) was also used for the surface morphology study and the microstructure evolution.

Auger electron spectroscopy (AES)<sup>50,51</sup> was used to determine the various elements present at the surface of contact samples. The surface was bombarded with a 10 keV electron beam. The electrons create inner quantum shell vacancies, which are filled with an electron decaying from a higher shell. The energy difference between these two levels is transferred to and causes ejection of another electron, the Auger electron. The Auger has a specific energy characteristic of the element. Due to energy loss, Auger electrons originating deeper than 3~4 atomic layers in the solid (5~20 Å) are inelastically scattered before reaching the surface and therefore can not be used for elemental identification. In this study, AES data were obtained from a Perkin-Elmer PHI 660 Scanning Auger Electron Multi probe in the N (E) mode. The primary energy used was 10 kV with a current of 100nA. AES may be combined with ion sputtering to clean the

surface as well as perform depth analysis.<sup>50,51</sup> The Auger electron intensities are plotted as a function of the sputtering time. The relative intensity changes give compositional information as a function of depth. Ar+ was used to sputter the surface for depth profile. Quantification of elemental concentrations in AES data is possible in cases where sensitivity factors have been measured in the same sample matrix.<sup>50,51</sup> The following equation is used for the calculation of elemental concentrations.

$$C_E (\%) = 100\% \times \frac{I_E / S_E}{\sum_X I_X / S_X} \quad (3-3)$$

, where  $I_E$  is analyte intensity,  $S_E$  is analyte sensitivity factor,  $I_X$  is intensity of other elements, and  $S_X$  is sensitivity factor of other elements in the samples.

X-ray diffraction (XRD)<sup>50</sup> was used to identify the phases formed at the contacts. A collimated beam of X-rays is incident on a specimen and is diffracted by the crystalline phases in the specimen according to Bragg's law ( $\lambda = 2d \sin\theta$ , where  $d$  is the spacing between atomic planes in the crystalline phase). The intensity of the diffracted beam is X-rays is measured as a function of the diffraction angle,  $2\theta$ , and the specimen's orientation. The time evolution of the interfacial phases was also studied as a function of metal structure and annealing condition. Since the metal films used in this study were thin (500~1000 Å), a glancing angle (1°) X-ray diffraction technique was employed to get enough X-ray intensities from the sample. The XRD data was obtained from a Phillips Model: PANalytical Hybrid X'pert MRD system with a Cu K $\alpha\&\beta$  averaged source.

Transmission electron microscopy (TEM)<sup>50</sup> was used to identify the phases, their distribution and microstructure formed at the contacts. A thin solid specimen is bombarded in vacuum with a highly focused, mono energetic beam of electrons. The

beam is of sufficient energy (200kV) to propagate through the specimen. A series of electromagnetic lenses magnify this transmitted electron signal. Diffracted electrons can be used to form a diffraction pattern to determine the atomic structure of the material. Transmitted electrons can be used to form images from small regions of the sample, due to several scattering mechanisms associated with interactions between electrons and the atomic constituents of the sample. A high resolution TEM system (JEOL JEM 2010F Field Emission Microscope) was used for the study. For TEM sample preparation, a focused ion beam (FIB, Model: FEI 210) technique was employed.<sup>50</sup> FIB TEM specimens prepared by the "lift-out" method provide a rapid means of preparing an electron transparent cross-section from a specific site of interest. A sample is inserted directly into the FIB chamber and a specimen created straight from the samples' surface. Two trenches are milled on either side of the site of interest, the area in the middle is thinned until it is electron transparent, and then the cross-section is cut free by the FIB. The specimen is then "lifted out" by the use of an electrostatic probe, which retrieves the free sample from its trench and deposits it on a TEM grid that is made up of copper covered with carbon thin films.

CHAPTER 4  
INTERFACIAL REACTIONS IN NICKEL/TITANIUM OHMIC  
CONTACTS TO N-TYPE SiC

4.1 Introduction

This chapter describes published research data, principles of the new tri layer metal scheme suggested in this study, and experimental results of this study. Many metal schemes for ohmic contact to n-SiC have been tried. Ni contacts have showed the most promising results in terms of contact resistance and stability but with a few issues also.<sup>5-7,32</sup>

The contact schemes described in this chapter consist of Ni based tri metal contacts and a few other combinations with different metals (Ti, Al and Au). After annealing, I-V curves were obtained from the samples. For the measurement of the specific contact resistance, CTLM patterns were used. Then, optical microscope (OM) pictures and Auger electron spectroscopy (AES) data (survey and depth profiles) were taken from each sample. XRD and TEM analysis were used for phase identification.

4.2 Published Results on Multi-Layer Metal Contacts

Ohmic contacts to n-type SiC have been formed from a variety of silicides, carbides and single metal elements.<sup>52-55</sup> Many single metal schemes have been tried including Ni, Ti, Ta, W, TiC and etc.<sup>54-61</sup> Nickel (Ni) based metal contacts has been proposed as the most suitable and promising candidate for the fabrication of ohmic metal contact to n-type 4H silicon carbide.<sup>40,43,56,62-66</sup> The n-type ohmic contacts based on nickel have currently been reported to have the lowest specific contact resistance ( $\sim 5 \times 10^{-7}$

$^6 \Omega \text{cm}^2$ )<sup>5</sup> and form stable and reproducible metal silicides at the interface during annealing.

But there are four major issues related to nickel based ohmic contacts to n-SiC.<sup>5-7</sup> The annealing process causes broadening and roughening of the metal SiC interface. Excess carbon segregation released from silicide reaction at the metal SiC interface results in the presence of graphite, and substantial roughening of the contact surface.

Ni diffusion into the SiC substrate causes excessive interfacial reactions deep into the substrate. This limits the achievement of a shallow junction depth for transistors. Interface roughness and interfaces broadening are issues for long-term reliability of the SiC devices. Interface oxidation degrades the device performance and creates difficulties in achieving and maintaining low ohmic contact resistance.

There have been many approaches to improve these issues, including the use of multi-layer metal structures. This includes Ni-Cr, Ni-Al and Ni-Si contact metallizations.<sup>8,9,30</sup> Some improvements have been reported in recent studies<sup>8,9,30</sup> as discussed in chapter 2. But all issues were not simultaneously improved, nor were the mechanisms leading to improvements adequately explained. The present study addresses some of these issues with respect to Ni/Ti/Ni ohmic contacts to n-type SiC.

#### 4.3 Principles of Tri Layer Metal Contacts in This Study

The ohmic contact metallization for this study was selected based on the following three principles. First, to obtain a reproducible and low specific contact resistance so that minimum voltages drop across the metal semiconductor junction can be achieved. Second, development of a uniform, shallow and abrupt metal semiconductor interface with lateral homogeneity of the interfacial phases was desired. Control of the interface

roughening and interfacial reactions were important aspects of the research. To obtain a uniform, shallow and abrupt metal semiconductor interface with homogeneous interfacial phases, metal diffusion into the substrate and interfacial reactions should be controlled.

Third, reduction of excess carbon at the interface after annealing was required for improving the high temperature stability. Minimizing Ni oxidation at the surface is a factor that determines the high temperature stability of ohmic contacts.

A tri metal scheme is investigated in this study to meet these requirements. First, the base metal lies in the middle of contact and forms an ohmic junction by formation of metal silicide. The bottom metal is located below the base metal and controls interfacial reactions and diffusion by extending the diffusion distance and forming a diffusion barrier. The bottom metal also forms carbide so it can reduce the excess carbon. The top metal minimizes oxidation of the base metal.

Since Ni reacts with SiC easily and forms a good nickel silicide with a low resistivity and stability, it is selected as the base metal for this ohmic contact to n-SiC. For the bottom metal film below the Ni layer, Ti and Al were investigated. Both can form carbides and oxide, which could control diffusion rates and reduce the excess carbon atoms. Ti, Al, Au, and Pt were studied for the top metal layer. Ti and Al are well known to form stable oxides ( $TiO_2$ ,  $Al_2O_3$ ) with a lower free energy of formation than  $NiO$ ,<sup>67,68</sup> thereby providing a protective oxide layer at the surface. Au and Pt are also good materials for the protection of the underlying materials due to their inert chemical nature.<sup>67,68</sup>

#### 4.4 Results of the Tri Metal Contact Scheme

Three metal schemes are chosen based on the principles described above, namely 8nmTi/100nmNi/20nmTi/SiC, 8nmAl/100nmNi/20nmAl/SiC, and 40nmAu/45nmPt/50nmNi/SiC. Ni is used as the base ohmic metal to Si, due to formation of a silicide phase after annealing. In the case of Au/Pt/Ni/SiC contact, Au and Pt are both used to minimize surface oxidation.

##### 4.4.1 Current-Voltage (I-V) Data

In figure 4-1 a), b) and c), current-voltage (I-V) data from the Al/Ni/Al/4H-SiC, Ti/Ni/Ti/4H-SiC, and Au/Pt/Ni/4H-SiC are shown, respectively. All three contacts were rectifying (not ohmic) as the as deposited state. Al/Ni/Al/SiC and Ti/Ni/Ti/SiC became ohmic after annealing at 1000°C for 2 min, based on the linear relationship between current and voltage (figure 4-1 (a) and (b)). The I-V data from a Au/Pt/Ni contact, as shown in figure 4-1 (c), was not linear either before or after annealing. In addition, the current level of the Au/Pt/Ni contact was also very low (on the order of  $10^{-3}$  A range).

The I-V curves of annealed Ti/Ni/Ti and Al/Ni/Al contacts on both 4H-SiC and 6H-SiC are shown in figure 4-2. The difference in the crystal structure for 4H versus 6H is described in chapter 2. In addition, there was a difference in the doping levels at  $1.2 \times 10^{19}$  atoms/cm<sup>3</sup> for 4H-SiC and  $1.1 \times 10^{18}$  atoms/cm<sup>3</sup> for 6H-SiC. The two contacts all became ohmic on both substrates regardless of the doping and SiC crystal type. The Ti/Ni/Ti contacts exhibited higher slopes for the I-V curves, which means a lower contact resistance as compared with the Al/Ni/Al contacts. Lower contact resistance for Ti/Ni/Ti versus Al/Ni/Al contacts presumably is related to the interface reactions that occurred during the annealing process, as discussed below.

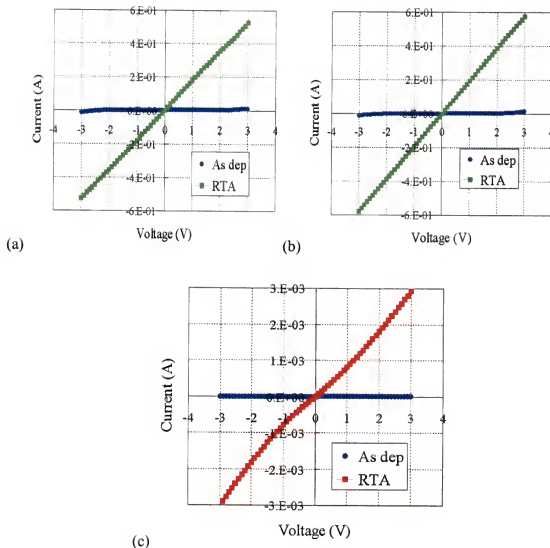


Figure 4-1 I-V data of the as deposited contacts and the contacts annealed at 1000°C, 2min, (a) Al/Ni/Al/4H-SiC, (b) Ti/Ni/Ti/4H-SiC, and (c) Au/Pt/Ni/4H-SiC.

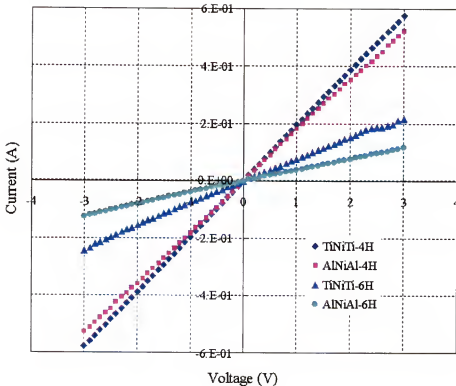


Figure 4-2 Comparison of the I-V data for Al/Ni/Al/SiC and Ti/Ni/Ti/SiC contacts on either 4H or 6H SiC after annealing at 1000°C, 2min in pure N<sub>2</sub>.

#### 4.4.2 Optical Microscopy Data

OM pictures of the Al/Ni/Al/4H-SiC, Ti/Ni/Ti/4H-SiC, and Au/Pt/Ni/4H-SiC contacts are shown in figure 4-3. For Au/Pt/Ni/SiC contacts, a very rough and discontinuous layer is observed. The layers on Al/Ni/Al/SiC and Ti/Ni/Ti/SiC contacts are still continuous and have metallic appearance in laboratory ambient light. Al/Ni/Al/SiC contacts were darker than Ti/Ni/Ti/SiC contacts. This could be related to larger roughness of the Al/SiC versus the Ti/SiC interface between SiC and contact layer.

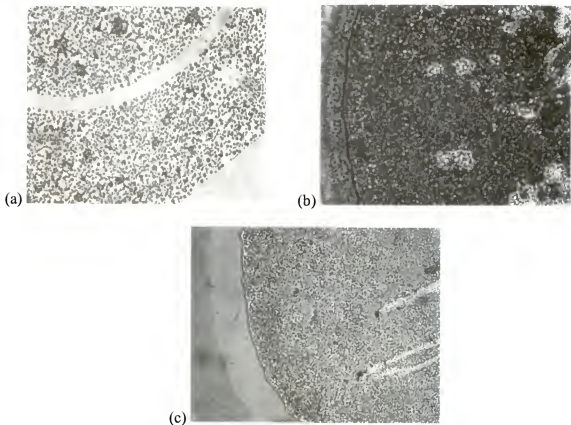


Figure 4-3 Optical microscope (OM) pictures of (a) Au/Pt/Ni, (b) Al/Ni/Al, and (c) Ti/Ni/Ti contacts annealed at 1000°C, 2min.

#### 4.4.3 Auger Electron Spectroscopy (AES)

Figure 4-4 shows AES depth profiles from Au/Pt/Ni, Al/Ni/Al, and Ti/Ni/Ti contacts, and extensive intermixing between the layers and/or diffuse interfaces (figure 4-4 (a)) are indicated for Au/Pt/Ni contacts. These AES data are consistent with the OM picture from Au/Pt/Ni contacts that showed a discontinuous layer (figure 4.3 (a)). As shown by I-V data (figure 4-1 and 4-2), Al/Ni/Al and Ti/Ni/Ti both formed ohmic contacts, with the Ti/Ni/Ti showing a lower contact resistance. However, they display very different trends in terms of the interface profiles. Figure 4-4 (b) and (c) show that the Al/Ni/Al/SiC contacts exhibited more diffuse interfaces between SiC and the contact metal layer than did Ti/Ni/Ti/SiC contacts. Since the breadth of the interfaces in the AES

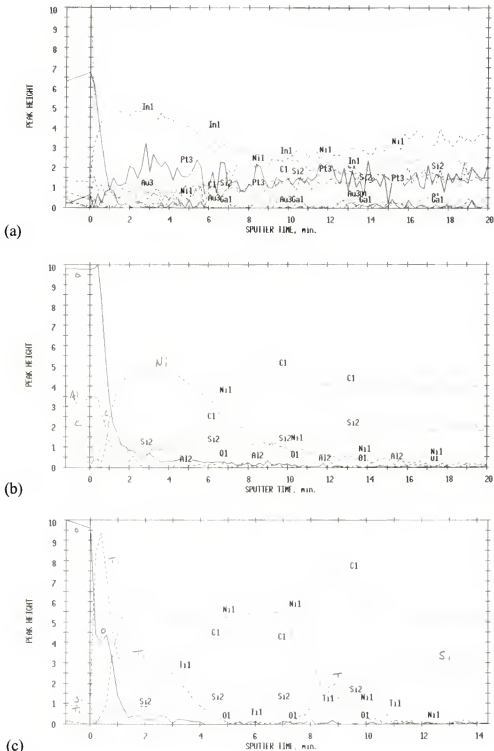


Figure 4-4 AES depth profiles of (a) Au/Pt/Ni, (b) Al/Ni/Al, and (c) Ti/Ni/Ti contacts after annealing at 1000°C, 2min.

depth profiles are related to both the roughness and interdiffusion,<sup>50,51</sup> in these contacts the Al/Ni/Al/SiC contacts are expected to have a rougher interface than those of Ti/Ni/Ti/SiC. These data could also be interpreted to mean that Ni can diffuse down deeper into SiC in Al/Ni/Al/SiC versus Ti/Ni/Ti/SiC contacts. These data show that Ti gives better performance than Al in terms of interfacial profiles. As a top metal layer, Ti also shows better results than Au/Pt in terms of protecting the Ni contact layer.

#### 4.5 Effects of Ni and Ti Layers on Ohmic Contact Formation

In the previous section, it has been shown that one (Ti/Ni/Ti/SiC) of the tri-metal contact structures provided good ohmic contacts to n-type SiC, with both interface morphology and contact resistance. The effects of each metal layer of the Ti/Ni/Ti structure on the ohmic contact formation have been investigated.

To understand the effects of each metal layer, different test structures were used, e.g. 8nmTi/100nmNi/20nmTi/SiC, 100nmNi/20nmTi/SiC, 110nmNi/SiC, and 20nmAu/100nmNi/20nmTi/SiC.

##### 4.5.1 Current-Voltage (I-V) Data

All of the as deposited contacts exhibited exponential I-V data typical for rectifying contacts, as shown in figure 4-5 (a). The total current levels were  $\sim 10^{-2}$  A. After annealing at 1000°C, 2min, in N<sub>2</sub>, linear straight lines are observed from the I-V data (Figure 4-5 (b)) indicating that Ti/Ni/Ti/SiC, Ni/Ti/SiC, Ni/SiC, and Au/Ni/Ti/SiC all turned to ohmic contact. This suggests that interfacial reactions occurred to form ohmic contacts.

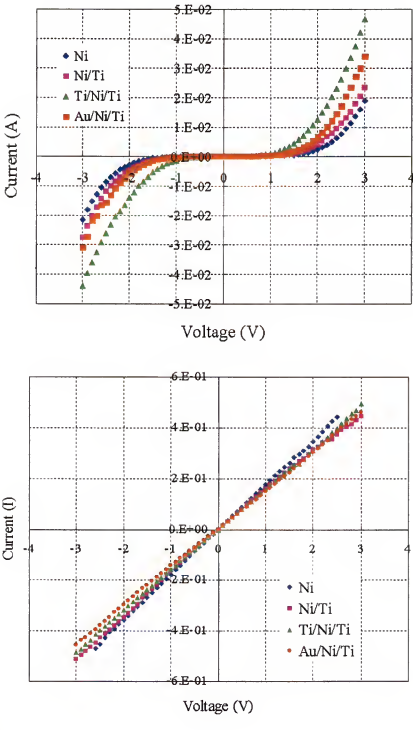


Figure 4-5 I-V data of (a) as deposited contacts and (b) contacts annealed at 1000°C, 2min.

Since Ni is known to react with SiC, the interfacial reaction could be related to formation of nickel silicide.<sup>30,40</sup> In terms of contact resistance values, the four contacts

show almost the same resistance. Therefore it is shown that metal layers other than Ni don't have a major effect on the formation of ohmic contact and contact resistance.

To evaluate contact resistance of the contacts, a CTLM pattern was formed on 100nmNi/20nmTi/SiC and 6nmTi/100nmNi/20nmTi/SiC contacts, due to their good I-V

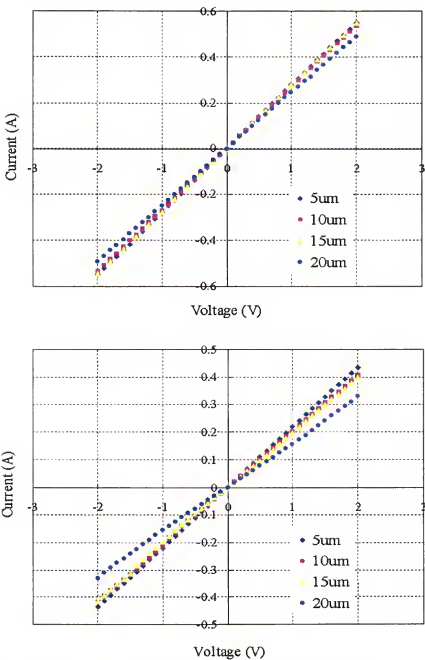


Figure 4-6 I-V data from the TLM patterns of (a) the Ni/Ti/SiC contacts, and (b) the Ti/Ni/Ti/SiC contacts, both of them annealed at 1000°C, 2min.

data and interface profiles (figure 4-9, 10). 1000nmNi/SiC (Ni-only) contacts were used for a reference data. I-V data were obtained from each sample with different gap spacing of the CTLM pattern. As displayed in figure 4-6, all spacing showed ohmic behavior as expected from the previous I-V data. After the TLM calculation as explained in chapter 2 and 3, the specific contact resistance ( $\rho_c$ ) of  $1 \times 10^{-4} \Omega \text{ cm}^2$  and  $2 \times 10^{-4} \Omega \text{ cm}^2$  for Ni/Ti and Ti/Ni/Ti contacts, respectively were obtained. The Ni-only contacts showed the specific contact resistance ( $\rho_c$ ) of  $1 \times 10^{-4} \Omega \text{ cm}^2$ . No significant difference in the specific contact resistance between contacts was found. This shows that Ni has major effects on the ohmic contact formation in Ni-based ohmic contacts.

#### 4.5.2 Optical Microscopy

OM pictures of Ti/Ni/Ti/SiC, Ni/Ti/SiC, Ni/SiC, and Au/Ni/Ti/SiC contacts are shown in figure 4-7. Ni/SiC contacts display a very dramatic change between the shiny as deposited and the dark, irregularly shaped surface features of the annealed samples (figure 4-7 (a) and (b)). After having Ti layer below Ni on contacts, a different trend is shown (figure 4-7 (d) and (e)). Ni/Ti/SiC and Ti/Ni/Ti/SiC contact were darker than as deposited contacts, but the general appearance remained a shiny metallic. Though interfacial reactions apparently occurred in these contacts to form ohmic junction, the surface (and presumably the interface) was more stable and smoother than a Ni-only contact. As shown from the I-V data in figure 4-5, Au/Ni/Ti/SiC contacts turned ohmic upon annealing, but the photos in figure 4-7 (f) show that a rough layer was observed.

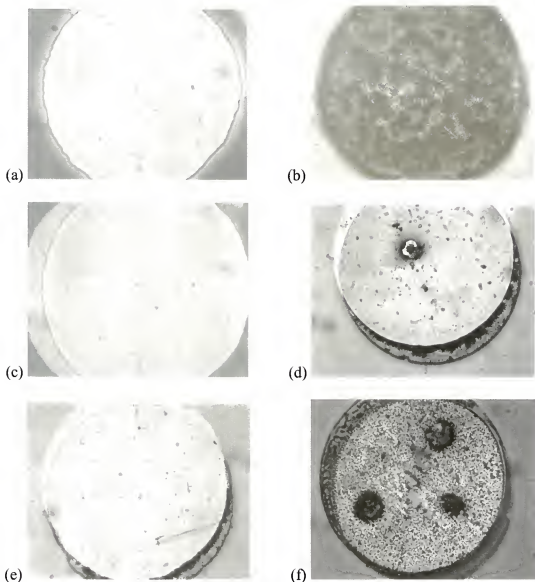


Figure 4-7 Optical Microscope pictures of (a) as deposited Ni/SiC contacts, (b) annealed Ni/SiC contacts, (c) as deposited Ni/Ti/SiC contacts, (d) annealed Ni/Ti/SiC contacts, (e) annealed Ti/Ni/Ti/SiC contacts, and (f) annealed Au/Ni/Ti/SiC contacts, (all anneals at 1000°C, 2min).

#### 4.5.3 XRD Data

For phase identification, X-ray diffraction (XRD) was used. Typical film thickness of this study was  $\sim 1000\text{\AA}$ . This was too thin for conventional XRD setup ( $\theta$ -2 $\theta$ ) to get enough X-ray intensity. A glancing incident angle ( $1^\circ$ ) technique was used to obtain

enough diffracted X-ray signals from the samples. XRD data of the Ni/SiC and Ti/Ni/Ti/SiC contacts are shown in figure 4-8. As-deposited Ti/Ni/Ti/SiC contacts spectrum show pure Ni peaks only (figure 4-8 (a)). This is confirmed by peak matching in figure 4-9 (a) (JCPDS: 04-0850). From the two annealed Ni/SiC and Ti/Ni/Ti/SiC contacts spectra, many different peaks appeared. Pure Ni peaks were not found from the annealed contacts. XRD peak matching shows that most of the peaks came from the nickel silicide phase ( $\text{Ni}_2\text{Si}$ ) (figure 4-9 (b), JCPDS: 73-2092). The  $\text{Ni}_2\text{Si}$  peaks were found in both annealed Ni/SiC and Ti/Ni/Ti/SiC contacts. Titanium carbide (TiC) peaks showed up from the annealed Ti/Ni/Ti/SiC contacts only (Figure 4-8 (b)).

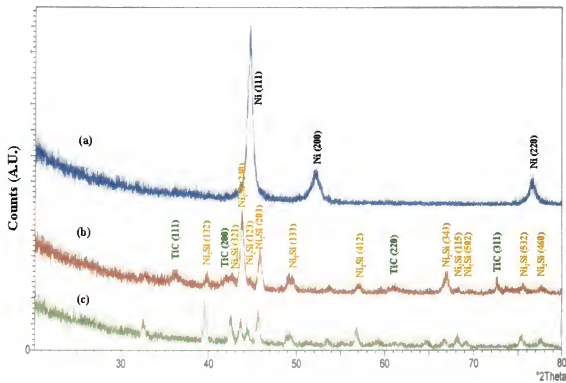


Figure 4-8 XRD data of the (a) as deposited Ti/Ni/Ti/SiC contacts and (b) annealed Ti/Ni/Ti/SiC contacts, and (c) annealed Ni/SiC contacts. Contacts annealed at 1000°C for 2min.

The annealed Ni/SiC and Ti/Ni/Ti/SiC contacts both have the same nickel silicide phase. The only difference was the TiC peak from the Ti/Ni/Ti/SiC contacts.

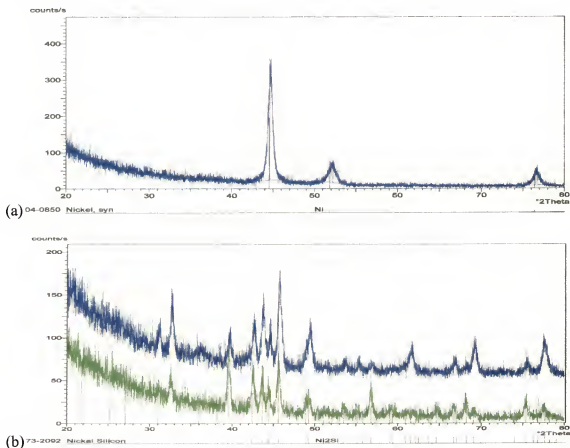


Figure 4-9 XRD peak matching data (a) Ni for as deposited contacts and (b) Ni<sub>2</sub>Si for annealed contacts.

#### 4.5.4 Auger Electron Spectroscopy (AES)

As shown by the I-V data, Au/Ni/Ti/SiC contacts became ohmic after annealing, whereas Au/Pt/Ni/SiC contact didn't. A rough layer was found for both surfaces, though the layers were more continuous in the Au/Ni/Ti/SiC contacts. AES depth profiles of the Au/Ni/Ti/SiC contacts show extensive layer intermixing and very diffuse interface profiles upon annealing (figure 4-10 (b)). Au is distributed throughout the contact layers and matches with Si profile. It is reasonable that a gold silicide (Au<sub>x</sub>Si) phase was

formed. The distribution of Ni, Si and carbon is similar to Ni/Ti/SiC contacts. After annealing Ti was found at the surface region along with a high oxygen concentration.

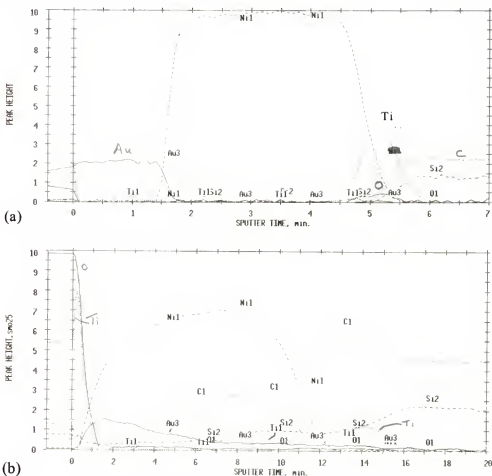


Figure 4-10 AES depth profiles of the Au/Ni/Ti/SiC contacts (a) as deposited, and (b) after annealing at 1000°C, 2min

As shown in the OM pictures, Ni-only contacts displayed very significant change between the as deposited and the annealed conditions (figure 4-7 (a) and (b)). AES depth profiles of the Ni/SiC contacts show the same trend in figure 4-11. The as deposited sample's profile shows very clear definition of the layers. The annealed contact shows extensive layer intermixing between Ni and SiC. Since both diffusion and roughness lead to diffuse interfaces in the AES depth profile, it is expected that the Ni/SiC contacts have rough interface or Ni diffused deep into SiC. The AES spectrum from the Ni-only

contacts found carbon, oxygen, Si, and Ni. Carbon was high at the outer surface, dipped to a low value where Ni and O were high presumably from surface NiO, and detected throughout the Ni layer. Carbon exhibited a peak at the interface between SiC and Ni. Si exists inside Ni layer and follows Ni profiles indicating the nickel silicide formation as shown from the XRD data (figure 4-8). The generation of carbon inside Ni (silicide) layer shows the nickel silicide reaction occurred in the contacts as well.<sup>8,39</sup>

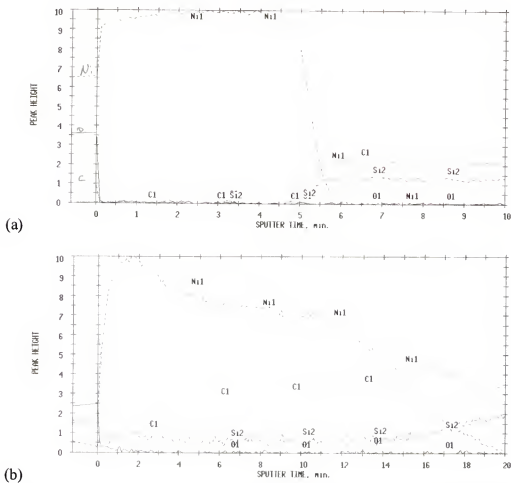


Figure 4-11 AES depth profiles of the Ni/SiC contacts (a) as deposited, and (b) after annealing at 1000°C, 2min.

After having Ti layer on contacts, the OM data showed that annealing of the Ti/Ni/Ti/SiC and Ni/Ti/SiC contacts did not change their color significantly, and shiny

metallic layers were maintained. This can be attributed to control of the interfacial reactions by the Ti layer between Ni and SiC.

AES depth profiles of the Ni/Ti/SiC contacts are shown in figure 4-12, and the interfaces of the annealed contacts are as easily identified as those in the as-deposited contacts. Ni in Ni/Ti/SiC contacts has a steeper interface with SiC than Ni-only contacts. The presence of Si inside Ni layer shows that a nickel silicide ( $Ni_2Si$ ) layer formed upon

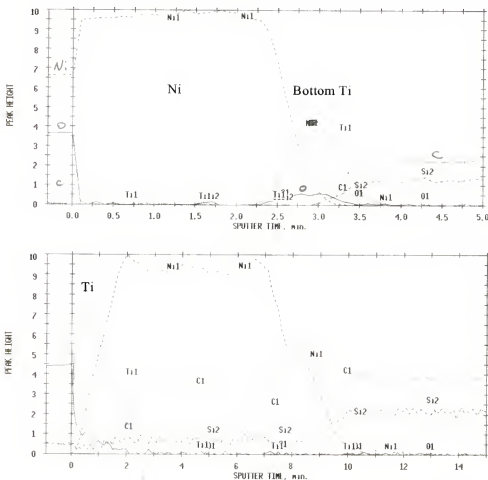


Figure 4-12 AES depth profiles of the Ni/Ti/SiC contacts (a) as deposited, and (b) after annealing at 1000°C, 2min.

annealing. The bottom Ti layer moved up to the surface, and Ni moved adjacent to SiC to form nickel silicide.

Carbon was distributed throughout the  $\text{Ni}_x\text{Si}$  layer leaving a peak located close to the silicide/SiC interface. The existence of excess carbon also suggests that nickel silicide reactions occurred in the contacts as the Ni-only contacts.

AES depth profiles from the as deposited and annealed Ti/Ni/Ti/SiC contacts are shown in figure 4-13. The changes in profiles are similar to the Ni/Ti/SiC contacts.

A clear definition of each interface is observed in figure 4-13 (b). Nickel shows a sharper interface with SiC than that in a Ni-only contact. Ni has two layers after annealing. Ni layer that diffused through bottom Ti exists below the bottom Ti layer. Small portion of the original Ni layer still exists between the bottom Ti and top Ti layers, which is the layer sequence as the as-deposited state. The formation of nickel silicide ( $\text{Ni}_2\text{Si}$ ) layer is evident from the Si signal distributed throughout Ni layers. Si in Ni layer follows Ni profiles suggesting silicide formation. Based on literature reports, silicide formation is the mechanism of forming ohmic contacts in Ni-based metallizations.<sup>38, 40</sup> Since the majority of Ni layer diffused to SiC and formed nickel silicide, the bottom Ti layer changed to a region closer to the surface. Carbon is distributed throughout the  $\text{Ni}_2\text{Si}$  and Ti layer leaving two peaks in Ni (or at the Ni/SiC interface) and a peak in bottom Ti layer (figure 4-10 (b)). The carbon generation in Ni-based contacts has been reported as well.<sup>8, 39</sup> Carbon profiles in Ni and Ti layers exhibit an interesting trend. Carbon inside Ni layer has high intensity where Ni is relatively low. This suggests that carbon didn't react with Ni and exists in a different phase. However, carbon in Ti layer shows the opposite trend. Carbon inside Ti layer increases where Ti intensity increases. This indicates formation of titanium carbide phase in Ti layer as shown from XRD data (figure 4-8). AES spectra from the surface before sputtering showed Ti, O and carbon,

but less carbon at the surface than in Ni/SiC and Ni/Ti/SiC contacts, probably due to titanium carbide formation below the surface. High oxygen and Ti peaks are observed at the surface region suggesting formation of titanium oxide. Due to the top Ti layer, the Ni signal is reduced in the surface region compared to the Ni/SiC and Ni/Ti/SiC contacts.

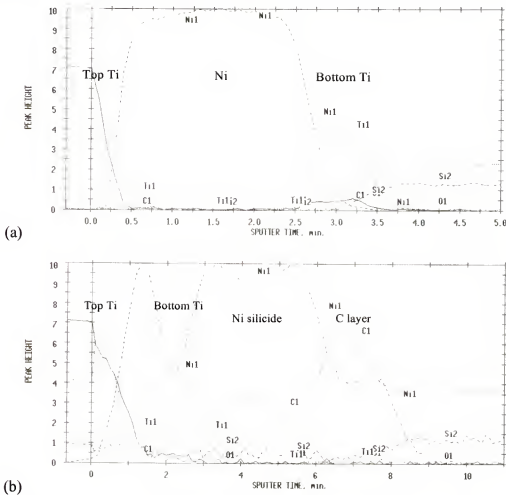


Figure 4-13 AES depth profiles of the Ti/Ni/Ti/SiC contacts (a) as deposited, and (b) after annealing at 1000°C, 2min.

Therefore, the steep interface profiles of the Ti/Ni/Ti/SiC and Ni/Ti/SiC contacts show the role of Ti layer on the contact profile formation.

#### 4.5.5 Auger Electron Spectroscopy (AES) : Chemical State Information

Previous AES data on the Ni/Ti/SiC and the Ti/Ni/Ti/SiC contacts revealed elemental redistribution inside the contacts. Also it provided possible interfacial reactions and their products. In order to deepen understanding on the interfacial reactions obtained from the previous AES data, it was required to investigate more detailed information on chemical states of the elements in each layer of the contacts. A combination of depth profiling and surface spectrum analysis was employed to obtain chemical state information of the elements in contacts. Based on the previous AES data, a center point of each layer was selected. After the first surface AES spectrum analysis, sputtering depth profiling was performed until the center point of the each contact layer was reached. The sputtering depth profiling was stopped and another AES spectrum was recorded. This cycle was repeated until the spectrum showed only SiC was present. If the characteristic binding energy of an element changes from spectrum (depth) to another, this is an indication that chemical state of an element has changed.<sup>50,51</sup> In addition to a characteristic energy shift of the Auger electron, a different Auger peak shape is also observed with a change in the chemical bonding.

For this AES study, good ohmic contacts with steep interface profiles were selected, i.e. Ni/Ti/SiC and the Ti/Ni/Ti/SiC contacts. For reference data, as-deposited samples were analyzed for the peak shape before the chemical state changed.

Figure 4-14 shows AES depth profile and spectra of the as deposited Ti/Ni/Ti/SiC contacts. Chemical states of the layers (top Ti, Ni, bottom Ti) in the contacts before annealing are discussed. The surface spectrum shows Ti, oxygen and carbon (figure 4-14(b)). The carbon shape matches that of surface contamination-organics and

hydrocarbons state or graphitic carbon (probably in surface contamination-organics state) (figure 4-15, 17).<sup>69</sup> As shown in figure 4-15, metallic Ti has higher peak at 418 eV than the peak at 387 eV. In the oxide case, the 387-peak is higher than the 418-peak. <sup>69-71</sup> The spectrum matches Ti in an oxide state (figure 4-14 (b)).<sup>72</sup> No Ni peak was detected at the surface suggesting no nickel oxidation at the surface of this structure. The top Ti layer shows oxygen and high Ti peaks (figure 4-14 (c)). The Ti peak shape shows that the 387-peak is still higher than the 418-peak, suggesting that the majority of Ti is in an

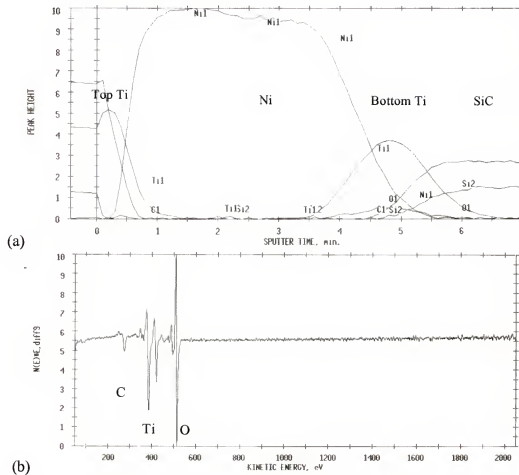


Figure 4-14 AES depth profile and spectra of the as deposited Ti/Ni/Ti/SiC contacts (a) depth profile, (b) surface, (c) Top Ti (d) Ni, and (e) Bottom Ti

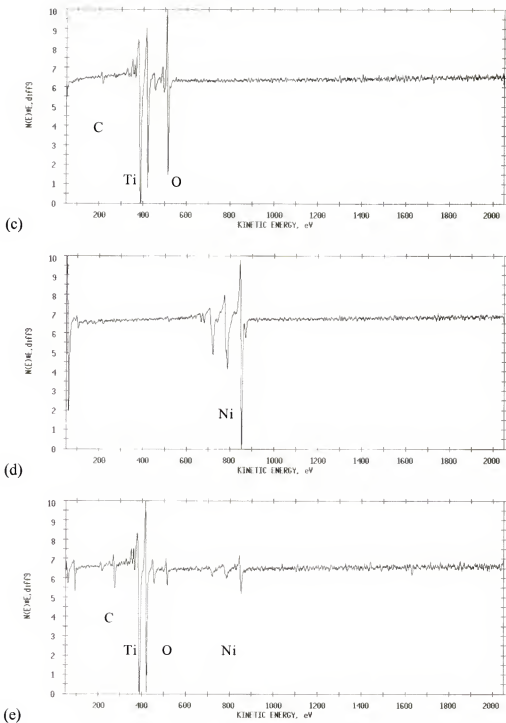


Figure 4-14 Continued

oxide state. However, the 387 to 418-peak ratio decreased compared to the surface data suggesting the existence of the metallic Ti in the top Ti layer. No Ni peak was detected

at the top Ti layer. Ni layer spectrum shows only Ni peaks (figure 4-14 (d)). Ni should be in metallic state. AES spectrum from the bottom Ti shows Ti, oxygen and carbon peaks (figure 4-14 (e)). The Ti peak shape is the same as the metallic showing a higher 387-peak than the 418-peak. The bottom Ti is in the metallic state. However, the presence of small oxygen peak suggests that small amount of Ti exists in an oxide phase in the bottom Ti layer.

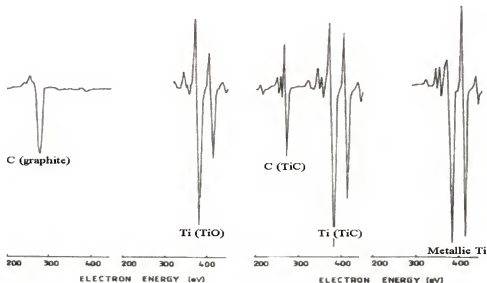


Figure 4-15 AES spectrum of titanium in metallic and carbide state, and carbon in graphite (organics) and carbide state<sup>69</sup>

AES depth profile and spectra from the as deposited Ni/Ti/SiC contacts are shown in figure 4-16. Carbon, Ni and oxygen were found from the surface spectrum suggesting the presence of nickel oxide (Figure 4-16 (b)), which was not found from the Ti/Ni/Ti/SiC contacts. Ni layer spectrum shows Ni (figure 4-16 (c)). Figure 4-16 (d) shows AES spectrum from the bottom Ti layer. The shape of the Ti peak is the same as the metallic showing a higher 387-peak than the 418-peak.

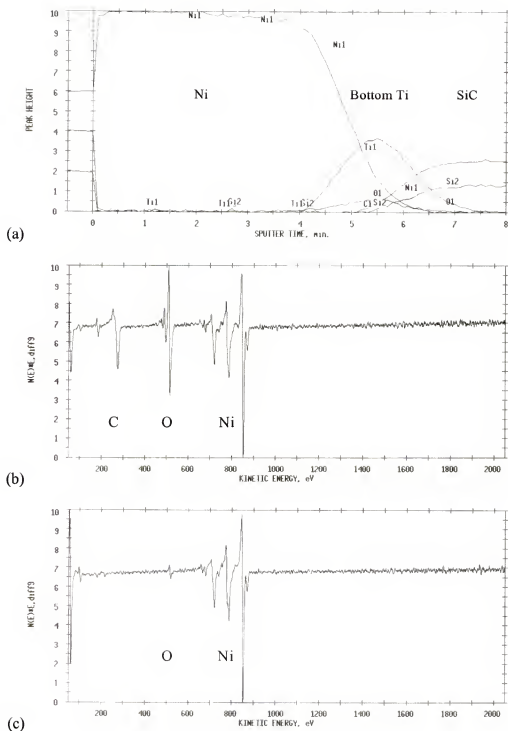


Figure 4-16 AES depth profile and spectra of the as deposited Ni/Ti/SiC contacts (a) depth profile, (b) surface, (c) Ni layer, and (d) Bottom Ti layer

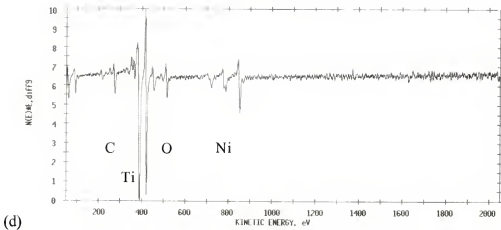


Figure 4-16 Continued

From the as deposited Ti/Ni/Ti/SiC and Ni/Ti/SiC contacts, the chemical states of the layers before annealing are shown. The top Ti (Ti/Ni/Ti/SiC only) was in an oxide state with a small portion of metallic Ti. The bottom Ti was in the metallic state, and Ni was probably in the metallic state as well. Ni/Ti/SiC contacts showed nickel oxide at the surface. In summary, the layer sequence of the as deposited Ti/Ni/Ti/SiC contacts can be represented as follows; Surface organics+ $\text{TiO}_x$  /  $\text{TiO}_x$ +Ti / Ni / Ti / SiC.

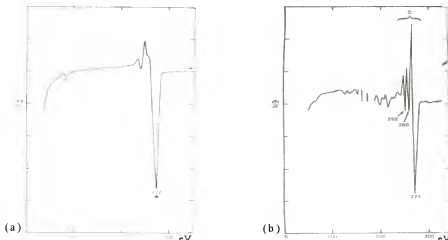


Figure 4-17 AES spectra of carbon in (a) graphite or surface contamination-organics and hydrocarbons, and (b) carbide state<sup>69</sup>

The previous OM data showed that after annealing the Ti/Ni/Ti/SiC contacts still showed metallic surfaces (figure 4-7). And AES data showed that interfaces of the contact remained smooth despite of the reactions that occurred to form an ohmic contact (figure 4-13). For example, Ni showed a steep interface with SiC. This is attributed to the role of Ti layer below Ni that controlled the interfacial reactions. The presence of Si inside Ni layer showed that nickel silicide ( $Ni_2Si$ ) layer formed after annealing, which has been the mechanism of the ohmic contact formation in Ni based contacts. The bottom Ti layer moved up to the surface, while Ni diffused to SiC substrate. As a result of the silicide reaction, the carbon atoms were liberated from the SiC substrate and distributed throughout the nickel silicide layer leaving carbon peaks around the interface between Ni and SiC. Formation of titanium carbide was also indicated as an interfacial reaction between Ti and the excess carbon. The Ti and oxygen on the surface suggested formation of titanium oxide. The surface data showed that Ni signal was reduced from surface region of the Ti/Ni/Ti/SiC contacts compared to the Ni/SiC and Ni/Ti/SiC contacts.

AES depth profiles and spectra from the annealed Ti/Ni/Ti/SiC contacts are shown in figure 4-18. Chemical states of the layers (top Ti, Ni, bottom Ti, and carbon in each layer) after annealing are discussed.

Surface spectrum found carbon, oxygen and Ti (Figure 4-18 (b)). As shown in figure 4-17 (a), the surface carbon was graphite or surface contamination-organics and hydrocarbons (probably surface contamination-organics).<sup>73-76</sup> Ti peaks show that they are in an oxide state (higher 387-peak in figure 4-15). These data suggest the existence of titanium oxide at the surface. AES spectrum from top Ti layer displays Ti as the major

peak (figure 4-18 (c)). Oxygen and carbon peaks were also found. Ti peak intensity increased and oxygen decreased compared to the surface spectrum. Ti peak shape was the same as the surface data (oxide state). Carbon peak changed to carbide shape that was shown in figure 4-17 (b).<sup>73-76</sup> These data suggest the formation of titanium oxide and titanium carbide in the top Ti layer.

In figure 4-18 (d), is shown AES spectrum from the bottom Ti layer. The bottom Ti was originally located below Ni layer. It moved between two Ni layers upon annealing, since the majority of Ni layer moved to SiC. Ti and carbon were the major peaks. Small nickel and oxygen peaks were also found. Carbon peak shape shows carbon in carbide state (figure 4-15, 17 (b)).<sup>73-76</sup> Ti peak shape showed carbide state as well (figure 4-15)<sup>74</sup>. Carbon peak increased significantly whereas oxygen decreased. Concentration of the elements in the bottom Ti layer was calculated as follows, carbon (38 %) and titanium (34.3 %) showing Ti to carbon ratio of 0.9:1. These data suggest that the majority of bottom Ti turned to titanium carbide (TiC).

AES spectrum from Ni layer shows Ni, Si, and carbon peaks, providing the concentration of nickel (50.4 %), silicon (27.2 %) and carbon (22.5 %) (figure 4-18 (e)). Ni to Si ratio was 1.85:1. Si signal follows the Ni peak. These indicate that a nickel silicide (Ni<sub>2</sub>Si) layer formed upon annealing. Carbon was distributed in the Ni layers. Carbon peak shape shows that the carbon is graphite or surface contamination-organics and hydrocarbons (figure 4-17 (a)). Considering that the carbon is located in the middle of contact layer and silicide reactions occurred, carbon is in graphitic carbon state.

AES spectrum from the carbon peak layer at the Ni<sub>2</sub>Si/SiC interface is shown in figure 4-18 (f). Carbon was the major element as expected. Ni and silicon peaks were

also found. The concentration of elements is as follows, carbon (53.5 %), nickel (30.9 %), and silicon (15.6 %). Ni to Si ratio was 1.98:1 showing the formation of  $\text{Ni}_2\text{Si}$  phase as the Ni layer. Carbon peak shape was the same as the carbon in Ni layer (graphitic carbon). Spectrum from SiC substrate was recorded to confirm carbon peak shape in carbide state after annealing (figure 4-18 (g)).

From the annealed Ti/Ni/Ti/SiC contacts, the chemical states of layers after annealing are discussed. The top Ti layer showed the formation of titanium oxide and titanium carbide. The formation of titanium carbide was indicated in the bottom Ti layer. The bottom Ti was in the metallic state before annealing. Ni and carbon peak layers showed the same phases (nickel silicide and graphite), except for the difference in the concentration ratio (more carbon in the carbon peak layer).

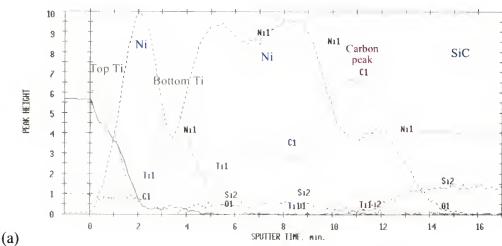


Figure 4-18 AES depth profile and spectra of the annealed Ti/Ni/Ti/SiC contacts (a) depth profile, (b) surface, (c) top Ti, (d) bottom Ti, (e)  $\text{Ni}_2\text{Si}$ , (f) carbon peak at the  $\text{Ni}_2\text{Si}/\text{SiC}$  interface, and (g) SiC substrate

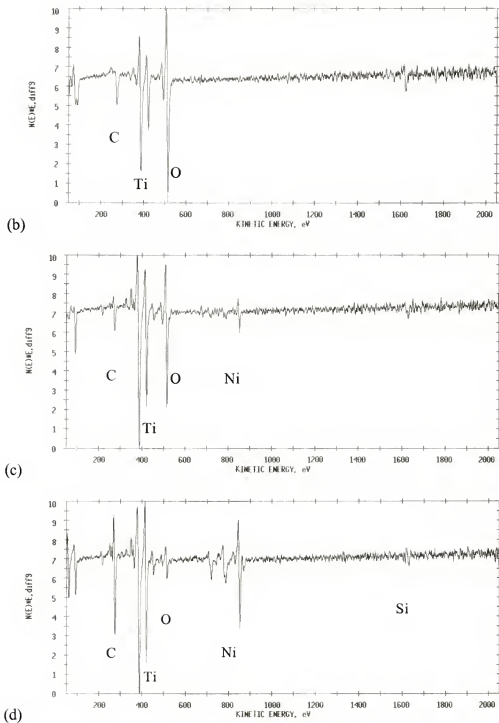


Figure 4-18 Continued

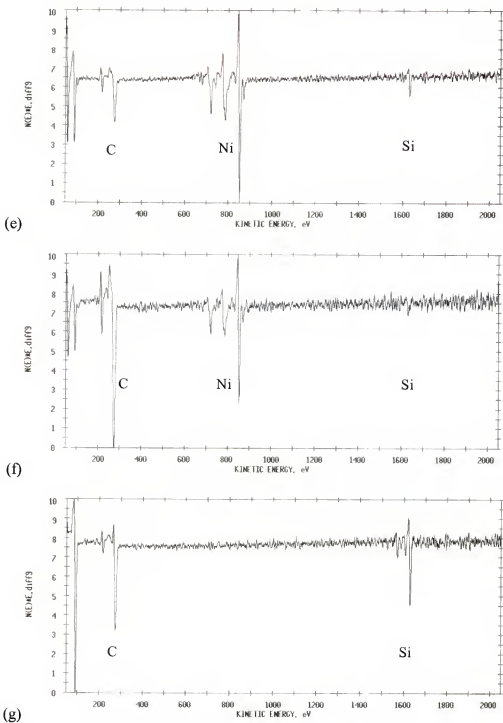


Figure 4-18 Continued

The previous OM data showed that after annealing the Ni/Ti/SiC contacts still showed metallic surfaces. AES data showed that interfaces of the contact remained smooth despite of the reactions that occurred to form an ohmic junction.

AES depth profile and spectra from the annealed Ni/Ti/SiC contacts are shown in figure 4-19. Interfacial reactions and phases are similar to the Ti/Ni/Ti/SiC contacts except for the top Ti layer. Carbon, oxygen and Ti peaks were found from surface spectrum (figure 4-19 (b)). Ti and carbon peaks suggest the existence of titanium oxide at the surface (figure 4-15, 17).<sup>74</sup> Figure 4-19 (c) shows spectrum from the bottom Ti layer. After annealing the bottom Ti moved on top of the Ni layer. Ti and carbon were the major peaks with the concentration of Ti (35 %) and carbon (37 %), providing Ti to C ratio of 0.95:1. Carbon and Ti peaks show formation of titanium carbide in the bottom Ti layer (figure 4-15, 17). Ni layer spectrum shows Ni, Si, and carbon peaks with the concentration of carbon (20.5%), nickel (52.8%), and Si (26.7%) (figure 4-19 (d)). Ni to Si ratio was close to 2:1 (1.98:1). The carbon peak shape and location suggest graphite formation (figure 4-17 (a)). Carbon peak layer spectrum shows carbon (45.3 %), nickel (36.0 %), and silicon (18.7 %) (figure 4-19 (e)). Ni to Si ratio was 1.93:1. Carbon peak shape indicates graphitic carbon as the carbon in Ni layer.

From the annealed Ni/Ti/SiC contacts, chemical state of the layers after annealing is discussed. The formation of titanium carbide was shown in the bottom Ti layer. Ni and carbon peak layers showed the same phases (nickel silicide and graphite), except for the concentration difference (more carbon in the carbon peak layer).

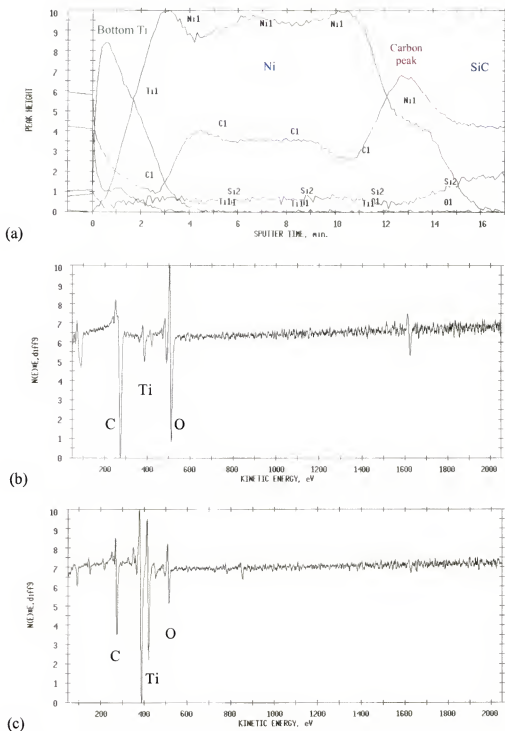


Figure 4-19 AES depth profile and spectra of the annealed Ni/Ti/SiC contacts (a) depth profile, (b) surface, (c) bottom Ti (d)  $\text{Ni}_x\text{Si}$ , and (e) carbon peak layer at the  $\text{Ni}_x\text{Si}/\text{SiC}$  interface

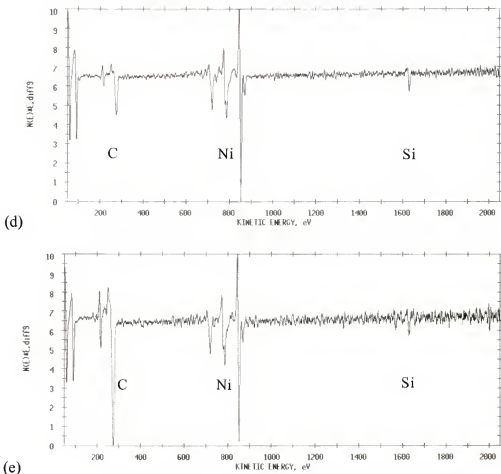


Figure 4-19 Continued

#### 4.5.6 Transmission Electron Microscopy (TEM)

As shown in the I-V, AES and XRD data, after annealing contacts turned to ohmic as a result of the interfacial reactions. Interfacial reactions also changed layer sequence and interfacial phases. Cross-sectional TEM analysis was used to confirm the layer sequence and interfacial morphology.

Cross-sectional TEM pictures of the annealed Ni/SiC and Ti/Ni/Ti/SiC contacts are shown in figure 4-20. The annealed Ni/SiC contacts show very rough interfaces between layers including the nickel silicide/SiC interface (figure 4-20 (a)). Nickel silicide and carbon layers are shown in the figure. This result indicates that the diffuse interface

profiles shown from the AES data (figure 4-9) are related to physically rough interfaces. Clear and smooth interfaces between SiC and nickel silicide layers are observed from the Ti/Ni/Ti/SiC contacts (figure 4-20 (b)). Clear phase separations between nickel silicide and titanium carbide layers are shown as well. TEM pictures confirm layer inversion between Ni and Ti layers in the Ti/Ni/Ti/SiC contacts. As the as-deposited state, Ni layer was placed on top of bottom Ti. After annealing they changed their position. Ni as a silicide phase exists below Ti layer in a carbide phase. The carbon peak layer is also seen

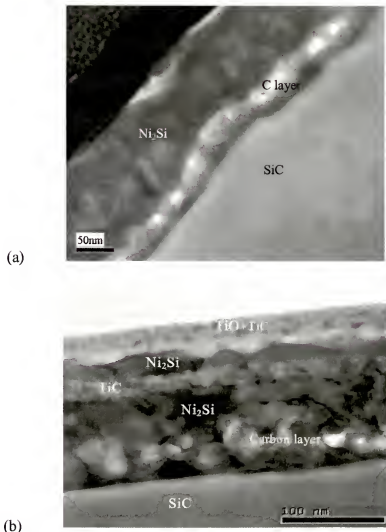


Figure 4-20 Cross-sectional TEM data of the (a) Ni/SiC contacts and (b) Ti/Ni/Ti/SiC contacts. Both annealed at 1000°C for 2min.

at the nickel silicide/SiC interface (figure 4-20 (b)). Carbon exhibits light color on the bright field image of TEM due to less electron scattering of carbon than heavy elements.<sup>50</sup>

The roughness of nickel silicide/SiC interfaces is measured from the TEM images. The average of measured roughness values is calculated for the annealed Ni/SiC and Ti/Ni/Ti/SiC contacts. The average interface roughness was  $25.9 \pm 6.4$  nm and  $7.5 \pm 2.3$  nm from the Ni/SiC and Ti/Ni/Ti/SiC contacts, respectively. These data show the effects of Ti layer on the interface profiles of nickel/titanium contacts.

Figure 4-21 shows TEM EDX data on the nickel silicide, titanium carbide, and carbon peak layers of the annealed Ti/Ni/Ti/SiC contacts. EDX data of the silicide layers

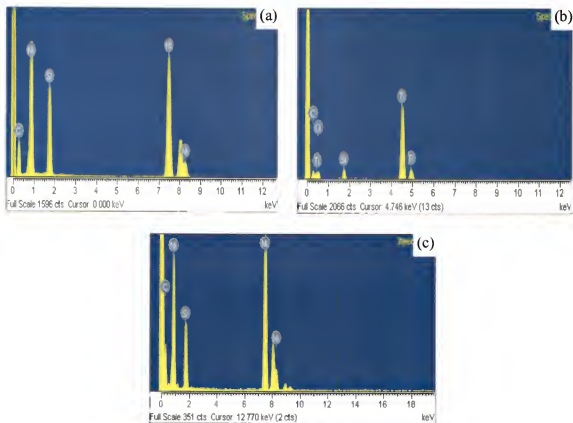


Figure 4-21 TEM EDX data of the Ti/Ni/Ti/SiC contacts annealed at 1000°C for 2min. (a) on Ni<sub>2</sub>Si layers, (b) on TiC layers, and (c) C layers

show Ni, Si and carbon, and the carbide layers show Ti, carbon and some oxygen as expected. Carbon layer shows the same elements as Ni silicide layer. The EDX data are consistent with the TEM images and the AES data.

#### 4.6 Discussion

A new tri metal Ti/Ni/Ti scheme for ohmic contacts to n-type SiC has been investigated in this study to meet the requirements described in the section 4.3. Specific contact resistance of  $1 \times 10^{-4} \Omega \text{ cm}^2$  was obtained from the Ni/SiC contacts upon forming the Ni<sub>2</sub>Si phase. However, these Ni/SiC contacts exhibited rough interfaces as shown from TEM (figure 4-20) and AES data (figure 4-9).

Ti/Ni/Ti/SiC contact structures provided good ohmic contacts to n-type SiC, with both a smooth interface morphology and a low contact resistance. A nickel silicide phase was formed in the Ti/Ni/Ti/SiC contacts providing a low specific contact resistance ( $\rho_c$ ) of  $2 \times 10^{-4} \Omega \text{ cm}^2$ . No significant difference in contact resistance was found between the Ni/SiC and Ti/Ni/Ti/SiC contacts. However, smooth interfaces were only obtained when using Ti layer below Ni. The AES, XRD, and cross-sectional TEM provided detailed information on the interfacial reactions and their products relative to the layer sequence of Ti/Ni/Ti/SiC contacts. The interfacial reactions caused dramatic changes in the layer sequence and the interfacial phases of contacts upon annealing. Based on the data presented in this chapter, a schematic model of the interfacial layers on the Ti/Ni/Ti/SiC contacts is deduced, as shown in figure 4-22. The as-deposited Ti/Ni/Ti/SiC contact shows a top Ti, intermediate Ni and bottom Ti layers on SiC (figure 4-22 (a)). Surface organics and titanium oxide exist at the surface of both contact schemes. After annealing, a very different layer sequence is observed (figure 4-22 (b)). For annealed contacts, TiO

and TiC phases were in the top Ti layer. A thin nickel silicide layer and a carbon layer follow. The bottom Ti layer reacted with carbon and became a TiC layer. The TiC layer was on top of nickel silicide layer. Ni reacted with Si and formed nickel silicide ( $Ni_2Si$ ) leaving carbon as a reaction product. A carbon layer was formed at the silicide/SiC interface.

	$C$ (organics) + $TiO$	
Top Ti	$Ti + TiO$	
	$Ni$	
Bottom Ti	$Ti + TiO + TiC$	
	$SiC$	
(a)		
	$C$ (organics) + $TiO$	
	$TiC + TiO$	
	$Ni_2Si + C$ (graphite)	
	TiC	
	$Ni_2Si + C$ (graphite)	
	$C$ (graphite) + $Ni_2Si$	
	$SiC$	
(b)		

Figure 4-22. A schematic model of the Ti/Ni/Ti/SiC contacts. (a) as deposited and (b) after annealing

The layer sequence suggests possible interfacial reactions and their products. The interfacial reactions involved in the formation of ohmic Ti/Ni/Ti/SiC contacts are summarized as follows. Upon annealing first, Ni moves to the SiC interface. It is difficult for the bottom titanium layer to move to the surface. The titanium layer has oxygen and carbon in the as deposited state due to its strong oxygen and carbon affinity. Once Ni atoms reaches the SiC, Si atoms are liberated from SiC and start forming nickel silicide.<sup>64</sup> The chemical reaction is represented by the following equation.



In the case of Ni/Si contacts,  $\text{Ni}_2\text{Si}$  forms at 250°C, transforming to  $\text{NiSi}$  at 400°C and  $\text{NiSi}_2$  at 800°C.<sup>38</sup> Ni/SiC contacts require higher temperatures to cause the initial reaction, therefore more metal rich silicides are formed first.<sup>38</sup> In forming silicides on SiC, the free energy of the reaction is equal to the free energy of formation of the silicide minus the free energy formation of SiC. Thus, in the case of reactions with SiC, silicide phase requiring less SiC dissociation will be favored relative to reactions with elemental Si for any given silicide.<sup>38,40</sup> Also the Ni-Si-C phase diagram shows that  $\text{Ni}_2\text{Si}$  is the only silicide in equilibrium with both C and SiC.<sup>40,64</sup>

In terms of silicide formation from reactions with SiC, Ohdomari et al,<sup>39</sup> reported that Ni carbide was not detected. Single-phase polycrystalline  $\text{Ni}_2\text{Si}$  was formed as the only reaction products. Pai et al.<sup>38</sup> reported the formation of  $\text{Ni}_2\text{Si}$  phase after 700°C, 30 min annealing in vacuum. Crofton et al.<sup>5</sup> concluded that after a 2 min annealing at 950°C in a vacuum, a Ni film on 6H-SiC turns into  $\text{Ni}_2\text{Si}$ . All existing studies thus show that this  $\text{Ni}_2\text{Si}$  phase is independent of the poly type, the doping of the SiC and the details of the annealing cycle, as long as the system has had the opportunity to reach its thermodynamically stable state.<sup>40</sup> The time-temperature cycle and the vacuum conditions may affect the kinetics and the pathway of the reaction. This in turn could change the morphology of the carbon and silicide in the final state.<sup>40</sup>

Carbon is liberated from SiC as a result of the silicide reaction.<sup>8,39</sup> In this study, the excess carbon diffused to the bottom Ti layer and formed titanium carbide (TiC). The possible reaction is shown below.



Carbon atoms move to the top Ti layer as well, forming titanium carbide. Thus the top Ti layer shows titanium carbide as well as oxide. As the titanium carbide layer forms, the TiC layer provides a barrier for the Ni diffusion.<sup>39</sup> This leaves the Ni layer between two TiC layers after annealing.

In addition to the titanium carbide formation, carbon in excess of that consumed to form TiC is distributed in the nickel silicide layer and forms a carbon layer at the silicide/SiC interface. Since the carbon layer exists as an independent phase in the nickel silicide,<sup>8,39</sup> it is reasonable that a phase separation is important in the development of the morphology. This phase separation results in a carbon layer (band structure) to minimize the carbon diffusion distance and the interfacial area between the silicide matrix and carbon precipitates, as shown from the TEM data (figure 4-20). AES and TEM EDX data confirmed the composition of the carbon layers. More discussion on the carbon layer formation is provided in chapter 5. Ohdomari et al.<sup>39</sup> observed at 600°C that Ni<sub>2</sub>Si forms, carbon bonds are found to be graphitic and the carbon concentration is described as being constant throughout the reacted film, except near the Ni<sub>2</sub>Si/SiC interface. Marinova et al.<sup>8</sup> also observe a carbon peak at the Ni<sub>2</sub>Si/SiC interface in an X-ray photoemission profile of a sample annealed in an N<sub>2</sub> atmosphere for 10 min at 950°C. Ohi et al.<sup>43</sup> reported that carbon atoms existed in the reacted region as graphite, and the graphite was composed of fine grains, because crystalline graphite was not detected by X-ray diffraction.

In order to understand the silicide reaction, thermodynamic properties and a diffusion parameter are considered. Table 4-1 lists common metal elements, including Ni, for ohmic contacts to n-SiC and their thermodynamic and diffusion property at high

annealing temperature.<sup>67,68,77-79</sup> They all show that the free energy of silicide formation is lower than that of SiC. Ni, Ti and Mo silicide have very low free energy of

Table 4-1 Thermodynamic and diffusion properties of metals for ohmic contacts to SiC<sup>18,67,68,77,79-83</sup>

Metal s	Stable phases with SiC	Resistivity of silicides ( $\mu\Omega\text{cm}$ )	$\Delta G_f$ (KJ) of silicide at 1000°C (SiC: -54 KJ)	Moving species in silicide reaction	$T_m$ (°C) of silicide	$\Delta G_f$ (KJ) of oxide at 1000°C
Co	CoSi	30~86	- 87.5	Si	1460	- 426.2
Cr	CrSi <sub>2</sub>	~600	- 74.0	Si	1490	NA
Fe	FeSi	240~287	- 71.9	Si	1410	- 688.4
Mo	MoSi <sub>2</sub>	90~100	- 130.6	Si	2020	- 415.4
Ni	Ni <sub>2</sub> Si	20~25	- 140.0	Ni	1318	- 131.7
Pd	Pd <sub>2</sub> Si	25~35	- 86.3	Pd	1330	~- 10
Ta	TaSi <sub>2</sub>	35~80	- 114.8	Si	2040	- 1522.9
Ti	TiSi <sub>2</sub>	20~25	- 126.1	Si	1540	- 700.4
W	WSi <sub>2</sub>	30~100	- 91.3	Si	2160	- 373.4
Pt	Pt <sub>2</sub> Si	~35	- 86.2	Pt	1100	- 157.8

formation, which suggests they can form silicide on SiC. Ni silicide shows lower free energy of formation than that of Ti silicide. Therefore, Ni should form a silicide more readily than Ti on the Ti/Ni/Ti/SiC contacts.

In terms of the diffusing species, metal elements should move during the silicide reaction in order to achieve a smooth and uniform interface after the interfacial reaction.<sup>77,79</sup> The diffusion of Si atoms to create silicides creates defects and voids (Kirkendall) at the metal semiconductor interface, resulting in a rough interface. Ni and

Pd have an advantage in this aspect. These data show that Ni has many advantages as an ohmic metal in terms of thermodynamic and diffusion properties.

In this study, no titanium silicide has been found on the contacts. This is an interesting considering that Ti has been widely used to form ohmic contacts to Si and SiC.<sup>53,54,57,58,61,84,85</sup> Titanium silicide forms on Si and SiC and has shown low contact resistance values. To investigate this possibility, thermodynamic parameters are calculated for possible interfacial reactions. Table 4-2 shows thermodynamic calculations for the bottom Ti and other metals that form carbide phases. It is shown that titanium and nickel make a good combination in forming silicide and carbide. Titanium carbide has lower free energy of formation than titanium silicide suggesting titanium forms carbide phase more readily than its silicide. Ni silicide shows lower free energy of formation than Ti silicide. This free energy of formation data provided a nickel silicide

Table 4-2 Thermodynamic properties of elements for the bottom metal (Ti) of the Ti/Ni/Ti/SiC contacts to SiC<sup>18,67,68,77-79,86</sup>

Metals	Stable phases with SiC	Resistivity ( $\mu\Omega\text{cm}$ )	$\Delta G_f(\text{KJ})$ at 1000°C (SiC: -54 KJ)	$T_m(\text{°C})$ silicides carbides	$\Delta G_f(\text{KJ})$ of oxide at 1000°C ( $\text{SiO}_2$ : - 687.8)
Hf	$\text{HfSi}_2$ $\text{HfC}$	45~70 39	NA	2142 3950	$\text{HfO}_2$ : - 878.3
Ni	$\text{Ni}_2\text{Si}$ -	20~25 -	- 140 -	1318 -	$\text{NiO}$ : - 131.7
Ti	$\text{TiSi}_2$ $\text{TiC}$	20~25 62	- 126.1 - 170.3	1500 3067	$\text{TiO}_2$ : - 700.4
Ta	$\text{TaSi}_2$ $\text{TaC}$	35~45 22	- 114.8 - 139.6	2040 4000	$\text{Ta}_2\text{O}_5$ : - 1522.9
W	$\text{WSi}_2$ $\text{WC}$	30~100 ~20	- 91.3 - 35.2	2160 2747	$\text{WO}_2$ : - 373.4
Zr	$\text{ZrSi}_2$ $\text{ZrC}$	35~40 ~50	- 161.2 - 187.9	1620 3420	$\text{ZrO}_2$ : - 868.6

and a titanium carbide phases on the Ti/Ni/Ti/SiC contacts. Titanium oxide can take oxygen from SiC and Ni preventing oxidation of nickel and SiC substrate.

#### 4.7 Summary

A new tri Ti/Ni/Ti metal scheme for ohmic contacts to n-type SiC has been investigated. Ti/Ni/Ti/SiC contact structures provided good ohmic contacts to n-type SiC, with both smooth interface morphology and low contact resistance. A nickel silicide phase (Ni<sub>2</sub>Si) was formed on the Ti/Ni/Ti/SiC contacts providing a specific contact resistance ( $\rho_C$ ) value of  $1 \times 10^{-4} \Omega \text{ cm}^2$ , which was the same as the contact resistance of Ni-only contacts. However, a smooth interface was obtained using a bottom Ti layer below Ni. Interface roughness of  $25.9 \pm 6.4 \text{ nm}$  and  $7.5 \pm 2.3 \text{ nm}$  were measured for Ni/SiC and Ti/Ni/Ti/SiC contacts, respectively. The interfacial reactions caused dramatic changes in the layer sequence and the interfacial phases of contacts upon annealing. A schematic model of the interfacial layers on the Ti/Ni/Ti/SiC contacts was deduced. The annealed contacts show that a top Ti layer has TiO<sub>X</sub> and TiC phases. A thin nickel silicide layer and a carbon layer follow. The bottom Ti layer turned to TiC layer. Ni reacted with Si and formed nickel silicide (Ni<sub>2</sub>Si) leaving carbon as a reaction product. A carbon layer formed at the silicide/SiC interface.

The layer sequence suggests possible interfacial reactions and their products, as follows. Upon annealing, Ni moves to the SiC interface and liberates Si atoms from SiC to form a nickel silicide phase. Carbon is liberated from SiC as a result of the silicide reaction. In this study, carbon diffuses to the bottom Ti layer and forms a titanium carbide (TiC) phase. Carbon atoms move to the top Ti layer as well, forming titanium carbide. Thus the top Ti layer shows titanium carbide as well as oxide. As the bottom

titanium carbide layer forms, it provides a barrier for the Ni diffusion. This leaves a Ni layer between two TiC layers after annealing. In addition to the titanium carbide formation, the liberated carbon is distributed in the nickel silicide layer as a carbon phase, and forms a graphitic carbon layer at the silicide/SiC interface. This appears as a carbon layer (band).

Ni silicide has a lower free energy of formation than that of Ti silicide. Therefore, Ni can form a silicide more readily than Ti in the Ti/Ni/Ti/SiC contacts. In terms of the diffusing species during diffusion, Ni also has advantage since it is known to be the fastest moving species. These data show that Ni has many advantages as the ohmic metal in terms of thermodynamic and diffusion properties. Titanium and nickel also are complementary in forming silicide and carbide. Titanium carbide has a lower free energy of formation than titanium silicide suggesting titanium forms carbide phase more readily than its silicide. Ni silicide shows lower free energy of formation than Ti silicide. Thus nickel silicide and titanium carbide phases are formed in the Ti/Ni/Ti/SiC contacts.

CHAPTER 5  
THE EFFECTS OF NICKEL AND TITANIUM THICKNESS  
ON NICKEL/TITANIUM OHMIC CONTACTS TO SiC

5.1 Introduction

In the previous chapter, it was reported that Ti/Ni/Ti/SiC contact showed good ohmic contact properties and appeared to be a promising candidate for contact to n-type 4H-SiC. This chapter describes a study on the effects of Ni and bottom Ti layer thickness on the ohmic contact formation of titanium/nickel/titanium contacts with a constant thickness top Ti layer. After annealing, I-V data was obtained. For specific contact resistance, a CTLM pattern was used. Optical microscopy (OM) and Auger electron spectroscopy (AES) data were taken. For phase identification, X-ray diffraction (XRD) was used. Since the films used in this study were thin ( $\sim 1000\text{\AA}$ ), a glancing incident angle technique was used to increase the signal to noise ratio for XRD. Cross-sectional transmission electron microscope (XTEM) was used to identify the interface phase morphology.

5.2 Effects of Ti Thickness

The effects of bottom Ti thickness on the ohmic contact formation of titanium/nickel/titanium contacts were investigated varying bottom Ti thickness from 0 nm to 30 nm. The same thickness (6nm) was used for the top Ti layer.

5.2.1 Current and Voltage (I-V) Data

Current-voltage (I-V) data of the Ti/Ni/Ti/4H-SiC contacts with different Ti

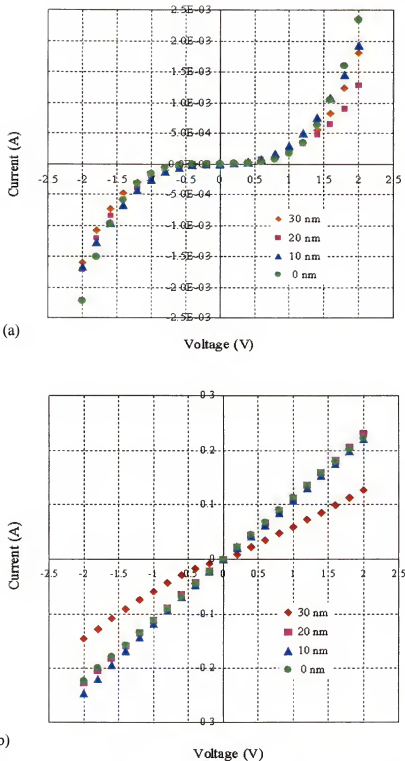


Figure 5-1 I-V data of the contacts with different bottom Ti thickness (a) as deposited contacts and (b) annealed contacts

thickness between 0 and 30 nm are shown in figure 5-1. All four contacts were rectifying as the as-deposited state. Three contact structures became ohmic upon annealing at 1000°C for 2 min (figure 5-4 (b)), while the data from 30 nm Ti was not linear. Contacts with 20 nm, 10 nm, and 0 nm bottom Ti showed linear I-V data and the same slope (figure 5-1 (b)). CTLM data showed the specific contact resistance ( $\rho_C$ ) are  $3 \times 10^{-4} \Omega \text{ cm}^2$ ,  $4 \times 10^{-4} \Omega \text{ cm}^2$  and  $1 \times 10^{-4} \Omega \text{ cm}^2$  for contacts with 0 nm, 10 nm and 20 nm Ti, respectively. When forced to fit a straight line, the contacts with 30 nm Ti showed a specific contact resistance ( $\rho_C$ ) of  $2 \times 10^{-3} \Omega \text{ cm}^2$ .

### 5.2.2 Optical Microscopy

As deposited samples show smooth, shiny metallic surface (figure 5-2 (a) and (b)), and the contacts with 30 nm Ti remain smooth and shiny after annealing, except for a few dark spots (figure 5-2 (c), (d)) which suggest that the contacts have begun to diffuse and react at the interface. Contacts of 20 nm Ti show color changes upon annealing, which are probably due to interfacial reactions, but the layers are continuous and smooth (figure 5-2 (e), (f)). As the Ti thickness decreases (10 nm Ti), the color of contacts becomes

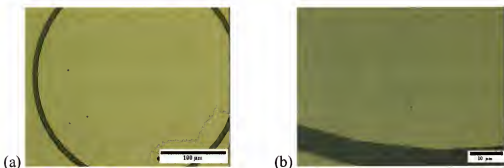


Figure 5-2 OM pictures of the contacts with different Ti thickness. (a)&(b) as deposited contacts, balance from annealed contacts with Ti thickness of (c)&(d) 30 nm, (e)&(f) 20 nm, (g)&(h) 10 nm, and (i)&(j) 0 nm.

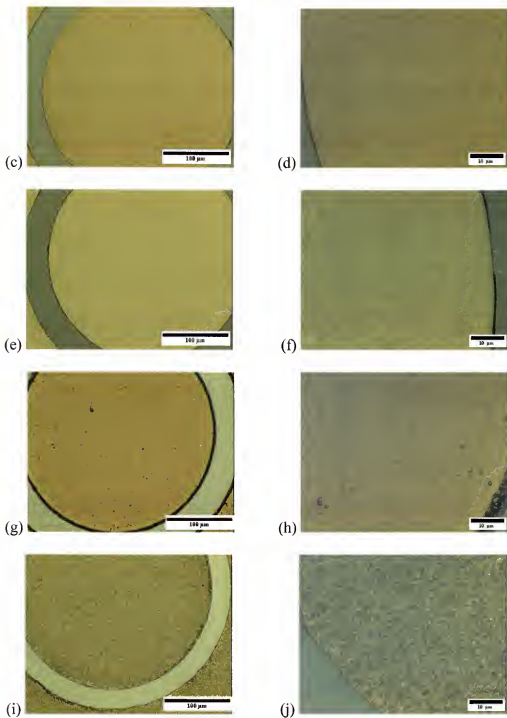


Figure 5-2 Continued

darker (figure 5-2 (g), (h)), and the Ni-only contacts display many dark spots (figure 5-2 (i), (j)).

### 5.2.3 XRD Data

For phase identification, glancing angle ( $1^\circ$ ) X-ray diffraction (XRD) was used since the typical film thickness was  $\sim 1000\text{\AA}$ . XRD data with different Ti thickness are shown in figure 5-3. As deposited contacts shows pure Ni peaks only (figure 5-3 (a)), as confirmed by the matching peaks with a standard (figure 5-4 (a), JCPDS: 04-0850). Many new diffraction peaks appeared upon annealing the contacts.

Pure Ni XRD peaks were not found from the four annealed contacts. Instead the XRD peaks matched data from a nickel silicide ( $\text{Ni}_2\text{Si}$ ) (figure 5-4 (b), JCPDS: 73-2092). This  $\text{Ni}_2\text{Si}$  phase was found from contacts with either a thin or thick Ti (30 nm) layer, the latter of which showed non-linear I-V. Titanium carbide (TiC) peaks are

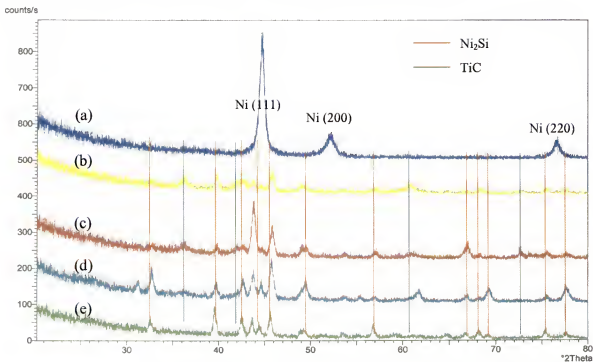


Figure 5-3 XRD data of the contacts with different Ti thickness (a) as deposited, and after annealing with a Ti thickness of (b) 30 nm, (c) 20 nm, (d) 10 nm, and (e) 0 Ti (Ni only) contacts. Contacts are annealed at  $1000^\circ\text{C}$  for 2min.

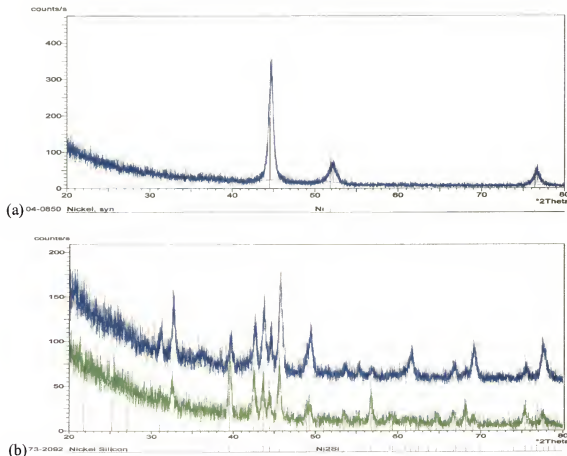


Figure 5-4 XRD peak matching data using JCPDS (a) Ni (JCPDS: 04-0850) for as deposited contacts and (b) Ni<sub>2</sub>Si (JCPDS: 73-2092) for annealed contacts ((d) and (e) in figure 5-3)

detected from contacts with thick bottom Ti (figure 5-3 (b), (c)). As the Ti thickness decreases (Figure 5-3 (d), (e)), the contacts showed more peaks from Ni<sub>2</sub>Si and less from TiC.

XRD data confirmed that nickel silicide and titanium carbide formed in the contacts with concentrations that were dependent on the bottom Ti thickness, which is consistent with AES data.

#### 5.2.4 Auger Electron Spectroscopy (AES)

Figure 5-5 shows AES depth profiles of the contacts with 30 nm Ti. After annealing the interfaces remain sharp with more than 50% of the Ni diffusing to the SiC

interface. A finite Si concentration shows formation of nickel silicide as shown from the XRD data (figure 5-3). Ti still exists inside the Ni-Si layer (silicide).

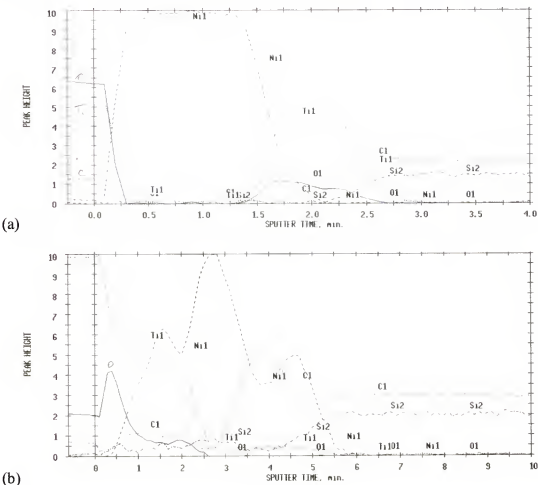


Figure 5-5 AES depth profiles of the contacts with Ti thickness 30 nm (a) as deposited, and (b) annealed at 1000°C for 2min.

Figure 5-6 shows the AES depth profiles from contacts with 20 nm Ti. The majority of the Ni layer diffused to the SiC interface, which remains smooth. Ti level inside Ni layer is negligible. Carbon was distributed in Ni layer. The trend is the same as the schematic model of Ti/Ni/Ti contacts discussed in chapter 4 (figure 4-22). Contacts with 20 nm Ti showed good results with both interface profiles (AES) and contact resistance (I-V).

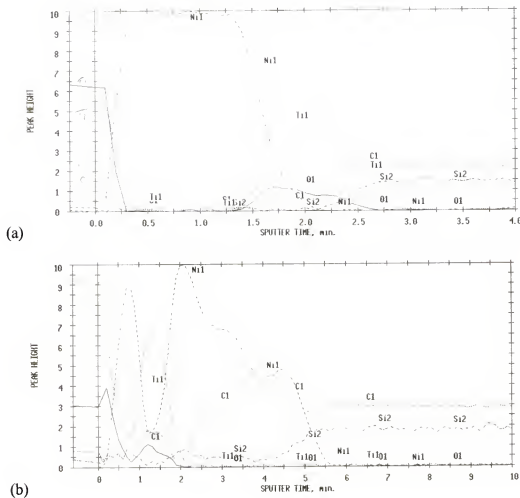


Figure 5-6 AES depth profiles of the contacts with Ti thickness 20 nm (a) as deposited, and (b) annealed at 1000°C for 2min.

AES depth profiles from the contacts with 10 nm Ti (figure 5-7) show a diffuse Ni/SiC interface. Due to thin bottom Ti layer, most Ni layer diffused to SiC interface, and the presence of both Si and Ni signals from the layer show formation of a nickel silicide phase.

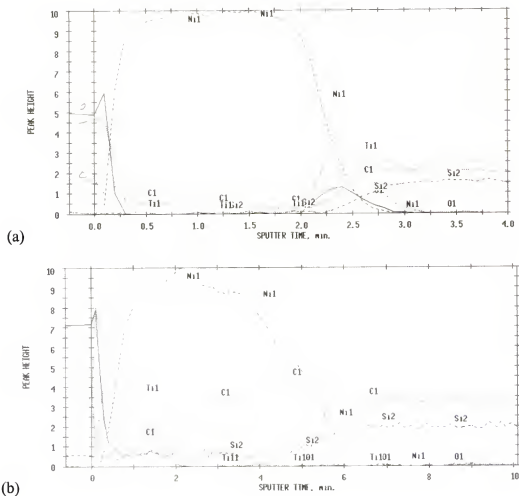


Figure 5-7 AES depth profiles of the contacts with 10 nm Ti thickness (a) as deposited, and (b) annealed at 1000°C for 2min.

AES depth profiles of the contacts with 0 bottom Ti (Ni-only) (figure 5-8 (b)). XTEM data in figure 4-20 showed that diffuse interfaces in AES profiles were related to physically rough interfaces. Since there is no bottom Ti layer on these contacts, Ni reacted with SiC without any barrier. The reactions is indicated by the presence of Si inside the Ni layer, as is reported from the other contacts.

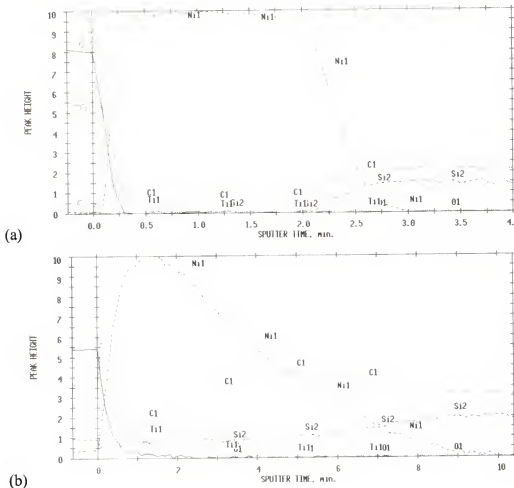


Figure 5-8 AES depth profiles of the contacts with 0 bottom Ti (Ni only) (a) as deposited, and (b) annealed at 1000°C for 2min.

Contacts with 20 nm bottom Ti layers showed good ohmic contacts with resistance as low as  $1 \times 10^{-4} \Omega \text{ cm}^2$  and sharp interface profiles. Thick bottom Ti ( $>20\text{nm}$ ) contacts showed non-linear I-V data. Contacts with thin Ti layers ( $<20\text{ nm}$ ) displayed diffuse interfaces upon annealing. These data suggest that the bottom Ti thickness plays an important role in ohmic contact formation of the Ti/Ni/Ti contacts. The non-linear I-V data of the thick Ti (30 nm) contacts can be attributed to the presence of Ti in the Ni-Si layer (silicide) of the contacts.

### 5.3 Effects of Ni Thickness

The effects of Ni layer thickness on the ohmic contact formation were investigated by varying it from 30 nm to 90 nm, while maintaining constant Ti thickness (6 nm top and 20 nm bottom). The contact structures are as follows, Ti/90nmNi/20nmTi, Ti/70nmNi/20nmTi, Ti/50nmNi/20nmTi, and Ti/30nmNi/20nmTi.

#### 5.3.1 Current and Voltage (I-V) Data

Current-voltage (I-V) data from Ti/Ni/Ti/SiC contacts with different Ni thickness are shown in figure 5-9. All four contacts were rectifying as the as-deposited state (figure 5-9 (a)). Upon annealing at 1000°C for 2 min in N<sub>2</sub>, they became ohmic and showed linear straight I-V data (figure 5-9 (b)). CTLM calculation provided specific contact resistances ( $\rho_c$ ) of  $1.8 \times 10^{-4} \Omega \text{ cm}^2$ ,  $5.8 \times 10^{-4} \Omega \text{ cm}^2$ ,  $3.5 \times 10^{-4} \Omega \text{ cm}^2$  and  $1.9 \times 10^{-4} \Omega \text{ cm}^2$  for 90nmNi/20nmTi, 70nmNi/20nmTi, 50nmNi/20nmTi and 30nmNi/20nmTi contacts, respectively. No major difference in contact resistance was found between the contacts, demonstrating that nickel/titanium forms an ohmic contact regardless of the Ni thickness, if an optimum bottom Ti thickness is provided.

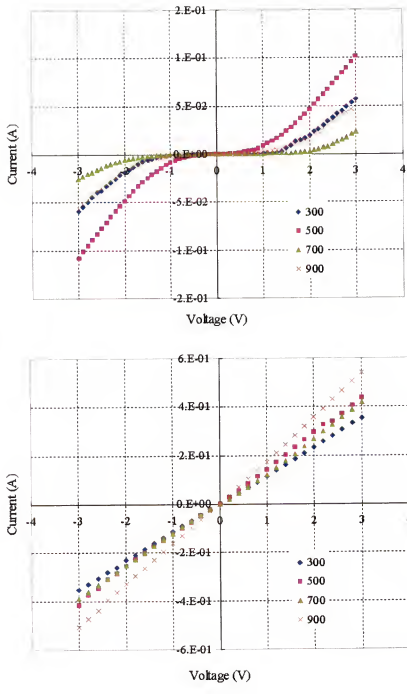


Figure 5-9 I-V curves of the contacts with different Ni thickness. (a) as deposited contacts and (b) contacts annealed at 1000°C for 2min.

### 5.3.2 XRD data

XRD spectra of the annealed contacts with different Ni thickness are shown in figure 5-10. After annealing, pure Ni peaks from the as deposited contacts (figure 5-3

(a)) disappeared and many new diffraction peaks appeared (figure 5-10). The XRD peaks matched data from a nickel silicide ( $\text{Ni}_2\text{Si}$ ) (figure 5-4 (b), JCPDS: 73-2092). This  $\text{Ni}_2\text{Si}$  phase was found from contacts with either a thin (30 nm) or thick Ni (50~90 nm) layer. Titanium carbide (TiC) peaks are detected from contacts (figure 5-10). As Ni thickness increases (Figure 5-10 (c), (d)), the contacts showed more peaks from  $\text{Ni}_2\text{Si}$ .

XRD data confirmed that nickel silicide and titanium carbide formed in the contacts with concentrations that were dependent on the Ni thickness, which is consistent with AES data. Carbon peak was not found.

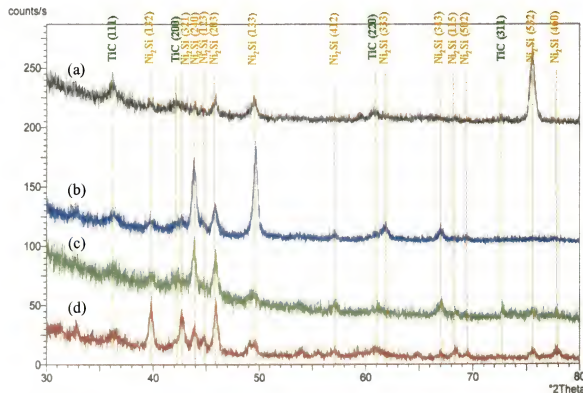


Figure 5-10 XRD data of the contacts with different Ni thickness. (a) 30 nm, (b) 50 nm, (c) 70 nm, and (d) 90 nm. The contacts are annealed at 1000°C for 2min.

### 5.3.3 Auger Electron Spectroscopy (AES)

Figure 5-11 shows AES depth profiles of the Ti/90nmNi/20nmTi contacts. After annealing, the layer sequence is changed due to diffusion and reactions. The trend follows the model in chapter 4 (figure 4-22) except for carbon profiles. The majority of the Ni layer diffuses to the SiC interface. A Si signal is detected inside the Ni layer,

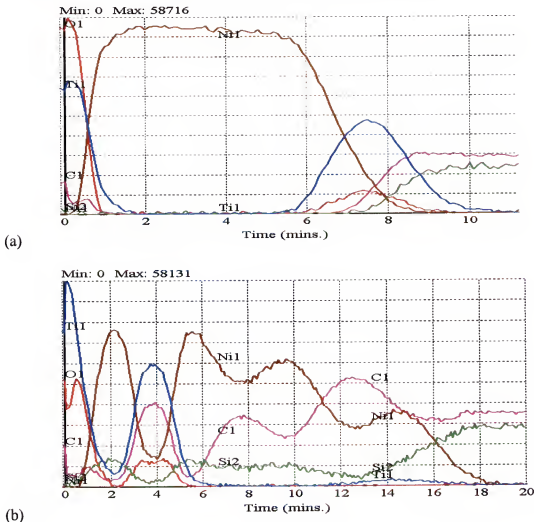


Figure 5-11 AES depth profiles of the Ti/Ni/Ti contacts with 90 nm of Ni (a) as deposited, and (b) annealed at 1000°C for 2min.

whereas Ti in this layer is negligible. Carbon is distributed in Ni layer resulting in two carbon peaks in the depth profile. One peak is close to the Ni/SiC interface, and the second one is inside the Ni layer. Carbon inside the Ni layer has a high concentration

when the Ni is relatively low, suggesting a phase separation between the  $\text{Ni}_2\text{Si}$  and a carbon phase, as discussed in section 4.5. In contrast, the carbon signal intensity from inside the Ti layer increases where Ti signal intensity increases, consistent with the presence of  $\text{TiC}$  suggested by XRD. The profiles at the interfaces remain sharp, suggesting a lack of roughness (figure 5-11 (b)).

AES depth profiles of the Ti/70nmNi/20nmTi and Ti/50nmNi/20nmTi contacts are shown in figures 5-12 and 5-13. The trends and their interpretations are the same as for

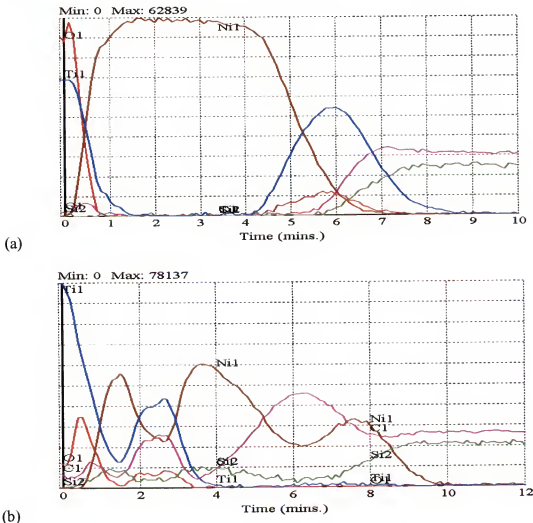


Figure 5-12 AES depth profiles of the contacts with 70 nm of Ni (a) as deposited, and (b) annealed at 1000°C for 2min.

the 90nm Ni contact above except for carbon profiles inside silicide layer. Only one carbon layer is found at the Ni/SiC interface of the contacts (figure 5-12 and 13). No second carbon layer is found inside the silicide layer. Since the Ti/50nmNi/20nmTi contacts have thinner Ni, more compact Ni and carbon profiles are shown compared to the Ti/70nmNi/20nmTi contacts.

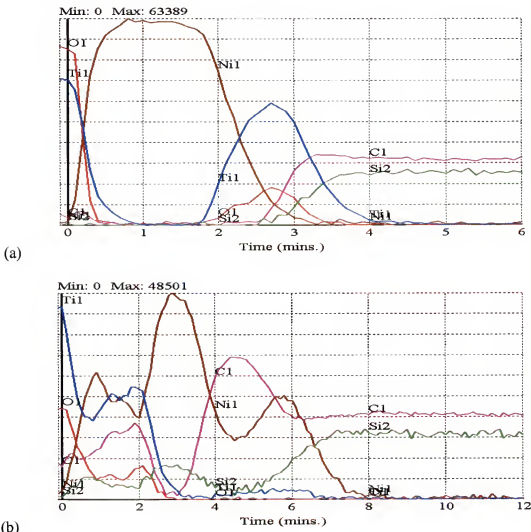


Figure 5-13 AES depth profiles of the contacts with 50 nm of Ni (a) as deposited, and (b) annealed at 1000°C for 2min.

The AES depth profiles of the Ti/30nmNi/20nmTi contacts (figure 5-14) show that Ni diffuses to the SiC interface upon annealing. The top and bottom Ti layers are merged

together, while Si and negligible Ti are found in the Ni layer. Carbon distribution in the Ni layer is smoother than the contacts with a thicker Ni (>30 nm) layer. No significant carbon peak layer was found in the Ni layer or at the Ni/SiC interface. Except for smoother carbon profiles in Ni, carbon follows the same trend as the other thicker Ni contacts. Si in the Ni layer follows the Ni profiles indicating formation of  $\text{Ni}_2\text{Si}$ .

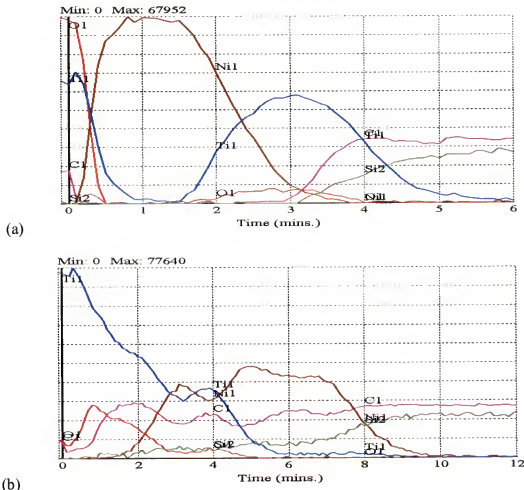


Figure 5-14 AES depth profiles of Ti/Ni/Ti contacts with 30 nm of Ni (a) as deposited, and (b) annealed at 1000°C for 2min.

The AES data showed that the different Ni thickness contacts follow the same trend as the nickel/titanium contacts discussed in chapter 4 (figure 4-22). Ni diffused to SiC and Ti layer is placed on top of the Ni layer. Nickel silicide and titanium carbide

formation is shown. Carbon distribution in the nickel silicide layer changed with Ni thickness. Contacts with 90 nm Ni showed two carbon peak layers, whereas contacts with 50 and 70 nm Ni exhibited one carbon layer at the Ni/SiC interface. Contacts with 30 nm of Ni didn't show any prominent carbon peak layer and the carbon distribution was more uniform than the thicker Ni ( $>30$  nm) contacts. This suggests that Ni layer thickness can control the carbon distribution inside silicide layer.

#### 5.3.4 Transmission Electron Microscopy (TEM)

As shown in the I-V, AES and XRD data, upon annealing contacts turned to ohmic as a result of the interfacial reactions. Interfacial reactions also changed layer sequence and interfacial phases. Cross-sectional TEM analysis was used to confirm the layer sequence and interface profiles of contacts. Cross-sectional TEM pictures of the contacts with different Ni thickness are shown in figure 5-15. Clear and smooth interfaces between SiC and nickel silicide layers are observed (figure 5-15 (b), (c), (d)) even after annealing. Clear phase separation between silicide and carbide layers is shown as well. TEM pictures confirm layer inversion between Ni and Ti layers. TEM image of the as-deposited 30 nm Ni contacts shows that 30 nm Ni layer exists on top of 20 nm bottom Ti layer (figure 5-15 (a)). After annealing Ni in a silicide phase exists below Ti in a carbide phase. Carbon peak layer is not found in the contacts with 30 nm Ni (figure 5-15 (b)) as expected from the AES data (figure 5-14). Contacts with 70 nm Ni show one carbon layer at the silicide/SiC interface (figure 5-15 (c)). Two carbon layers are shown in the contacts with 90 nm of Ni (figure 5-15 (d)), as shown from the AES data (figure 5-11 (b)).

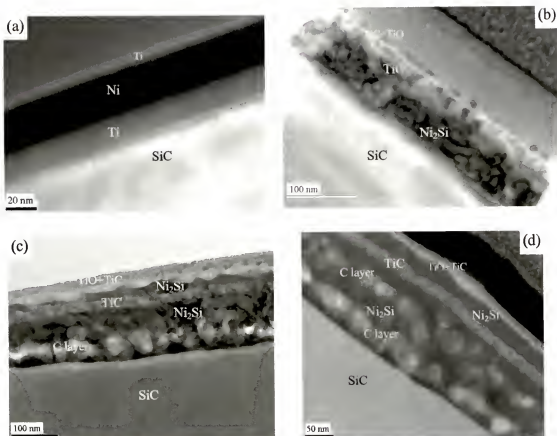


Figure 5-15 Cross-sectional TEM images of the Ti/Ni/Ti contacts with different Ni thickness. (a) as deposited contacts with Ni 30 nm, (b) annealed contacts with Ni 30 nm, (c) annealed contacts with Ni 70 nm, and (d) annealed contacts with Ni 90 nm. Contacts are annealed at 1000°C for 2min. Bottom Ti 20 nm.

Roughness change of the silicide/SiC interface with Ni thickness is measured from the TEM images. The average of the measured roughness values are as follows.  $4.6 \pm 1.6$  nm,  $7.5 \pm 2.3$  nm, and  $9.9 \pm 3.2$  nm are from the contacts with 30 nm Ni, 70 nm Ni, and 90 nm Ni, respectively. Interface roughness increases with Ni thickness due to the thicker silicide layer and more carbon layers in the thick Ni contacts, but it is still lower than the Ni-only contacts ( $25.9 \pm 6.4$  nm) measured in chapter 4 (figure 4-20).

Figure 5-16 shows TEM EDX line scanning data of the contacts with Ni 30 nm and

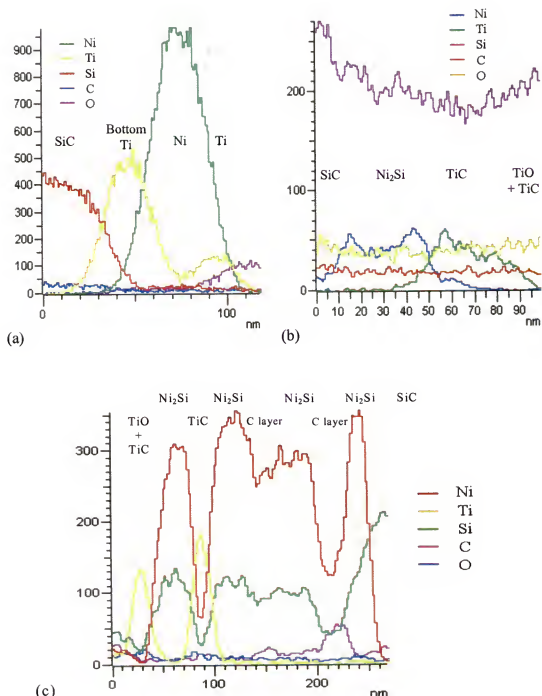


Figure 5-16 TEM EDX line scanning data of the Ti/Ni/Ti contacts with different Ni thickness. (a) as deposited contacts with Ni 30 nm, and (b) annealed contacts with Ni 30 nm, and (c) annealed contacts with Ni 90 nm. Contacts are annealed at 1000°C for 2min. Bottom Ti 20 nm

90 nm. EDX data shows elemental distribution across the contact. The as deposited contacts show layer sequence of Ti/Ni/Ti/SiC (figure 5-16 (a)). The annealed 30 nm Ni contacts exhibit titanium carbide layer on nickel silicide. Uniform carbon profiles are shown as well. Figure 5-16 (c) shows TEM EDX of the annealed Ni 90 nm contacts revealing a complicated layer structure as shown from the TEM images (figure 5-15). Two carbon layers are shown. One is in silicide layer and the other one at the Ni/SiC the interface supporting the TEM images.

These trends are consistent with the TEM images, AES data, and the TEM data in chapter 4 (figure 4-20).

#### 5.4 Discussion

In this chapter, the effects of nickel and bottom titanium thickness on the ohmic contact formation of nickel/titanium contacts were studied. The experimental data from different Ti thickness showed that there was generally a diffuse interface observed when the contact resistance was low. If the bottom Ti thickness was 20 nm or less than 20 nm, an ohmic contact formed. Specific contact resistances as low as  $1 \times 10^{-4} \Omega \text{ cm}^2$  were obtained. Contacts with a 20 nm bottom Ti layer showed a low contact resistance and smooth interface profiles suggesting that this thickness is the optimum condition. For a bottom Ti layer  $< 20$  nm, the contacts showed a diffuse silicide/SiC interface profiles (figure 5-7, 8). The diffuse interface is related to interface roughness, which was confirmed by the TEM data in chapter 4 (figure 4-20). For bottom Ti layers  $> 20$  nm, the annealed contacts exhibited steep profiles. However, these thick Ti contacts also showed non-linear I-V data and high contact resistance, even after annealing (figure 5-1). The difference between the thick Ti contacts and thin Ti contacts are found in the AES data

(figure 5-5~8). AES data from the thick Ti contacts revealed that Ti still existed inside the nickel layer, suggesting incomplete diffusion of Ni to the SiC interface. Thus the presence of Ti layer inside Ni layer provided a barrier preventing the contacts from becoming ohmic. Carbon in thick Ti layers followed the Ti profiles due to formation of TiC, as verified by XRD. Similarly, Si followed the Ni profiles due to formation of Ni<sub>2</sub>Si, as verified again by XRD. Carbon peak layer at the Ni/SiC interface was also found as the contacts with 20 nm Ti.

This trend can be understood using the schematic model of the layers in Ti/Ni/Ti/SiC contacts as shown in chapter 4 (figure 4-22). The model shows that SiC substrate contacts the Ni<sub>2</sub>Si and carbon layer directly. A schematic model of the layers in the thick Ti contacts is drawn in figure 5-17.

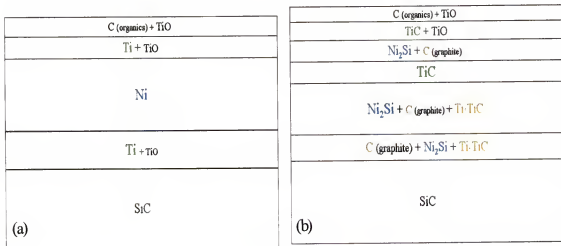


Figure 5-17 Schematic model of the layers in the thick (30nm) bottom Ti contacts (a) as deposited, and (b) annealed contacts

The only difference between the 20 nm Ti contacts (figure 4-22) and the schematic for the thick bottom Ti contacts (figure 5-17) is the presence of Ti (or TiC) layer inside the Ni<sub>2</sub>Si and carbon layers. This suggests that the nickel silicide should contact SiC

substrate directly to obtain an ohmic contact with the 20 nm bottom Ti contacts. The 20 nm bottom Ti contacts showed contact resistance as low as  $1 \times 10^{-4} \Omega \text{ cm}^2$  and smooth silicide/SiC interface ( $7.5 \pm 2.3$  nm) as shown from the TEM data (figure 5-15).

The effects of nickel thickness on the ohmic contact formation of nickel/titanium contacts were studied using a fixed top and bottom Ti thickness (6 and 20 nm). All four contacts with different Ni thickness (90nmNi/20nmTi, 70nmNi/20nmTi, 50nmNi/20nmTi, and 30nmNi/20nmTi) became ohmic upon annealing with the specific contact resistance of  $3.3 \times 10^{-4} \pm 2.5 \times 10^{-4} \Omega \text{ cm}^2$ . The contact resistance didn't vary with nickel thickness (figure 5-9), if the bottom Ti thickness was optimized. The general trend of the interfacial reactions and layer sequence in the nickel/titanium contacts was maintained independent of nickel thickness. Ni diffused to SiC and formed silicide ( $\text{Ni}_2\text{Si}$ ), which was confirmed by XRD (figure 5-10) and TEM (figure 5-15) data. Carbon reacted with Ti forming a TiC layer. AES data showed that carbon in Ti layers matched well the Ti profiles due to the TiC formation (figure 5-11~14). In the nickel silicide layer, carbon exhibited the opposite trend from the Ni profiles.

One parameter that was affected by the Ni thickness was the carbon distribution in the  $\text{Ni}_2\text{Si}$  layer. The AES depth profiles from contacts with 90 nm Ni showed two carbon peaks (layers) with complicated multi layer structures after annealing (figure 5-11). One of them was in the nickel silicide and the other one at the silicide/SiC interface. As Ni thickness decreased, the number of carbon layers in the silicide decreased as well. Contacts with 70 and 50 nm Ni layers exhibited one carbon layer at the silicide/SiC interface. More compact profiles were observed from 50 nm Ni contacts. In the 30 nm Ni contacts, the carbon distribution in the Ni silicide layer was more uniform than in the

thicker Ni (>30 nm) contacts. No significant carbon layer was found at the silicide/SiC interface of the 30 nm Ni contacts (figure 5-14). TEM images showed the same trend as described above (figure 5-15).

The dependence of carbon distribution on Ni thickness can be understood based on phase separation between nickel silicide and a carbon phase (probably graphite) as described in chapter 4. Graphite has been reported to exist as a second phase in nickel silicide,<sup>8,39</sup> therefore it is reasonable to expect such a phase separation in the present experiment. As the Ni thickness increases, there will be more carbon atoms in the silicide layer due to the larger extent of reaction between Ni and SiC to form silicide. When the concentration of carbon exceeds the solid solubility limit in nickel silicide, carbon will precipitate as a second phase in the silicide layer. When the carbon atoms precipitate in a matrix, they will try to minimize diffusion distance. This results in a band structure.<sup>87</sup> However, the generation of new carbon layers in a matrix will increase the energy term associated with the creation of a new interface between the silicide and the carbon precipitate. To reduce this interface energy term, the system may attempt to minimize the interface area between silicide and carbon phase by spherodization and Ostwald ripening. Thus the free energy reduction from carbon precipitation works to create small precipitates, while the interface energy terms tend to agglomerate and enlarge them. The balance between these two driving forces dictates that the carbon form layers, the number of which depends upon the extent of reaction, i.e. on the Ni layer thickness. When the total thickness of matrix (nickel silicide in this study) increases, the number of precipitated carbon layers inside the matrix tends to increase to reduce the

diffusion distance of carbon. This basic model of phase separation provides a good explanation for the observation of multiple carbon layers depending on the Ni thickness.

In contacts with 90 nm of Ni, diffusion distance of the liberated carbon atoms was long enough to require extra time for long-range diffusion. In fact, the distances were too long and the reaction generated a new interface between the silicide and a carbon layer, i.e. a second carbon layer was formed. Contacts with 70 and 50 nm of Ni showed one carbon peak at the silicide/SiC interface, because the carbon diffusion distance was not long enough to force the system to spend the extra energy to form a new interface. In contacts with 30 nm Ni, the smaller area of the silicide matrix and smaller amount of carbon provided a smoother carbon profile in  $\text{Ni}_2\text{Si}$ . The carbon intensity at the silicide/SiC interface was not significantly higher than the average carbon concentration in the silicide layer, suggesting that carbon did not concentrate at the interface.

The Ni to Ti ratio of the contacts was an important factor that affected the smoothness of the carbon profile in silicide layer of the 30 nm Ni contacts. Since the Ti layers react with the liberated carbon and form TiC, in lower Ni to Ti ratio contacts (30 nm Ni contacts have the lowest Ni to Ti ratio), a larger portion of the carbon atoms will be consumed in the carbide reaction with titanium than in the thick Ni contacts (higher Ni to Ti ratio). This results in a lower driving force to cause precipitation of carbon in silicide layer, which results in a smoother carbon profile. Based on this explanation, schematic models of the contacts with different Ni thickness are drawn in the following figures.

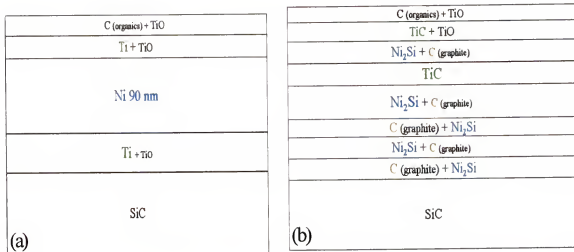


Figure 5-18 Schematic model of the layers in 90nm Ni contacts (a) as deposited, and (b) annealed contacts, bottom Ti 20 nm.

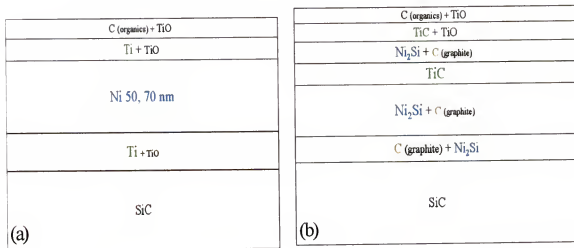


Figure 5-19 Schematic model of the layers in 50 and 70 nm Ni contacts (a) as deposited, and (b) annealed contacts, bottom Ti 20 nm.

The contacts with 70 and 50 nm Ni have the same layer sequence as the schematic model shown in chapter 4, i.e. one carbon layer. A schematic model of the 30 nm Ni contacts is shown in figure 5-20, and no separate carbon layer is displayed.

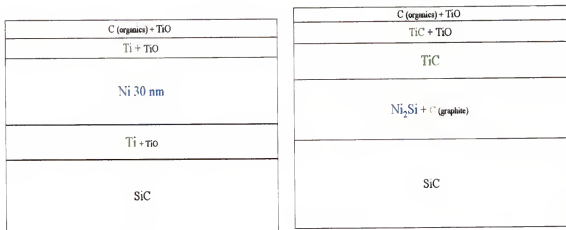


Figure 5-20 Schematic model of the layers in 30 nm Ni contacts (a) as deposited, and (b) annealed contacts, bottom Ti 20 nm.

These models suggest that the Ni layer thickness can be used to control carbon distribution in the silicide layer. Excess carbon in silicide layer has been reported to limit the high temperature stability of the contacts.<sup>8,39</sup> Therefore the carbon layer can be reduced or removed by controlling the Ni thickness for a fixed bottom Ti thickness.

TEM images showed that the roughness of silicide/SiC interface increased with Ni thickness. The average measured roughnesses are  $4.6 \pm 1.6$  nm,  $7.5 \pm 2.3$  nm, and  $9.9 \pm 3.2$  nm from the contacts with 30 nm Ni, 70 nm Ni, and 90 nm Ni, respectively. Interface roughness increases with Ni thickness due to more reaction forming thicker silicide and carbon layers, but these roughnesses for Ti/Ni/Ti contacts were still lower than for Ni-only contacts (25.9 nm) reported in chapter 4.

The CTLM data show that 30 nm Ni and 20 nm Ti contacts provide good ohmic contacts with low contact resistance ( $1.9 \times 10^{-4} \Omega \text{ cm}^2$ ) and smooth interfaces. The contacts provide low carbon concentration as well, since a separate carbon layer is not found in the contacts with 30 nm Ni and 20 nm Ti.

### 5.5 Summary

The effects of Ni and Ti layer thickness on the resistance and interfacial abruptness of n-type silicon carbide ohmic contacts were studied. In contact with a top and bottom Ti layer sandwiching a Ni intermediate layer, the bottom Ti thickness was more important than the Ni thickness for the ohmic contact properties. The contacts with 20 nm bottom Ti layer showed a low contact resistance ( $1.0 \times 10^{-4} \Omega \text{ cm}^2$ ) while maintaining a smooth interface. Ti/Ni/Ti contacts with Ti bottom layer  $< 20$  nm showed rough interfaces with low contact resistance. Thicker Ti ( $> 20$  nm) contacts showed non-linear I-V data.

The effects of Ni thickness were studied. Specific contact resistances ( $\rho_c$ ) of  $3.3 \times 10^{-4} \pm 2.5 \times 10^{-4} \Omega \text{ cm}^2$  were obtained from 90nmNi/20nmTi, 70nmNi/20nmTi, 50nmNi/20nmTi and 30nmNi/20nmTi contacts. No major difference in the contact resistance was found with Ni thickness. However, carbon distribution in the nickel silicide layers changed with Ni thickness. The number of carbon layers in silicide increased with Ni thickness. The 30 nm Ni contacts (Ti/30nmNi/20nmTi) showed more uniform carbon distribution in the Ni layer than for the thicker Ni ( $> 30$  nm) contacts. No carbon peak layer was found in the 30 nm Ni contacts. Thus, the carbon layer can be reduced or removed by controlling the Ni thickness for a fixed bottom Ti layer thickness. The silicide/SiC interface roughness increased with Ni thickness. The measured roughness values were  $4.6 \pm 1.6$  nm,  $7.5 \pm 2.3$  nm, and  $9.9 \pm 3.2$  nm from the contacts with 30 nm Ni, 70 nm Ni, and 90 nm Ni, respectively, but all of these roughness values are lower than those from contacts with only Ni ( $25.9 \pm 6.4$  nm). These results showed that

6nm Ti / 30nm Ni / 20nm Ti / SiC contacts provide good ohmic contact with low contact resistance, smooth interface, and less free carbon.

## CHAPTER 6 CONCLUSIONS

Titanium/nickel/titanium/SiC multi layer metallization has been studied for ohmic contacts to n-type SiC. Good ohmic contacts to n-type SiC were obtained from the Ti/Ni/Ti/SiC, with a smooth interface morphology and contact resistances as low as  $1 \times 10^{-4} \Omega \text{-cm}^2$ . As-deposited Ni/SiC, Ni/Ti/SiC and Ti/Ni/Ti/SiC contacts were rectifying. After annealing at 1000°C for 2 minutes in N<sub>2</sub> ambient all of these contacts turned to ohmic. Specific contact resistances ( $\rho_c$ ) of  $1 \times 10^{-4} \Omega \text{ cm}^2$  for both Ni/Ti and Ti/Ni/Ti contacts were obtained. For Ni/SiC annealed contacts, the RMS interfacial roughness was  $25.9 \pm 6.4 \text{ nm}$ , while that for Ni/Ti/SiC or Ti/Ni/Ti/SiC was  $7.5 \pm 2.3 \text{ nm}$ . The ohmic contact was formed when a fraction of the Ni layer moved to the SiC interface and formed Ni<sub>2</sub>Si, releasing carbon as a reaction product. In Ti/Ni/Ti/SiC structures, this carbon reacted with both the top and bottom Ti layers and formed titanium carbide (TiC). Carbon in excess of that consumed to form TiC was distributed in the silicide layer and at the silicide/SiC interface as a carbon phase. These phases were observed because titanium carbide has a lower free energy of formation than titanium silicide, and nickel silicide has a lower free energy of formation than that of titanium silicide.

The effects of Ti and Ni layer thickness on the ohmic contact properties were also studied. Ti thickness was more important than Ni thickness in achieving smooth interfaces and low contact resistances. Contacts with a 20nm bottom Ti layer showed a contact resistance of  $1 \times 10^{-4} \Omega \text{ cm}^2$ , while maintaining an interfacial roughness of  $7.5 \pm 2.3 \text{ nm}$ . Thicker bottom layer Ti (>20 nm) contacts were rectifying with a non-linear I-V

data, and there was still a Ti layer between the Ni and SiC after annealing. The lack of an ohmic contact was attributed to the Ti layer acting as a diffusion barrier preventing the formation of  $\text{Ni}_2\text{Si}$ .

The Ni thickness was varied from 90 to 30 nm over 20 nm Ti bottom layers, but the specific contact resistances ( $\rho_C$ ) ( $3.3 \times 10^{-4} \pm 2.5 \times 10^{-4} \Omega \text{ cm}^2$ ) did not vary systematically with Ni thickness. Thicker Ni ( $> 30 \text{ nm}$ ) contacts showed a non-uniform carbon distribution in the silicide layer with carbon layers at the silicide/SiC interface as a second phase. Carbon distribution in the thin Ni contacts (Ti/30nmNi/20nmTi) was more uniform than in the contacts with thicker Ni. No significant carbon layer was found at the silicide/SiC interface in the thin Ni (30nm) contacts. The RMS interfacial roughness values are  $4.6 \pm 1.6 \text{ nm}$ ,  $7.5 \pm 2.3 \text{ nm}$ , and  $9.9 \pm 3.2 \text{ nm}$  from 30 nm, 70 nm, and 90 nm Ni contacts, respectively. Interface roughness increases with Ni thickness due to thicker silicide and carbon layers in the thick Ni contacts, but they are still lower than the Ni-only contacts ( $25.9 \pm 6.4 \text{ nm}$ ).

## CHAPTER 7 FUTURE WORK

SiC and related materials have presented promising opportunities in materials and device research area. The continued advancement of new devices using SiC requires better understanding of the mechanisms controlling the formation of ohmic contacts to SiC.

For the interfacial reactions in nickel/titanium contacts to SiC, the first work should be to find a more detailed mechanism of the ohmic contact formation in nickel/titanium contacts. More works on understanding the role of  $\text{Ni}_2\text{Si}$  phase in contact formation will be helpful in improving the contact properties. A study on the time evolution of the interfacial phases in nickel/titanium contacts will be an important area for further work to deepen understanding of the interfacial reactions.

For the effects of Ti thickness on the nickel/titanium contacts, works should be continued to study the effect of Ti layer inside the nickel silicide layer on the ohmic contact formation. Understanding interfacial morphology and phase identification using XTEM will be helpful.

For the effect of Ni thickness, while this dissertation provides simple models for the carbon layer formation in nickel silicide layer, it requires more study and a complete model. A study on the time evolution of the carbon phase inside the nickel silicide will be an important subject.

To confirm the principles of Ti/Ni/Ti/SiC contacts, it will be interesting to study a different metal combination following the principle. As shown from table 4-2, Ni/Ta will be a good candidate to form ohmic contacts to n-type silicon carbide.

## LIST OF REFERENCES

1. M. A. Capano and R. J. Trew, *Mrs Bulletin* **22** (3), 19-22 (1997).
2. V. E. Chelnokov, A. L. Syrkin, and V. A. Dmitriev, *Diamond and Related Materials* **6** (10), 1480-1484 (1997).
3. V. E. Chelnokov and A. L. Syrkin, *Materials Science and Engineering B-Solid State Materials For Advanced Technology* **46** (1-3), 248-253 (1997).
4. J. A. Cooper, M. R. Melloch, R. Singh, *Ieee Transactions On Electron Devices* **49** (4), 658-664 (2002).
5. J. Crofton, P. G. McMullin, J. R. Williams, *Journal of Applied Physics* **77** (3), 1317-1319 (1995).
6. M. W. Cole, P. C. Joshi, C. W. Hubbard, *Journal of Applied Physics* **88** (5), 2652-2657 (2000).
7. J. Crofton, L. M. Porter, and J. R. Williams, *Physica Status Solidi B-Basic Research* **202** (1), 581-603 (1997).
8. T. Marinova, A. KakanakovaGeorgieva, V. Krastev, *Materials Science and Engineering B-Solid State Materials For Advanced Technology* **46** (1-3), 223-226 (1997).
9. E. D. Luckowski, J. M. Delucca, J. R. Williams, *Journal of Electronic Materials* **27** (4), 330-334 (1998).
10. J. R. Williams and M. J. Bozack E. D. Luckowski, presented at the MRS Symposium Proc., 1996 (San Francisco)
11. A. G. Milnes, *Heterojunctions and Metal-Semiconductor Junctions* (New York, Academic Press, 1972).
12. S. M. Sze, *Physics of Semiconductor Devices, 2nd ed.* (New York, Wiley, 1981).
13. C. T. Sah, *Fundamentals of Solid State Electronics* (River Edge, Academic, 1990).
14. H. H. Berger, *Solid-State Electronics* **15** (2), 145 (1972).

15. S. S. Li, *Semiconductor Physical Electronics* (New York, Plenum, 1990).
16. R. E. Williams, "Chapter 11 Ohmic Contact" in *GaAs Processing Techniques* (New York, Dedham, 1993).
17. G. S. Marlow and M. B. Das, *Solid-State Electronics* **25** (2), 91-94 (1982).
18. Y. S. Park, "SiC Materials and Devices," in *Semiconductor and Semimetals* (New York, Academic, 1998), Vol. 52.
19. M. R. Melloch and J. A. Cooper, *Mrs Bulletin* **22** (3), 42-47 (1997).
20. T. P. Chow and R. Tyagi, *Ieee Transactions On Electron Devices* **41** (8), 1481-1483 (1994).
21. T. P. Chow and M. Ghezzo, presented at the MRS Symposium Proc., 1996 (San Francisco)
22. W. V. Muench and I. Pfaffeneder, *Journal of Applied Physics* **48** (11), 4831-4833 (1977).
23. W. V. Muench and E. Pettenpaul, *Journal of Applied Physics* **48** (11), 4823-4825 (1977).
24. S. Yoshida, *Properties of Silicon Carbide* (London, INSPEC, 1995).
25. W. J. Choyke and G. Pensl, *Mrs Bulletin* **22** (3), 25-29 (1997).
26. R. Singh, J. A. Cooper, M. R. Melloch, *Ieee Transactions On Electron Devices* **49** (4), 665-672 (2002).
27. K. Moore and R. J. Trew, *Mrs Bulletin* **22** (3), 50-56 (1997).
28. L. M. Porter and R. F. Davis, *Materials Science and Engineering B-Solid State Materials For Advanced Technology* **34** (2-3), 83-105 (1995).
29. L. Beyer J. Crofton, and S. E. Mahney, presented at the High Temperature Electronics Conference, 1998
30. C. Hallin, R. Yakimova, B. Pecz *et al.*, *Journal of Electronic Materials* **26** (3), 119-122 (1997).
31. A. Kakanakova-Georgieva, T. Marinova, O. Noblanc, *Thin Solid Films* **344**, 637-641 (1999).
32. Y. Gao, Y. Tang, M. Hoshi, *Solid-State Electronics* **44** (10), 1875-1878 (2000).
33. S. K. Lee, C. M. Zetterling, M. Ostling, *Solid-State Electronics* **44** (7), 1179-1186 (2000).

34. S. K. Lee, C. M. Zetterling, E. Danielsson, *Applied Physics Letters* **77** (10), 1478-1480 (2000).
35. A. Kakanakova-Georgieva, T. Marinova, O. Noblanc, *Thin Solid Films* **337** (1-2), 180-183 (1999).
36. B. Pecz, *Applied Surface Science* **184** (1-4), 287-294 (2001).
37. C. Hubbard M. W. Cole, D. Dermaree and P. Searson, presented at the Electrochemical Society Proc., 1998 (San Francisco)
38. C. S. Pai, C. M. Hanson, and S. S. Lau, *Journal of Applied Physics* **57** (2), 618-619 (1985).
39. I. Ohdomari, S. Sha, H. Aochi, *Journal of Applied Physics* **62** (9), 3747-3750 (1987).
40. A. Bachli, M. A. Nicolet, L. Baud, *Materials Science and Engineering B-Solid State Materials For Advanced Technology* **56** (1), 11-23 (1998).
41. M. G. Rastegaeva, A. N. Andreev, A. A. Petrov, *Materials Science and Engineering B-Solid State Materials For Advanced Technology* **46** (1-3), 254-258 (1997).
42. N. Lundberg, C. M. Zetterling, and M. Ostling, *Applied Surface Science* **73**, 316-321 (1993).
43. A. Ohi, J. Labis, Y. Morikawa, *Applied Surface Science* **190** (1-4), 366-370 (2002).
44. F. Roccaforte, F. La Via, V. Raineri, *Applied Surface Science* **184** (1-4), 295-298 (2001).
45. F. Roccaforte, F. La Via, V. Raineri, "Electrical characterization of nickel silicide contacts on silicon carbide," in *Silicon Carbide and Related Materials 2001, Pts 1 and 2, Proceedings* (Trans Tech Publications Ltd, Zurich-Uetikon, 2002), Vol. 389-3, pp. 893-896.
46. S. G. Muller, M. F. Brady, W. H. Brixius, "High quality SiC substrates for semiconductor devices: From research to industrial production," in *Silicon Carbide and Related Materials 2001, Pts 1 and 2, Proceedings* (2002), Vol. 389-3, pp. 23-28.
47. S. G. Muller, R. C. Glass, H. M. Hobgood, *Journal of Crystal Growth* **211** (1-4), 325-332 (2000).
48. R. C. Glass, D. Henshall, V. F. Tsvetkov, *Mrs Bulletin* **22** (3), 30-35 (1997).
49. Milton Ohring, *The Materials Science of Thin Films* (Boston, Academic Press, 1992).

50. C. R. Brundle and C. A. Evans, *Encyclopedia of Materials Characterization : surfaces, interfaces, thin films* (Boston, Butterworth-Heinemann, 1992).
51. L. C. Feldman, *Fundamentals of Surface and Thin Film Analysis* (New York, North-Holland, 1986).
52. O. A. Agueev, A. M. Svetlichnyi, and R. N. Razgonov, "Influence of rapid thermal annealing on Ni/6H-SiC contact formation," in *Silicon Carbide and Related Materials 2001, Pts 1 and 2, Proceedings* (Trans Tech Publications Ltd, Zurich-Uetikon, 2002), Vol. 389-3, pp. 901-904.
53. D. Basak and S. Mahanty, Materials Science and Engineering B-Solid State Materials For Advanced Technology **98** (2), 177-180 (2003).
54. R. S. Okojie, A. A. Ned, A. D. Kurtz, IEEE Transactions on Electron Devices **46** (2), 269-274 (1999).
55. S. K. Lee, C. M. Zetterling, M. Ostling, Journal of the Korean Physical Society **40** (4), 572-576 (2002).
56. L. G. Fursin, J. H. Zhao, and M. Weiner, Electronics Letters **37** (17), 1092-1093 (2001).
57. R. Getto, J. Freytag, M. Kopnarski, Materials Science and Engineering B-Solid State Materials for Advanced Technology **61-2**, 270-274 (1999).
58. F. Goessmann, R. Wenzel, and R. Schmid-Fetzer, Journal of Materials Science-Materials in Electronics **9** (2), 103-107 (1998).
59. S. Y. Han, N. K. Kim, E. D. Kim, "Effects of interfacial reactions on electrical properties of Ni ohmic contacts on n-type 4H-SiC," in *Silicon Carbide and Related Materials 2001, Pts 1 and 2, Proceedings* (Trans Tech Publications Ltd, Zurich-Uetikon, 2002), Vol. 389-3, pp. 897-900.
60. M. Hirai, J. P. Labis, A. Ohi, Applied Surface Science **216** (1-4), 187-191 (2003).
61. F. La Via, F. Roccaforte, A. Makhtari, Microelectronic Engineering **60** (1-2), 269-282 (2002).
62. M. W. Cole, P. C. Joshi, and M. Ervin, Journal of Applied Physics **89** (8), 4413-4416 (2001).
63. S. Y. Han, J. Y. Shin, B. T. Lee, Journal of Vacuum Science & Technology B **20** (4), 1496-1500 (2002).
64. M. Levit, I. Grinberg, and B. Z. Weiss, Journal of Applied Physics **80** (1), 167-173 (1996).

65. T. Nakamura, H. Shimada, and M. Satoh, "Ohmic contact formation on n-type 6H-SiC using NiSi<sub>2</sub>," in *Silicon Carbide and Related Materials - 1999 Pts, 1 & 2* (Trans Tech Publications Ltd, Zurich-Uetikon, 2000), Vol. 338-3, pp. 985-988.
66. T. Nakamura and M. Satoh, "NiSi<sub>2</sub> ohmic contact to n-type 4H-SiC," in *Silicon Carbide and Related Materials 2001, Pts 1 and 2, Proceedings* (Trans Tech Publications Ltd, Zurich-Uetikon, 2002), Vol. 389-3, pp. 889-892.
67. Malcome W. Chase Jr. NIST-JANAF, *Thermochemical Tables* (Washington DC, American Chemical Society 1998).
68. M. Binnewies, *Thermochemical Data of Elements and Compounds* (Weinheim, Wiley VCH 1999).
69. Noel C. MacDonald Lawrence E. Davis, Paul W. Palmberg, Gerald E. Riach, and Roland E. Weber, *Handbook of Auger Electron Spectroscopy* (New York, Perkin-Elmer Corporation, 1990).
70. S. M. Mendoza, L. I. Vergara, M. C. G. Passeggi, *Applied Surface Science* **211** (1-4), 236-243 (2003).
71. I. Vaquila, M. C. G. Passeggi, and J. Ferron, *Applied Surface Science* **93** (3), 247-253 (1996).
72. I. Vaquila, L. I. Vergara, M. C. G. Passeggi, *Surface & Coatings Technology* **122** (1), 67-71 (1999).
73. P. E. Viljoen, W. D. Roos, H. C. Swart, *Applied Surface Science* **101**, 612-616 (1996).
74. E. Mitura, A. Niedzielska, P. Niedzielski, *Diamond and Related Materials* **5** (9), 998-1001 (1996).
75. T. W. Kang, C. Y. Hong, C. K. Chung, *Thin Solid Films* **342** (1-2), 184-187 (1999).
76. H. C. Swart, A. J. Jonker, C. H. Claassens, *Applied Surface Science* **205** (1-4), 231-239 (2003).
77. S. P. Murarka, *Silicides for VLSI Applications* (New York, Academic, 1982).
78. J. S. Park, K. Landry, and J. H. Perepezko, *Materials Science and Engineering a-Structural Materials Properties Microstructure and Processing* **259** (2), 279-286 (1999).
79. K. N. Tu and J. W. Mayer J. M. Poate, *Thin Films-Interdiffusion and Reactions* (New York, Wiley, 1978).

80. J. M. Delucca and S. E. Mohney, presented at the MRS Symposium Proc., 1996 (San Francisco)
81. F. Goesmann and R. SchmidFetzer, Materials Science and Engineering B-Solid State Materials for Advanced Technology **46** (1-3), 357-362 (1997).
82. W. F. Seng and P. A. Barnes, Materials Science and Engineering B-Solid State Materials For Advanced Technology **76** (3), 225-231 (2000).
83. J. W. Mayer and S. S. Lau, *Electronic Materials Science : for Integrated Circuits in Si and GaAs* (New York, Macmillan, 1990).
84. F. Touati, K. Takemasa, and M. Saji, IEEE Transactions on Electron Devices **46** (3), 444-448 (1999).
85. R. Wenzel, F. Goesmann, and R. Schmid-Fetzer, Journal of Materials Science-Materials in Electronics **9** (2), 109-113 (1998).
86. American Society of Metals, *Metals Handbook*, 9th ed. (Cleveland, American Society of Metals, 1986), Vol. 10.

### BIOGRAPHICAL SKETCH

Jae Hyun Park was born in Pusan of Republic of Korea, on September 9, 1967. After completing 12 years of primary and secondary education in Pusan, he moved to Seoul and enrolled in the Department of Metallurgical Engineering (now the School of Material Science and Engineering) at Seoul National University in 1986. In 1990, he was admitted to the graduate program at Seoul National University. Under Professor Lee's guidance, he finished his MS thesis on tungsten CVD process for Si integrated circuit application in the Spring of 1992. After graduation, he joined a company LG Semiconductor in Korea in 1992, and continued to work until the summer of 1999. With a strong interest in the semiconductor process and devices, he came to Gainesville to attend the University of Florida in 1999, majoring in electronic materials in the Department of Materials Science of Engineering. Under the guidance of Dr. Paul H. Holloway, he worked on ohmic contact technology for silicon carbide and received his Ph.D in December 2003.

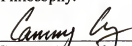
I certify that I have read this study and that in my opinion it conforms to acceptable standards of scholarly presentation and is fully adequate, in scope and quality, as a dissertation for the degree of Doctor of Philosophy.

  
\_\_\_\_\_  
Paul H. Holloway, Chairman  
Distinguished Professor of Materials Science and Engineering

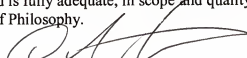
I certify that I have read this study and that in my opinion it conforms to acceptable standards of scholarly presentation and is fully adequate, in scope and quality, as a dissertation for the degree of Doctor of Philosophy.

  
\_\_\_\_\_  
Kevin S. Jones  
Professor of Materials Science and Engineering

I certify that I have read this study and that in my opinion it conforms to acceptable standards of scholarly presentation and is fully adequate, in scope and quality, as a dissertation for the degree of Doctor of Philosophy.

  
\_\_\_\_\_  
Cammy Abernathy  
Professor of Materials Science and Engineering

I certify that I have read this study and that in my opinion it conforms to acceptable standards of scholarly presentation and is fully adequate, in scope and quality, as a dissertation for the degree of Doctor of Philosophy.

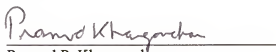
  
\_\_\_\_\_  
David Norton  
Professor of Materials Science and Engineering

I certify that I have read this study and that in my opinion it conforms to acceptable standards of scholarly presentation and is fully adequate, in scope and quality, as a dissertation for the degree of Doctor of Philosophy.

  
\_\_\_\_\_  
Sheng S. Li  
Professor of Electrical and Computer Engineering

This dissertation was submitted to the Graduate Faculty of the College of Engineering and to the Graduate School and was accepted as partial fulfillment of the requirements for the degree of Doctor of Philosophy.

December 2003

  
\_\_\_\_\_  
Pramod P. Khargonekar  
Dean, College of Engineering

\_\_\_\_\_  
Winfred M. Phillips  
Dean, Graduate School